工學博士學位論文

Performance Improvement of Electro-Responsive Smart Fluid Based on Nanoparticle Characteristics

나노입자 특성에 따른 전기 반응성 지능형 유체의 성능 향상

2016年 2月

서울大學校 大學院

化學生物工學部

李 承 愛

Performance Improvement of Electro-Responsive Smart Fluid Based on Nanoparticle Characteristics

by

Seungae Lee

Submitted to the Graduate School of Seoul National University

in Partial Fulfillment of the Requirements

for the Degree of Doctor of Philosophy

February, 2016

Thesis Adviser: Jyongsik Jang

ABSTRACT

Stimuli-responsive materials, so-called smart materials, change their structure, dimension, and interactions in response to external stimuli, such as pH, temperature, light, mechanical force, and electric or magnetic field. Stimuli-responsive materials have received tremendous worldwide attention because of their fascinating characteristic, *e.g.* adjustability of response based on environmental condition. In particular, electro-responsive materials, defined as the materials that exhibit controllable properties according to electric field, are considered as the most feasible candidate for practical applications due to their low power consumption, rapid reversible transition, and simple fluid mechanics. Up to date, various electro-responsive materials have been produced and adopted to electro-responsive fluid. However, few researches have addressed the dependence of electro-responsive activities on particle features. Moreover, there are still several limitations for substantive commercialization of electro-responsive fluids due to deficient performance and sedimentation problem. Consequently, it is still challenging to develop innovative electro-responsive materials that represent high efficiency. In addition, it is required to obviously clarify the effect of particle properties on

electro-responsive behavior to better understand the mechanism underlying electro-responsive fluids.

This dissertation describes electro-responsive characteristics based on different critical parameters, including particle geometry, dielectric property, and electrical conductivity, by fabricating inventive nanoparticles for electro-responsive fluids. First, electro-responsive characteristics depending on particle geometry is examined by varying the aspect ratio of graphene oxide (GO)-wrapped silica materials. Electrorheological (ER) effect of the GO-wrapped silica material-based fluid is improved as the aspect ratio of the particle increases, which is attributed to geometrical effect (*e.g.* flow resistance and mechanical stability) and superior dielectric properties. Second, the relationship between particle shell structure and electro-responsive property is investigated by synthesizing the size-controlled single-shell and double-shell SiO_2/TiO_2 hollow nanoparticles for ER fluids. It is revealed that outstanding electro-responsive performance of double-shell SiO_2/TiO_2 hollow nanoparticles (DS HNPs) is associated with the enhanced interfacial polarization. In addition, electro-responsive efficiency is observed to be enhanced with a decrease in the diameter of particles, ascribed to a large achievable polarizability determined

by dielectric constant. Furthermore, remarkable anti-sedimentation property is observed, which promise a sufficient potential for practical application. Third, the correlation of electrical conductivity and electro-responsive behavior is identified by introducing few-layer molybdenum disulfide (MoS_2) nanosheets to ER fluid. Electrical conductivity of MoS_2 can be tunable by adjusting the annealing temperature because of its semiconductivity. It is meaningful that an in-depth study on the effect of electrical conductivity on ER effect is carried out. Moreover, to the best our knowledge, this is the first time to report the possibility of transition-metal dichalcogenides as a candidate of ER fluid. This study may provide promising approaches for performance improvement of electro-responsive smart fluids.

KEYWORDS: Smart fluid; Stimuli-responsive; Electro-responsive; Nanoparticle; Electrorheological fluid

STUDENT NUMBER: 2011–22926

List of Abbreviations

0-D : zero-dimensional

1-D : one-dimensional

A : cross-sectional area

A_{BET} : total surface area

A_{ISP} : surface area of the small pores within shells

A_{shell} : surface of the shells except small pores within shells

A_z : depolarization factor

AFM : atomic force microscopy

APS : 3-aminopropyltrimethoxysilane

BET : Brunauer–Emmett–Teller

C_d : drag coefficient

CCJ : Cho–Choi–Jhon

CVD : chemical vapor deposition

DS HNPs : double-shell SiO_2/TiO_2 hollow nanoparticles

E : electric field intensity

E_0 : applied electric field strength

E_g : band gap energy

EA : elemental analyzer

EDS : energy dispersive X-ray spectroscopy

ER : electrorheological

F_d : dynamic drag force

f_{max} : frequency of the loss peak

FE-SEM : field-emission scanning electron microscopy

FWHM : full width at half maximum

GER : giant electrorheological

GERF : giant electrorheological fluid

GO : graphene oxide

ICP-AES : inductively coupled plasma-atomic emission spectrometer

k : Boltzmann constant

LCST : lower critical solution temperature

MoS_2 : molybdenum (IV) disulfide

p : dipole moment

PL : photoluminescence

PVP : polyvinylpyrrolidone

SiO_2 : silicon dioxide, or silica

SS HNPs : single shell SiO_2/TiO_2 hollow nanoparticles

ST CS NPs : SiO_2/TiO_2 core/shell nanoparticles

STEM : scanning transmission electron microscopy

STEM-EDS : scanning transmission electron microscopy-energy dispersive spectroscopy

STS CS NPs : silica-coated SiO_2/TiO_2 core/shell nanoparticles

STST CS NPs : $SiO_2/TiO_2/SiO_2/TiO_2$ core/shell nanoparticles

T : temperature

t_{rec} : recovery time

t_{res} : response time

$\tan\delta$: dielectric loss tangent

TEM : transmission electron microscopy

TEOS : tetraethyl orthosilicate

TiO_2 : titanium dioxide, or titania

TTIP : titanium (IV) isopropoxide

V : volume

V_g : sedimentation velocity

XPS : X-ray photoelectron spectroscopy

$\dot{\gamma}$: shear rate

ε_0 : static permittivity

ε' : the dielectric constant

ε'' : dielectric loss factor

ε_∞ : fictitious permittivity

η : viscosity

η_∞ : viscosity at infinite shear rate

λ : relaxation time

v : relative velocity

ξ : geometric parameter

ρ : density

σ : electrical conductivity

τ : shear stress

τ_y : yield stress

φ : particle volume fraction

ω : angular frequency

$\Delta\varepsilon$: polarizability

List of Figures

Figure 5. (Color online) Sketches of the ER effect and the origin of its shear resistance. a) Side view, top view, and microscope top view of ER fluids under different electric fields E and shear states $\dot{\gamma}$. b) Electrostatic pair interaction between particles in the traditional polarization model. c) Mechanical interaction induced by the electrostatic interaction between particles after these particles become shear thickened or jammed.

Figure 6. Working principle of the giant electrorheological fluid (GERF). a) GERF stays in the liquid state when no electric field is applied, begins to form chains when an electric field is applied, then grows into columns when the electric field increases. b) When no electric field is exerted, GERF keeps flowing because it is pumped, and when the electric field is applied on GERF by embedded parallel plate electrodes, GERF solidifies. A large enough electric field will provide very high yield stress of GERF, resulting in a fluid suspending effect.

List of Tables

Table of Contents

1. INTRODUCTION

1.1. Background

1.1.1. Stimuli-responsive smart material

Smart materials, which respond to external stilmuli, such as temperature, pH, light, redox, glucose, enzyme, mechanical force, and electric or magnetic field, have attracted a great deal of interest from industry and academic researchers (Figure 1) [1–5]. Stimuli-responsive smart materials have grabbed considerable focus and attention to be applied to various fields because of their adjustability of response according to environmental conditions [6–12]. Since external stimuli leads to changes in structure, dimension, and interactions of the intelligent materials, it is possible to regulate the location and rate of response, which is a crucial advantage of the stimuli-responsive smart material. Depending on the mechanisms of response, the stimuli-responsive smart materials have been applied in various fields [13–21].

pH-responsive material, one of representative smart material, is widely utilized in biological and medical applications such as drug delivery and release system [22–28]. These delivery systems function based on the physical and chemical changes of materials with respect to a pH signal, for instance, swelling, bond cleavage, and charge conversion (Figure 2) [29–33]. Particularly, the strategies of utilizing the materials having acid-cleavable

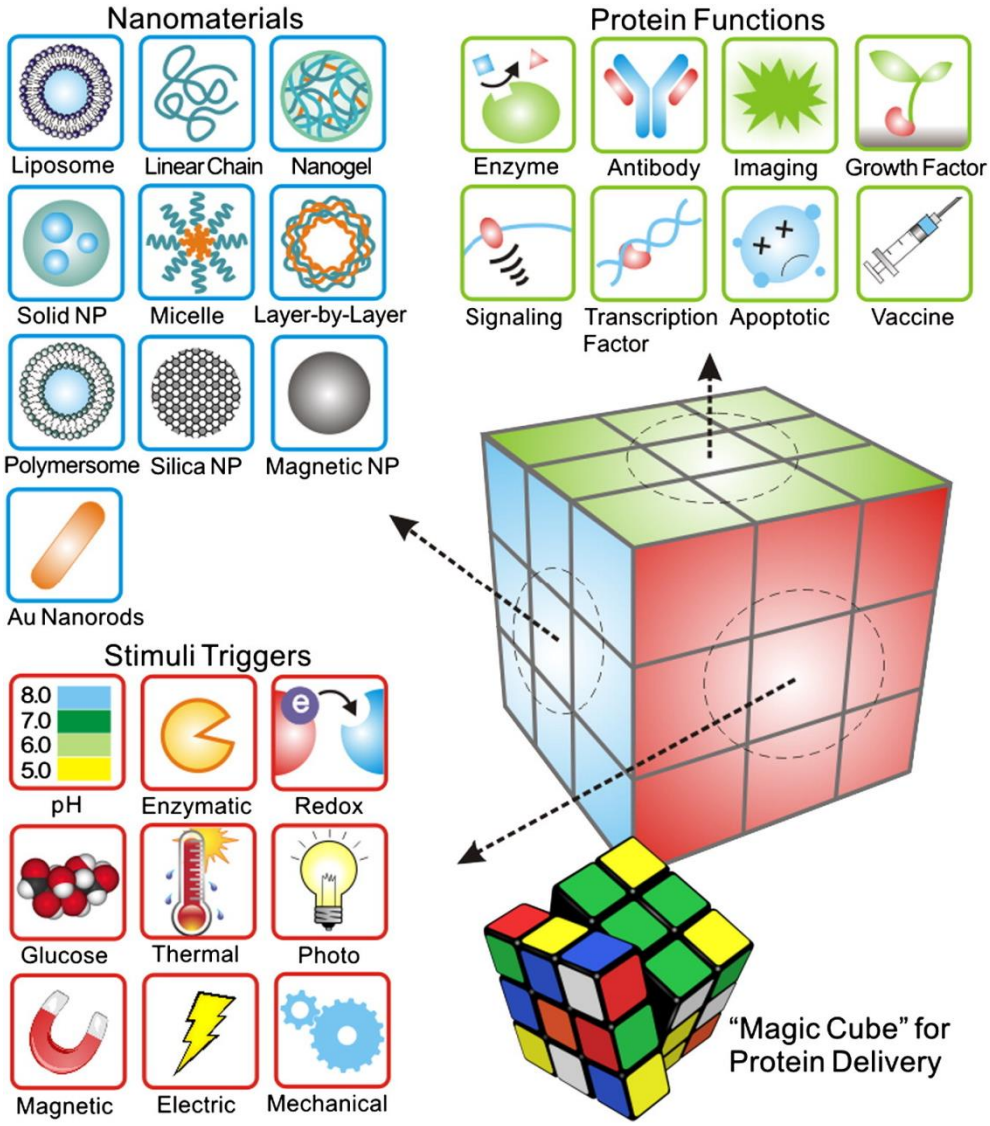

Figure 1. Schematic of "Magic Cube" for protein delivery: combination of a variety of triggeringmechanisms and carrier formulations for delivery of a broad spectrumof functional proteins. Reprinted with permission. Copyright 2014 Elsevier.

bonds or copolymers with ionizable groups have been typically incorporated for the intracellular delivery and oral delivery.

Temperature-responsive material, or thermo-responsive material, is another representative smart material that displays a drastic variation in response to temperature [34–37]. A predominant factor governing the change phenomenon of the temperature-responsive material is the balance of hydrophobic and hydrophilic moieties on the material (Figure 3). Since most of the termal stimuli-responsive material exhibits a lower critical solution temperature (LCST) behavior, it is possible to trigger releasing of drugs at tumor sites because the local temperature of tumor sites is generally higher thatn that of normal tissue. This characteristic phenomenon is useful in biomedical applications [38–43].

Among the various stimuli-resonsive smart materials, the electro-responsive and magneto-responsive materials are considered as the most feasible candidate for practical applications. In particular, when the electro-responsive and magneto-responsive materials are applied to smart fluids, the practicability is significantly high due to their controllable mechanical and rheological properties depending on the external field on and off [44–50]. Moreover, the electro-responsive and magneto-responsive materials also can be used as a drug carrier because they represent phase transition depending on the

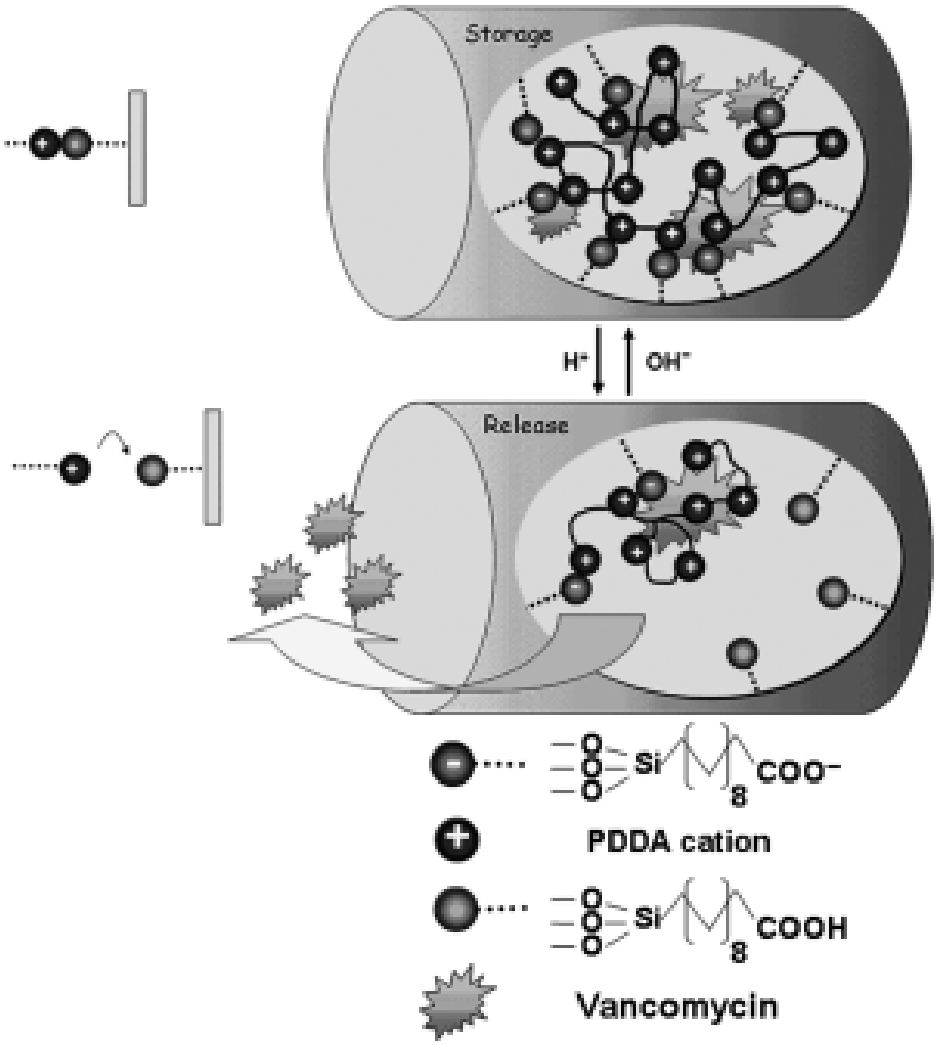

Figure 2. pH-responsive storage–release drug-delivery system based on the interaction between negative carboxylic acid modified SBA-15 silica rods with polycations (PDDA). Reprinted with permission. Copyright 2007 Wiley-VCH Verlag GmbH & Co. KGaA.

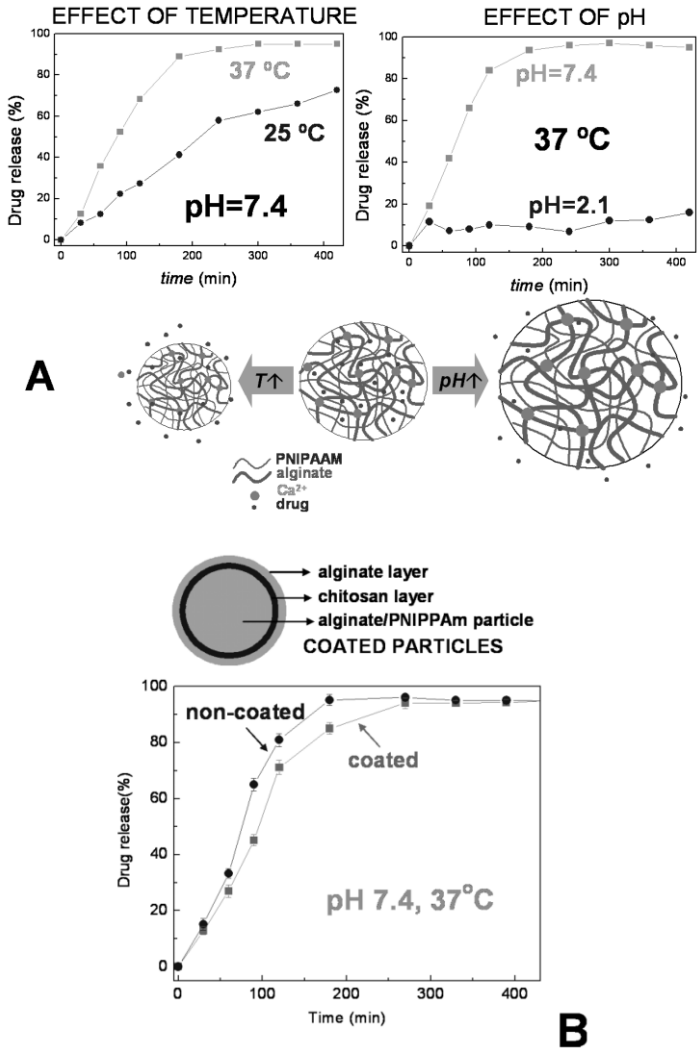

Figure 3. a) Temperature and pH influence on the release of indomethacin in semi-interpenetrating polymer networks, in the form of hydrogel beads, composed of alginate and poly(N-isopropylacrylamide); the scheme shows the influence of such parameters on the swelling of the particles. b) the same particles, subjected to a coating process with chitosan and alginate (see scheme) exhibit a significant slower release profile for indomethacin as compared with the uncoated. Reprinted with permission. Copyright 2008 Wiley-VCH Verlag GmbH & Co. KGaA.

external field conditions [51–55].

Besides, diverse stimuli-respnosive materials have received a lot of attention and emerged as next-generation materials for applications in controlled drug delivery system, shape memory composites, self-healing application, muscle-like actuator, shape memory materials, sensors, micro- and nano-fluidic devices [56–70].

1.1.2. Electro-responsive material

Electro-responsive materials can be defined as the materials that exhibit controllable properties, such as physical properties and mechanical properties, in response to electric field [71–74]. Because of the adjustability of properties, the electro-responsive materials have been utilized in several applications. In particular, the electro-switchable characteristics of the electro-responsive materials are favorable for applying them to engineering fluids. Electro-responsive fluid, or electrorheological (ER) fluid, is a type of smart fluid that consists of polarizable electro-responsive material and an insulating liquid medium [75–79]. ER effect, also called the *Winslow* effect, is first discovered in 1940s by Willis M. Winslow [80]. The rheological and mechanical features of ER fluids are controllable in response to external electric field. In accordance with and without an external electric field, the alternation of a solid-like state and a liquid-like state take places reversibly. This state transition is ascribed to dipole–dipole interactions between the polarized electro-resonsive materials under an applied electric field (Figure 4). Electro-responsive materials can be categorized into organic and polymeric material, inorganic oxide, and non-oxide inorganic material.

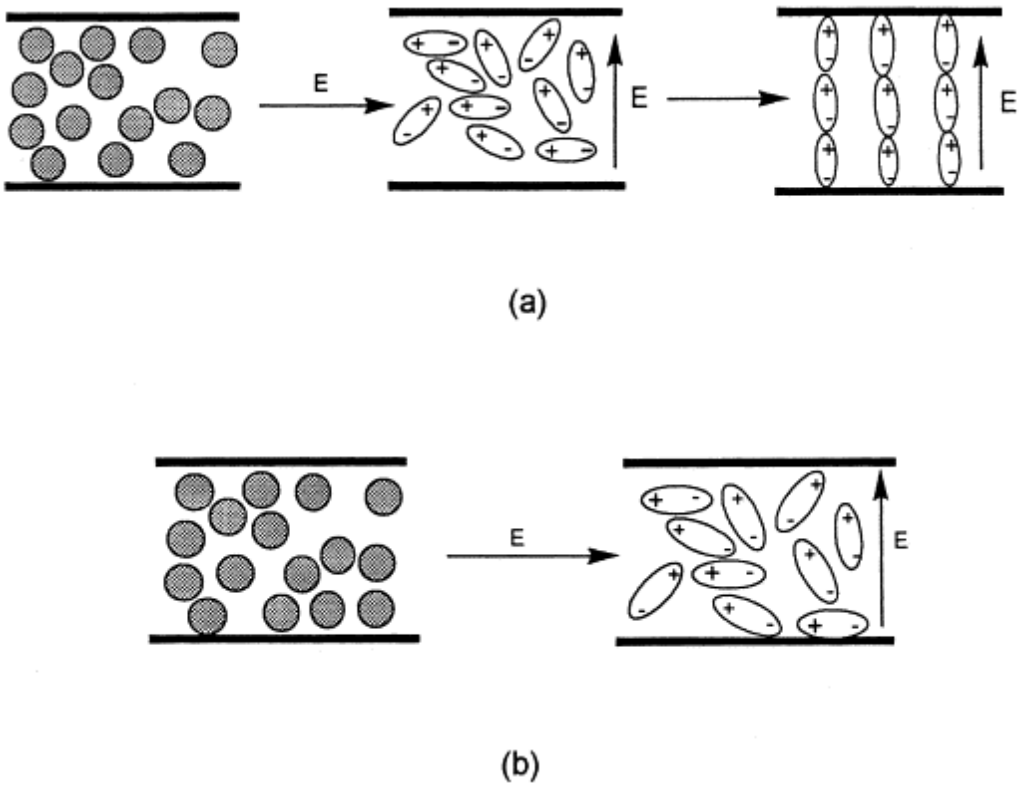

Figure 4. Schematic illustration of the ER particles and the non-ER particle behaviors before and after an external electric field is applied. a) ER particle; b) non-ER particle. Reprinted with permission. Copyright 2002 Elsevier.

1.1.2.1. Organic and polymeric material

Organic and polymeric material which is one of representative electro-responsive material can be devided into two categories. The first is the material composed of conjugated π bonds [81–85]. The electrical conductivity of these materials can be adjusted by doping metallic ion or metallic oxide and controlling the carbonation temperature. This class of material having a conjugated π bond generally exhibits high dielectric constant and can be highly polarized under an electric field. The second is the material containing highly polarizable groups, such as hydroxyl, amino, and cyano group, on the molecular chain [86–88]. Polyelectrolytes come under this kind of material which has high charge density.

Since the organic and polymeric material is soft, it does not scratch on the surface of device, which is in contrast with inorganic material. However, ER effect of the organic and polymeric material-based fluid is weaker than that of non-oxide inorganic-based fluid. To maximize advantages and complement disadvantages of the organic and polymeric material, several approaches have been suggested. For instance, conducting polymers, including polypyrrole, polythiophene, polyaniline, and poly(3,4-ethylenedioxythiophene), have emerged as a fascinating ER material due to their excellent intrinsic polarizability, low density, and facile change in conductivity [89, 90].

Outstanding electrical and electrochemical properties which are attributed to π-conjugated carbon backbone structures lead to high ER performance. In case of coating the conducting polymer on the surface of inorganic particles, it is possible to not only supplement the drawback of inorganic material abrading the surface of device but also achieve high ER effect [91, 92]. Another electro-responsive organic material recently spotlighted is graphene oxide (GO) because of its distinguiching features, such as high polarizability, and excellent dispersion stability in both aqueous and organic solvents [93–95]. Because GO contains functional groups, including hydroxyl, carboxylic, and epoxy groups, on its edges and basal planes, it displays low electric conductivity, which is an appropriate feature for ER application. Numerous researches regarding on electro-response of graphene-based materials, such as size-controlled GO sheets, GO/polyaniline composites, and titanium dioxide nanorod-decorated graphene sheets, and have been reported [96–100]. However, most of studies on electro-response of GO-based material have been focused on a two-dimensional planar structure which is inherent structure of graphene. It remains challenging to examine electro-response of GO-based material in tems of other configurations (*e.g.*, a zero-dimensional (0-D) or one-dimensional (1-D) shape).

1.1.2.2. Inorganic oxide

Some ceramic materials and metallic oxides have been regarded as one of the most acclaimed candidates for electro-responsive material due to their ease of manufacture and possibility of modification. Silicon dioxide, or silica (SiO_2), is one of the most representative materials for an application to electro-responsive fluids. Since it is facile to control the shape and size as well as modify the surface of SiO_2, various types of SiO_2 with different shape and size has been synthesized and applied as a template for preparation of core/shell particles [101–103].

Titanium dioxide, or titania (TiO_2), is another good candidate for electro-responsive material exhibiting superior ER performance due to its high dielectric properties. Various structures of TiO_2 materials have been fabricated and utilized as an electro-responsive material in order to acquire high ER efficiency. Among the various TiO_2 materials, hollow structure has received a great deal of attention because of its high polarization force and dispersity. Moreover, Cheng and coworkers synthesized TiO_2 hollow spheres having TiO_2 branches to achieve superior ER performance by increasing active surface area [104]. In addition to pristine TiO_2 material, a variety of TiO_2 and its derivatives, for instance, metal-doped TiO_2, polypyrrole-coated TiO_2 hollow nanoparticles, rare earth-doped mesoporous TiO_2, and kaolinite/TiO_2, have been adopted as a

dispersed material of ER fluid [105, 106].

1.1.2.3. Inorganic non-oxide

Inorganic non-oxide material can be adopted as a good ER material because it exhibits a significantly strong ER effect under an electric field [107–110]. Researches on inorganic non-oxide material-based ER fluids were chiefly amplified in the late 1980s and early 1990s. Among the inorganic non-oxide materials, aluminosilicates, silicates, and zeolite family materials have received a lot of focus for ER application [111–114].

1.1.3. Critical parameters to electro-response

ER behavior is affected by several parameters, such as particle volume fraction, dielectric property, electrical conductivity, electric field strength, and geometrical feature of material (*i.e.* size and shape). Studies on critical parameter to ER performance have been progressed steadily since the ER efficiency varies depending on several parameters [115–117]. For instance, Choi's group demonstrated a relationship between yield stress of ER fluid and electric field strength [118–120]. In addition, Hao and coworkers described an influence of particle volume fraction and electric field strength on shear behavior of ER fluid [121]. Moreover, an effect of particle size to ER activity was investigated by fabricating and adopting three different-sized polyaniline/poly(styrene sulfonate)-coated silica spheres [122]. Although many researches regarding the critical parameters to electro-response have been proposed, a more in-depth study is required to clarify how the critical parameters affect the ER performance.

1.1.3.1. Size and shape of material

It has been reported that size and shape of ER material have a significant impact on ER behavior. On the other hand, the experimental results of researches on the effect of particle size on ER efficiency were different. According to the theoretical prediction, it was expected that the too small-sized particles exhibit weak ER performance since the Brownian motion competes with particle fibrillation. On the contrary, when the particle size is too large, ER effect is also small due to sedimentation of particles in liquid medium that interrupts formation of fibrillar structure. However, the actual experimental results revealed that the relationship between the particle size and ER performance is not simple. In previous research using $BiTiO_3$ nanoparticles with different diameter as ER material, it was addressed that the ER fluid composed of smaller particle represented stronger ER effect at low electric fields and similar ER effect at high electric fields compared with larger particle [123]. In addition, another examination on ER behavior of fumed silica figured out that apparent viscosity and yield stress of ER fluid increased as the particle size decreased [124]. The high ER efficiency of small-sized particle can be ascribed to the dense and rigid fibil-like structures that withstand against hydrodynamic force generated by flow.

Relatively few studies on an influence of particle geometry on ER behavior

have been demonstrated. According to the previously reported research, ER activity of ellipsoidal particle is stronger than that of spherical particle because of the strengthened chain structures resulted from the greater electric-field-induced moment [125]. ER properties as a function of aspect ratio (length-to-diameter) can be depicted in relation to dielectric constant [126].

It is obvious that ER activity is associated with the size and shape of particle. However, since there are many other parameters affecting ER properties, such as electric field strength and shear rate, it is required to identify the ER behavior when other conditions and parameters are comparable.

1.1.3.2. Electrical conductivity

Electrical conductivity of the dispersed material has an effect on ER properties. Block and coworkers revealed how electrical conductivity of the material affects ER behavior [127]. From the experimental proof, the maximum yield stress of fluid appeared at a conductivity of *ca.* 10^{-5} S m^{-1} for the acene-quino radical polymer and *ca.* 10^{-5} S m^{-1} for the oxidized polyacrylonitrile respectively [128]. In addition to the yield stress, the electrical conductivity of material manipulates the response time and current density of ER fluid. It has been theoretically and experimentally verified that the electrical conductivity and response time are inversely related [129, 130]. In accordance with the previous studies, shear modulus and forces between the particles induced by an applied electric field are determined depending on the dielectric constants of both the dispersed material and liquid medium at high frequency of electric fields (> 0.1–1 kHz) [131]. On the other hand, at low frequency of electric fields or dc electric fields, the electrical conductivity decides shear modulus and forces between the particles generated by an electric field. Moreover, if the electrical conductivity of the dispersed material is higher than that of liquid medium, the ER performance would be decided by the ratio of electrical conductivity of the dispersed material to liquid medium, corresponding to the conductivity model [132, 133].

Though the electrical conductivity is a very important parameter to ER activity, few experimental investigations have been provided an impact of electrical conductivity on ER efficiency. To specify the dependence of ER properties on electrical conductivity, a more in-depth study is needed by regulating the electrical conductivity of the electro-responsive material without any other changes.

1.1.3.3. Dielectric property

Dielectric property of the electro-responsive material is regarded as a dominant parameter in ER activities because it determines the polarizability of material which is a critical factor to ER performance. Dielectric property of the electro-responsive material varies on applied electric field strength, particle volume fraction, and water content adsorbed on surface of material. It has been verified that the dielectric property is enhanced in proportion to particle volume fraction, which is attributed to electric double layer overlapping [134]. On the other hand, Klass *et al.* revealed that dielectric property can be decreasing, constant or increasing depending on the particle volume fraction as applied electric field strength increases [135]. In addition, some researches illustrated that the dielectric property was enhanced in proportion to the electric field strength at high electric field [136].

Relationship between dielectric property of the dispersed material and ER

behavior has been considered as an important subject. Since the liquid medium typically used for ER fluid is silicone oil, which has a dielectric constant of *ca.* 2, a lot of attention has been focused on dielectric constant of the dispersed particle. The polarization model, one of the most popular theories for describing the mechanism of ER phenomenon, is related to dielectric property of the dispersed material [137–140]. In the polarization model, yield stress is attributed to the fibrillation occurred by electrostatic interactions between the particles and the Maxwell–Wagner interfacial polarization. The electrostatic force is induced by the dielectric constant mismatch between the solid dispersed particles and liquid medium (Figure 5). However, the physical fundamentals of ER behavior are not sufficiently covered in the polarization model. Especially in some systems under high electric field strength, the activities of ER fluid were not matched with the polarization model. Another popular theory for explaining the mechanism of ER phenomenon is the conduction model. The conduction model accounts for the particle interactions after fibrillation of particles. In the conduction model, it is suggested that the particle interaction is mainly determined by the ratio of dielectric constant of particle to fluid rather than that of electrical conductivity [141, 142]. However, the microstructural changes of ER suspension under an applied electric field, transition from a randomly dispersed state to an ordered fibil structured state,

were not elucidated in the conduction model. In other words, the conduction model does not give an adequate interpretation of a field-induced response process. In addition, several theoretical approaches for clarifying the mechanism of ER phenomenon have been proposed [143–150]. In particular, it has been proved that a high dielectric constant and a dielectric loss tangent would be required to obtain a high ER efficiency [151].

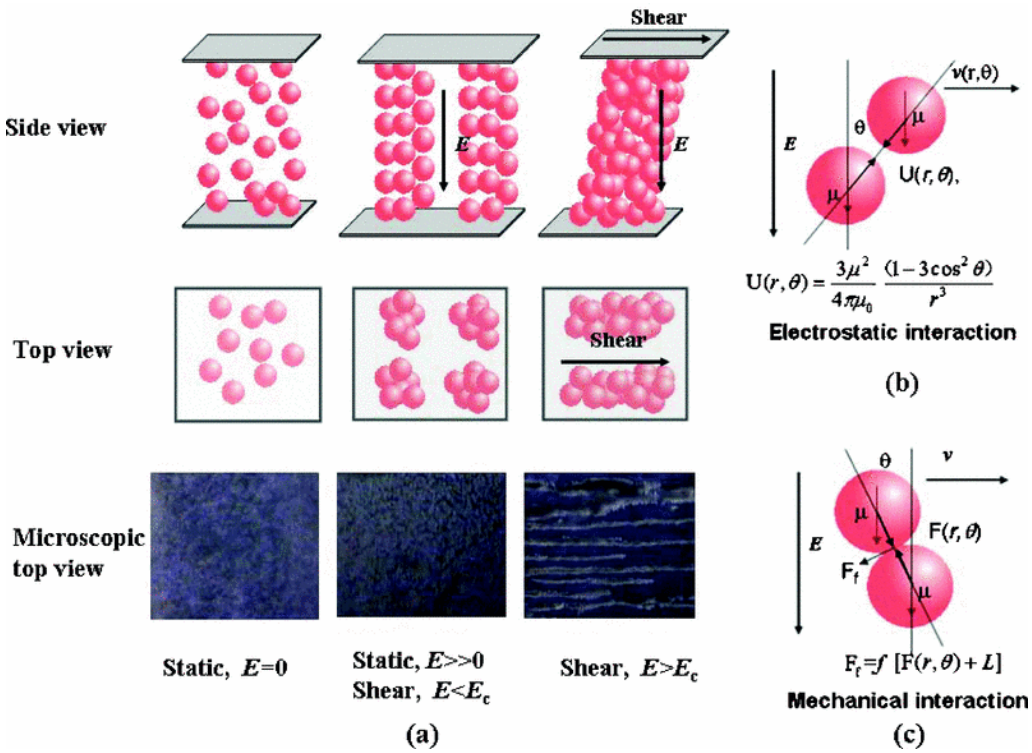

Figure 5. (Color online) Sketches of the ER effect and the origin of its shear resistance. a) Side view, top view, and microscope top view of ER fluids under different electric fields E and shear states $\dot{\gamma}$. b) Electrostatic pair interaction between particles in the traditional polarization model. c) Mechanical interaction induced by the electrostatic interaction between particles after these particles become shear thickened or jammed. Reprinted with permission. Copyright 2011 American Physical Society.

1.1.3.4. Electric field strength

Electric field strength is critical to ER performance since an electro-responsive material responds to an electric field. It has been reported that the yield stress increases in proportion to an applied electric field strength (Figure 6) [152]. The relationship between the yield stress and electric field strength is expressed as follows:

$$\tau_y = k\,(E - E_c)$$

where τ_y denotes the yield stress of ER fluid, k is a constant, and E and E_c indicate an applied electric field strength and a critical electric field strength respectively. Beyond critical electric field strength, ER fluid exhibits ER characteristics.

Further investigation on the correlation of an applied electric field strength and dynamic yield stress was provided by Liu *et al*, demonstrated as follows:

$$\tau_0 \propto E^m$$

where τ_0 represents the dynamic yield stress, and m is a variable typically in the range of 1.0–2.0 in an empirical distribution [153–155]. Judging from the several experimental results, it was confirmed that the dynamic yield stress depending on an applied electric field was fitted on a line with a slope of 2.0 for the polarization model and 1.5 for the conduction model in a logarithmic graph [156, 157].

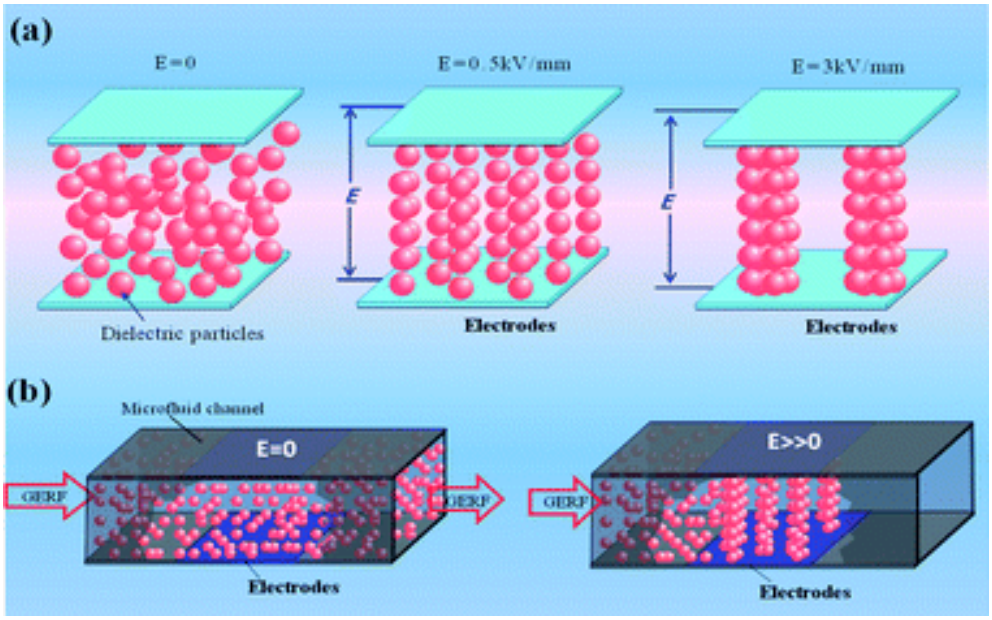

Figure 6. Working principle of the giant electrorheological fluid (GERF). a) GERF stays in the liquid state when no electric field is applied, begins to form chains when an electric field is applied, then grows into columns when the electric field increases. b) When no electric field is exerted, GERF keeps flowing because it is pumped, and when the electric field is applied on GERF by embedded parallel plate electrodes, GERF solidifies. A large enough electric field will provide very high yield stress of GERF, resulting in a fluid suspending effect. Reprinted with permission. Copyright 2010 The Royal Society of Chemistry.

1.1.4. Application fields

ER fluids have attracted a great deal of attention in various fields because of their distinguishing features, such as rapid reversible transition, simple fluid mechanics, and low power consumption. Fast response time and reversibility of ER fluids are suitable for applications in an electric–mechanical interface, for instance, damper (shock absorber), brake, clutch, squeeze mount, engine mount, and valve. Particularly, a great interest has been focused on damping device, including robot arms, bering damper, engine mount, and seismic controlling frame structure since it does not demand substantially high yield stress and wide operating temperature range (Figure 7) [158–160]. Furthermore, ER fluids can be applied to human muscle stimulator, mechanical polisher, photomic crystal, display, light shutter, and ink jet printer [161–163]. Recently, in vitual reality applications such as medical haptic device, ER fluid was adopted in a tactile array and successfully performed [164]. It is expected that more applications of ER fluid would be developed and expanded in the future.

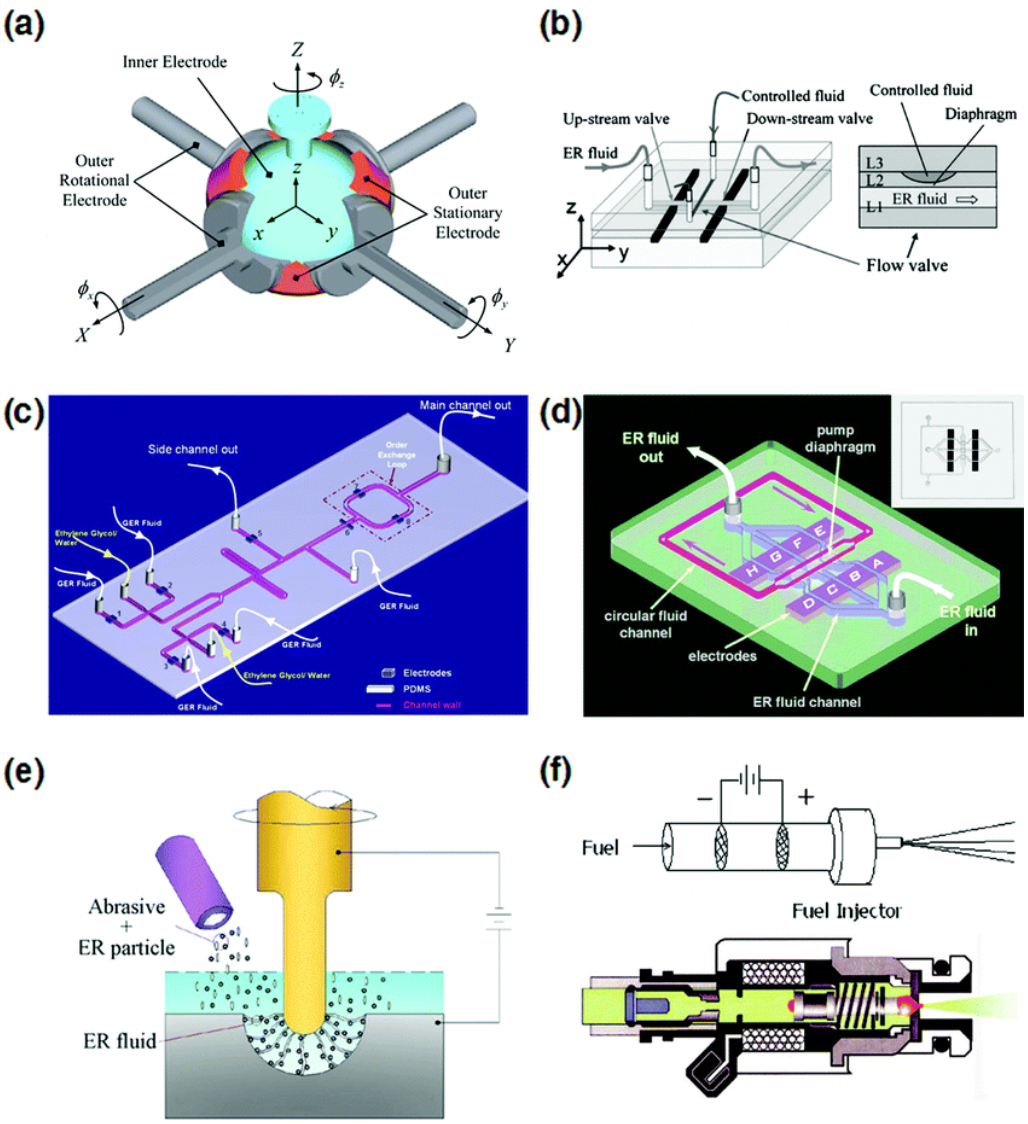

Figure 7. Schematic illustrations of a) the spherical ER joint for the haptic master device, b) the four-port micro-GER valve, c) the ER microfluidic chip, d) the ER microfluidic pump, e) the combined technology of electrical discharge machining with polishing by using ER fluid, and f) the design of the fuel injector with ER. Reprinted with permission. Copyright 2012 The Royal Society of Chemistry.

1.2. Objectives and Outline of the Study

1.2.1. Objectives

In the preceding section, the importance of electro-responsive smart material was introduced from the viewpoint of academic research and practical applications. The aim of this dissertation is to present electro-responsive characteristics depending on different critical parameters, including particle geometry, dielectric property, and electrical conductivity, by adopting three different categories of materials. Furthermore, the mechanism underlying the electro-responsive behavior of smart fluid is systematically scrutinized.

1.2.2. Outline

This dissertation involves the following subtopics:

I. Electro-Responsive Characteristics Depending on Particle Aspect Ratio

1. Fabrication of various graphene oxide (GO)-wrapped silica materials
2. Electro-response of GO-wrapped silica material-based fluids
3. Influence of particle aspect ratio on electro-responsive behavior

II. Electro-Responsive Performance Depending on Particle Shell Structure

1. Fabrication of size-controlled double-shell SiO_2/TiO_2 hollow nanoparticles
2. Influence of the number of SiO_2/TiO_2 shell on electro-responsive

property

3. Electro-responsive activity of double-shell SiO_2/TiO_2 hollow nanoparticles depending on particle size

III. Electro-Responsive Behavior Depending on Electrical Conductivity

1. Fabrication of few-layer MoS_2 nanosheets
2. Characteristic analysis of few-layer MoS_2 nanosheets depending on annealing temperature
3. Effect of electrical conductivity on electro-responsive behavior

A detailed outline of the study is as follows:

1. As an electro-responsive material, the GO-wrapped silica materials with different aspect ratios are successfully fabricated by using a facile and straightforward method. To achieve an in-depth insight into the influence of particle geometry on electro-responsive fluid, the electro-responsive property of GO-wrapped silica material-based fluids are investigated under various experimental conditions, such as shear rate and electric field strength. From an in-depth analysis of electro-responsive activities, it is revealed that the ER performance improves as the aspect ratio of material increases, which can be elucidated by the geometrical effect (*e.g.* flow resistance and mechanical stability) and dielectric properties of the electro-

responsive materials. This meticulous investigation may offer an opportunity for the further application of other materials as electro-responsive materials.

2. It is noteworthy that double shell SiO_2/TiO_2 hollow nanoparticles are successfully synthesized and introduced into electro-responsive smart fluid in order to achieve an in-depth insight into the influence of shell structure on ER activities. The electro-responsive performance is significantly enhanced as the number of shells increases, which can be explained by the enhanced interfacial polarization. In addition, ER performance of the double shell SiO_2/TiO_2 hollow nanoparticles is observed to increase with decreasing the particle diameter, which is attributed to the enhanced achievable polarizability of the smaller particles. The double shell SiO_2/TiO_2 hollow nanoparticles exhibit excellent ER performance as well as superior anti-settling property, which is enough to promise sufficient probability for practical or industrial applications.
3. Few-layer MoS_2 nanosheets, one of graphene analogues and layered transition-metal dichalcogenides, are successfully prepared through mild grinding and delamination process using sonication. To demonstrate the dependence of electro-responsive characteristics on the electrical conductivity of material, the electrical conductivity of the few-layer MoS_2

nanosheets is controlled by adjusting the annealing temperature. It is confirmed that electro-responsive behavior of the few-layer MoS_2 nanosheets-based ER fluid depending on the electrical conductivity corresponds to the Wagner's model which describes the interfacial polarization existing in a heterogeneous system. It is noticeable that an intensive study on the effect of electrical conductivity on electro-responsive characteristics is carried out. Furthermore, this study provides the possibility of transition-metal dichalcogenides as a candidate of ER material.

2. EXPERIMENTAL DETAILS

2.1. Electro-Responsive Characteristics Depending on Particle Aspect Ratio

2.1.1. Preparation of various silica materials

Uniform silica spheres were synthesized according to the Stöber method [165, 166]. First, tetraethyl orthosilicate (TEOS, 4.33 mL) was slowly added to a solution composed of ethyl alcohol (40 mL), distilled water (6.4 mL), and ammonium hydroxide (8.46 mL) at room temperature. For sol-gel reaction, the resulting solution was stirred for 3 h at room temperature. The products were washed with ethyl alcohol three times (at 6,000 rpm for 20 min) and dried in a vacuum oven at 40 ℃.

Silica rod was fabricated by a facile one-pot method [167–169]. First of all, 5 g of polyvinylpyrrolidone (PVP, average molecular weight M_n = 40,000) was dissolved in 1-pentanol (50 mL) using sonication for 2 h. Then, distilled water (1.4 mL), ethyl alcohol (5 mL), 180-mM sodium citrate solution (0.5 mL), and ammonium hydroxide (0.85 mL) were added to 1-pentanol solution containing PVP. The solution was shaken using a vortex mixer for 1 min to completely mix the contents and then left to stand for 5 min. Subsequently, TEOS was slowly added dropwise to the solution while shaking the bottle containing the solution by hand. The products were washed with ethyl alcohol several times

(at 6,000 rpm for 20 min) and dried in a vacuum oven at 40 ℃. The diameter of the fabricated rod-like silica was *ca*. 200 nm. The length of silica rod was controlled by adjusting the amount of TEOS.

2.1.2. Fabrication of various GO-wrapped silica materials

Nanometer-sized GO was prepared through a ball-mill process to uniformly wrap the silica materials. Initially, pristine graphite (<20 μm) was placed in the mortar of a ball-milling apparatus containing zirconium oxide balls (diameters: 1, 2, and 5 mm). Subsequently, the container was fixed in the ball-milling machine and agitated at a rolling speed of 550 rpm for 12 h. The ball-milled graphite was oxidized and formed into GO nanosheets using a Hummers method [170, 171]. First of all, for pre-oxidization, the ball-milled graphite (1.0 g) was added to the solution composed of H_2SO_4 (1.5 mL), $K_2S_2O_8$ (0.5 g), and P_2O_5 (0.5 g), and heated at 80 ℃ for 6 h. The resulting solution was diluted and washed with distilled water *via* a vacuum-filtration process, and dried in air overnight. The dried powder was added to the H_2SO_4–$NaNO_3$ solution, and stirred for 30 min at 0 ℃. After adding $KMnO_4$ (3.0 g) to the solution at 20 ℃, the mixture was carefully stirred for 45 min. Subsequently, the temperature rose to 35 ℃ while stirring for 2 h. After adding distilled water (46 mL) to the solution, the temperature increased to 98 ℃ with slow stirring for 15 min.

Once the color of the solution turned into a brilliant brown, indicating a fully oxidized state, then H_2O_2 solution (30%) was added dropwise to the solution at room temperature. Finally, the product solution was washed with distilled water using a vacuum filtration process and dried overnight.

GO nanosheets were deposited to the surface of the silica materials by electrostatic interaction between oppositely charged components [172, 173]. First of all, dried silica materials were evenly redispersed in ethyl alcohol using sonication. To obtain the positively charged silica materials, the surface of silica was functionalized with amine groups by 3-aminopropyltrimethoxysilane (APS) treatment for 12 h. After adding dried GO nanosheets to distilled water, GO solution was prepared using sonication in order to uniformly disperse GO nanosheets. Since the surface of GO nanosheets was negatively charged because of chemical functional groups, such as hydroxyl and carboxyl groups, the amine-functionalized silica materials were coated with the GO nanosheets when the GO solution was added into the solution containing amine-functionalized silica materials. After stirring for 12 h at room temperature, the resulting products were acquired through washing with ethyl alcohol and distilled water several times at 4,000 rpm for 30 min, and drying overnight.

2.1.3. Influence of particle aspect ratio on electro-responsive behavior

Transmission electron microscopy (TEM) images were acquired by a JEM-2100 (JEOL). Electro-responsive behavior of GO-wrapped silica material-based ER fluids was evaluated using a rheometer (AR 2000 Advanced Rheometer, TA Instruments) with a concentric cylinder conical geometry having a cup radius of 15 mm, a high-voltage generator (Trek 677B), and a temperature controller. Energy dispersive X-ray spectroscopy (EDS) was carried out using a field-emission scanning electron microscopy (FE-SEM) (JSM-6701F, JEOL), equipped with an EDS system (INCA Energy, Oxford Instruments Analytical Ltd.). Permittivity of GO-wrapped silica material-based fluids was measured by an impedance analyzer (1260, Solartron) combined with a dielectric interface (1296, Solartron).

2.2. Electro-Responsive Performance Depending on Particle Shell Structure

2.2.1. Fabrication of size-controlled double-shell SiO_2/TiO_2 hollow nanoparticles

Various size of silica nanoparticles were synthesized according to the Stöber method [165]. Titanium (IV) isopropoxide (TTIP) was added dropwise into the colloidal solution of silica nanoparticles, blended with ethyl alcohol (18 mL), and acetonitrile (6 mL). This colloidal solution reacted at 4 ℃ for 6 h to obtain SiO_2/TiO_2 core/shell nanoparticles (ST CS NPs). The solution was centrifuged for 20 min at 12,000 rpm and dispersed in distilled water (80 mL). The solution containing the ST CS NPs was stirred with PVP (M_w of 1,300,000) for 12 h to coat PVP onto the surface of the ST CS NPs. The PVP-coated ST CS NPs were centrifuged and redispersed in ethyl alcohol (158 mL). The ST CS NPs solution was mixed with ammonium hydroxide (2 mL) and distilled water (1.4 mL). TEOS (5.8 mL) was dropped to the ST CS NPs solution and stirred for 4 h to form silica shell on the surface of the ST CS NPs. A solution of silica-coated ST CS NPs (STS CS NPs) was mixed with TTIP (5.8 mL), ethyl alcohol (9mL), and acetonitrile (3mL). Through the sol–gel reaction, $SiO_2/TiO_2/SiO_2/TiO_2$ core/shell nanoparticles (STST CS NPs) were produced. Double-shell SiO_2/TiO_2 hollow nanoparticles (DS HNPs) were acquired *via*

etching and redeposition process using sonication with ammonium hydroxide (0.1 M) [174]. By centrifugation of the resulting solution at 12,000 rpm for 10 min and washing with ethyl alcohol twice, the final products were abtained.

2.2.2. Influence of the number of SiO_2/TiO_2 shell on electro-responsive property

Dried particles were dispersed in silicone oil (poly(methylphenylsiloxane), viscosity = 100 cSt) and stirred with magnetic stirrer to disperse the particles uniformly. Concentration of the ER fluids was 10 wt% and no additives were added into the ER fluid. All ER fluids were prepared by the same method. ER behavior of the prepared fluids were measured using rheometer (AR 2000 Advanced Rheometer, TA Instrument) with a concentric cylinder conical geometry, a temperature controller, and a high voltage generator (Trek 677B). The gap distance between the cup and rotor was 1.00 mm and the ER fluid was placed in that space. To get an equilibrium fibrillar structure, an electric field was applied for 3 min before starting measurement. All measurements were performed at room temperature.

TEM images were acquired by a JEM-2100 (JEOL). Total surface area and pore distribution were examined using a Micromeritics analyzer (ASAP 2000; Micromeritics Co., Norcross, GA). Elemental composition of the particles was

acquired using elemental analyzer (EA1110, CE Instrument) and Inductively Coupled Plasma-Atomic Emission Spectrometer (ICPS-7500, SHIMADZU Corporation, Japan). Scanning transmission electron microscopy-energy dispersive spectroscopy (STEM-EDS) elemental maps were acquired using scanning transmission electron microscopy (STEM, Tecnai F20, FEI) equipped with a Gatan image filter (Gatan, Inc.). The dielectric spectra of the ER fluids were obtained by an impedance analyzer (1260, Solartron) combined with a dielectric interface (1296, Solartron).

2.3. Electro-Responsive Behavior Depending on Electrical Conductivity

2.3.1. Fabrication of few-layer MoS_2 nanosheets

Molybdenum (IV) disulfide (MoS_2, powder, <2 μm, 99%) was exfoliated by grinding and sonication. First, MoS_2 powders (4.0 g) were ground with NMP (4 mL) vigorously in a porcelain mortar for 30 min. The mixture was completely dried in a vacuum oven to remove all the solvents. Dried powders were dispersed in a mixture of ethyl alcohol (45 mL) and distilled water (55 mL) using sonication for 2 h. After eliminating the sediment from the dispersion, the resulting dispersion was centrifuged to collect exfoliated MoS_2 as powders in order to utilize them for the fabrication of ER fluids.

2.3.2. Characteristic analysis of few-layer MoS_2 nanosheets depending on annealing temperature

To gain an in-depth insight into the properties of the few-layer MoS_2 nanosheets depending on the annealing temperature, MoS_2 powders were heated at certain temperatures (313, 333, 353, and 373 K). The samples were annealed for 1 h and cooled down thoroughly at ambient conditions.

TEM images were taken by a JEM-2100 (JEOL). For the sample preparation, the suspension diluted in the mixture of ethyl alcohol and distilled

water was cast onto a copper grid. The topography of atomic force microscopy (AFM) was acquiured by a Digital Instrument Nanoscope IIIA (Veeco Instruments) in tapping mode using a silicon tip of which the resonance frequency is 320 kHz. Horiba scientific T64000 Raman spectrometer was used for analyzing the structures of MoS_2. The electronic behaviors were observed by Lambda 35 (PerkinElmer) UV-visible spectrometer and JASCO FP-6500 spectrofluorometer. X-ray photoelectron spectroscopy (XPS) spectra were acquired using Sigma probe (ThermoVG). The measurement of electrical conductivity was carried out by Loresta-GP/MCP-T610 (Mitsubishi) using a four-probe method. The dielectric spectra of the ER fluids were obtained by 1260 impedance analyzer (Solartron) connected with 1296 dielectric interface (Solartron). Optical micrographs of MoS_2-based ER fluids were taken with a microscope (Leica DM2500P).

2.3.3. Effect of electrical conductivity on electro-responsive behavior

Exfoliated MoS_2 nanosheets were redispersed in silicone oil (10 vol%), resulting in a homogeneous grey suspensions. The suspensions were prepared through mixing the powders with silicone oil and grinding the mixture in an agate mortar. Further sonication and mechanical stirring enhanced the uniformity of the fluids. For the characterizations depending on the annealing

temperature, MoS_2 powders were heated at certain temperatures (313, 333, 353, and 373 K) before and after mixing with silicone oils. After annealing for 1 h, the samples were cooled down thoroughly at ambient conditions. ER behaviors were examined by a rheometer (AR 2000 Advanced Rheometer, TA Instruments) with a concentric cylinder conical geometry whose cup radius is 15 mm, a temperature controller, and a high-voltage generator (Trek 677B).

3. RESULTS AND DISCUSSION

3.1. Electro-Responsive Characteristics Depending on Particle Aspect Ratio

3.1.1. Fabrication of various GO-wrapped silica materials

To investigate the relationship between the particle aspect ratio and electro-responsive activities, silica materials with various aspect ratios were fabricated and utilized as a template. Specific particle geometry of the fabricated various silica materials was confirmed by TEM analysis (Figure 8). Highly uniform silica spheres having an average diameter of 200 nm were successfully synthesized. Bullet-shaped silica rods were formed having a fixed diameter of *ca*. 200 nm and various lengths that are dependent on the reagent contents. The length of silica rod could be adjusted from *ca*. 220 nm to *ca*. 4 μm by varying the amount of silica precursor. The silica precursor used for synthesizing the silica materials was TEOS that reacted with silica *via* a hydrolysis reaction followed by a condensation reaction.

Nanometer-sized GO sheets were prepared through a ball-mill process in order to be introduced onto the surface of silica materials for an enhancement of ER efficiency (Figure 9). The nanometer-sized GO sheets were successfully coated on the surface of silica materials by a simple electrostatic interaction (Figure 10–12). Since the GO nanosheets were negatively charged, it could be

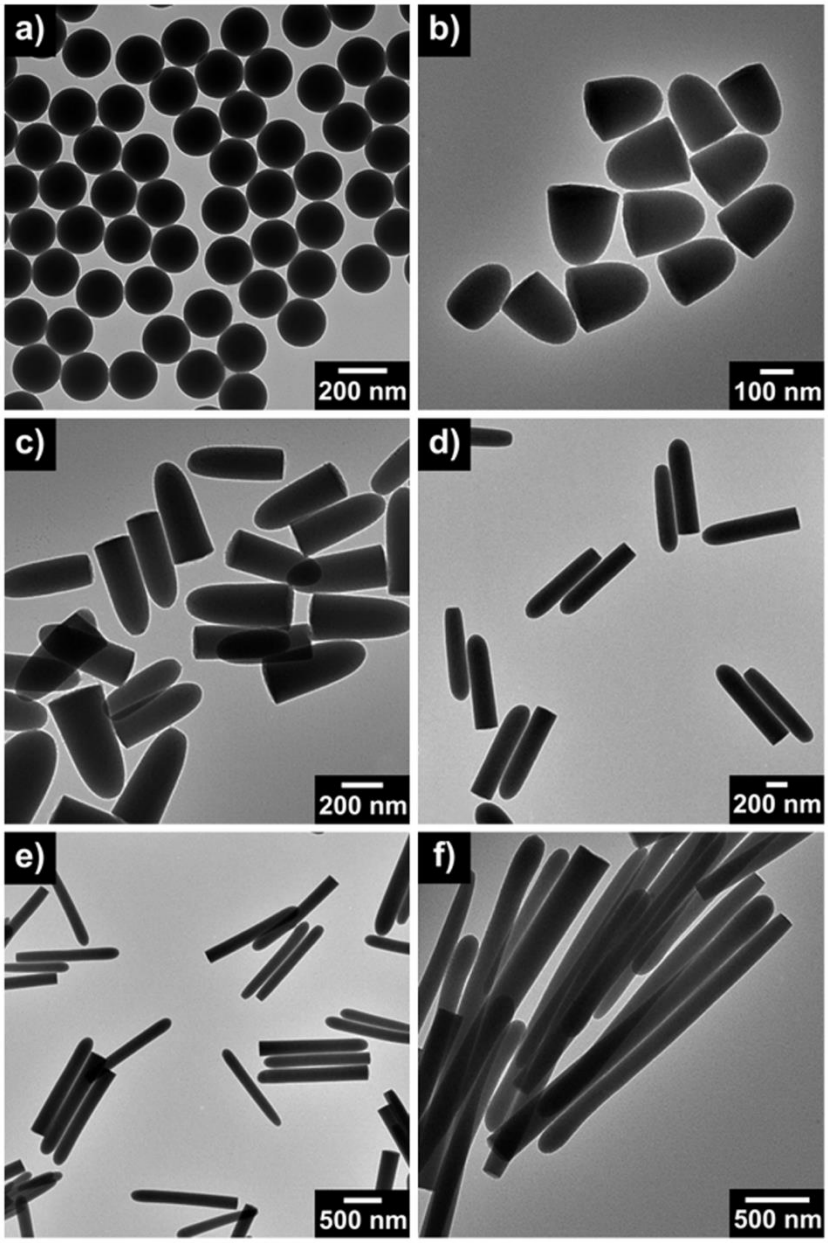

Figure 8. TEM images of a) silica spheres with 200 nm diameter, b) silica rods with an aspect ratio of 1.8, c) silica rods with an aspect ratio of 3.1, d) silica rods with an aspect ratio of 5.0, e) silica rods with an aspect ratio of 8.0, and f) silica rods with an aspect ratio of 20.

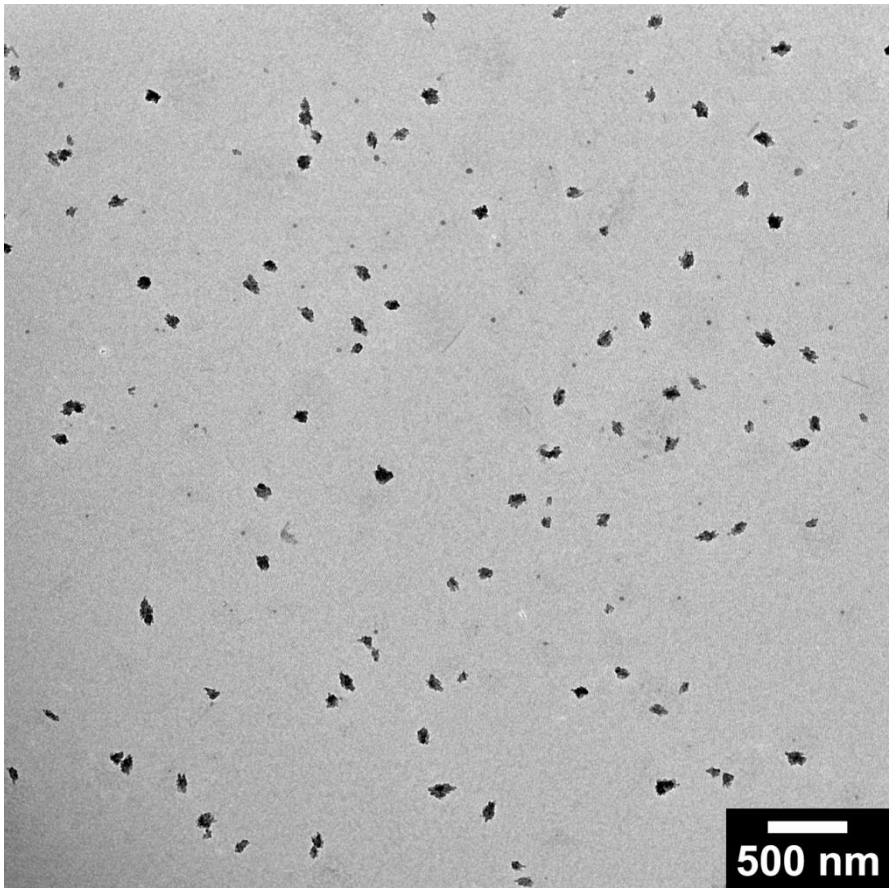

Figure 9. TEM image of GO nanosheet (diameter: *ca.* 100 nm) prepared by a ball-mill process.

combined with a positively charged amine-functionalized silica material by electrostatic interaction, resulting in formation of GO-wrapped silica materials. To ascertain that GO nanosheets were successfully deposited on the surface of silica materials, an elemental composition of the product was scrutinized by EDS (Table 1). From the elemental analysis, it was confirmed that the product consisted mainly of carbon (C), silicone (Si), and oxygen (O), indicating the existence of GO nanosheets as well as silica materials.

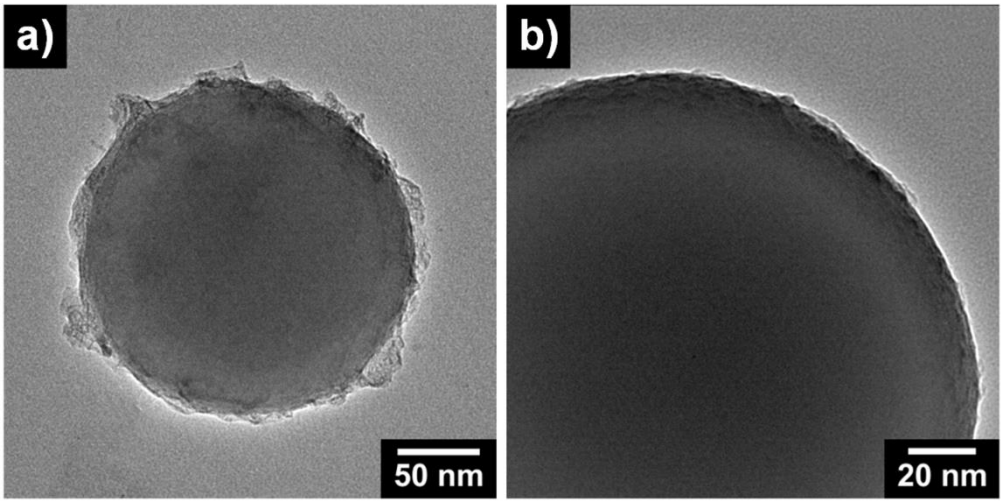

Figure 10. TEM images of a) GO-wrapped silica sphere at low magnification, and b) and at high magnification.

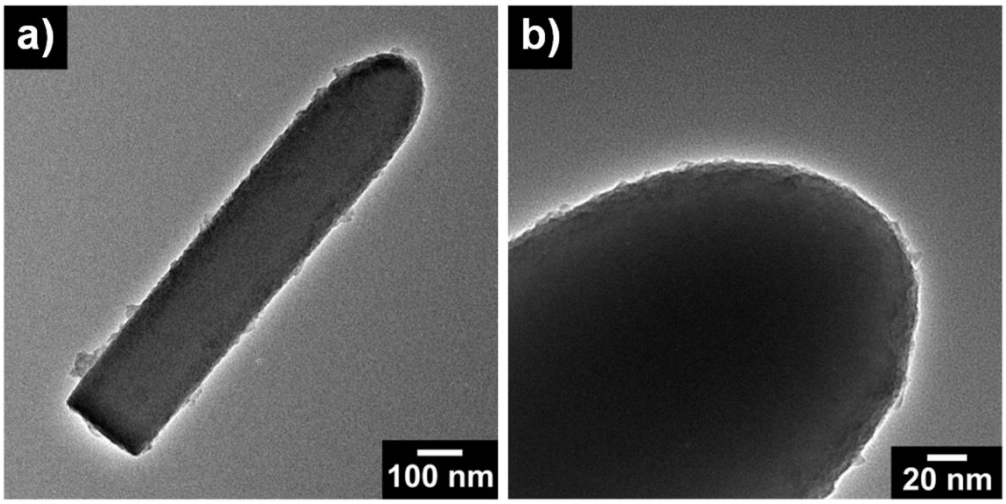

Figure 11. TEM images of a) GO-wrapped silica rod with an aspect ratio of 5 at low magnification, and b) and at high magnification.

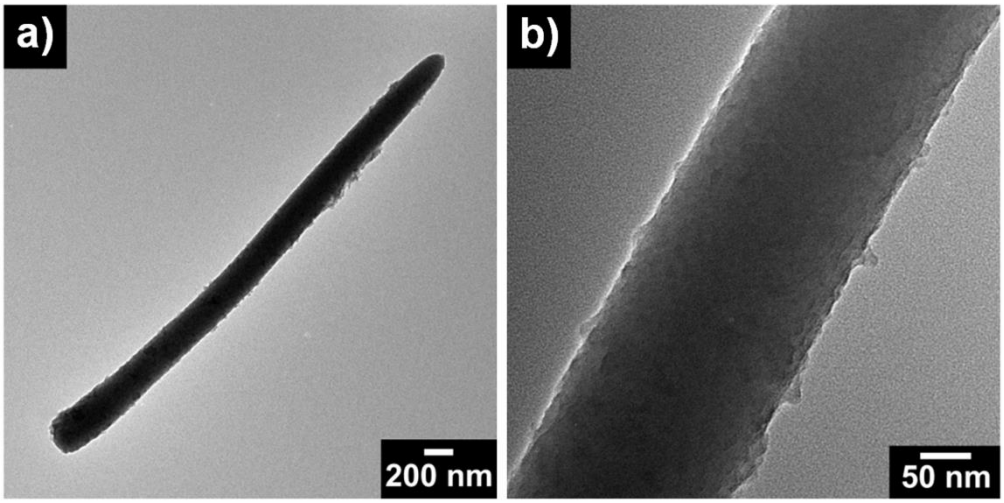

Figure 12. TEM images of a) GO-wrapped silica rod with an aspect ratio of 20 at low magnification, and b) and at high magnification.

Table 1. Physical parameters of various GO-wrapped silica materials.

Shape	Length[a]	Diameter[b]	Aspect ratio[c]	Atomic ratio[d]		
	(L)	(D)	(L/D)	C%	Si%	O%
Sphere	200 nm	200 nm	1	25.93	53.64	20.43
Rod	1 μm	200 nm	5	28.57	53.57	17.86
Rod	4 μm	200 nm	20	27.41	55.84	16.75

[a,b] The average length and diameter were confirmed by TEM (50 particles counted).

[c] Aspect ratio was determined by dividing length by diameter.

[d] The values for atomic composition were obtained in the EDS mode at a beam current of 10 μA and accelerating voltage of 10 kV.

3.1.2. Electro-response of GO-wrapped silica material-based fluids

To compare the effect of GO to electro-responsive performance, the rheology and the electro-responsive behavior of various bare silica material-based fluids were measured. In general, fluids can be classified into two categories, Newtonian and non-Newtonian fluid. The Newtonian fluid is a fluid that has a linear relation between shear rate and shear stress. In the non-Newtonian fluid, however, the relation between shear rate and shear stress is non-linear, and the non-Newtonian fluid can be classified into three categories; shear thinning, shear thickening, and Bingham fluid. A Bingham fluid is a fluid that the shear stress proportionally increases with increasing the shear rate beyond the yield stress. The various silica material-based fluids exhibited non-Newroniam behavior (typically, Bingham plastic behavior) with and without an electric field (Figure 13, 14). The shear stress value of silica material-based ER fluids was much lower than that of GO-wrapped silica material-based ER fluids under identical condition. It can also be found that the shear stress of the ER fluids increased with increasing the aspect ratio of silica materials. In addition, the shear viscosity of the silica material-based ER fluids decreased as the shear rate increased, which was in accordance with the Bingham plastic behavior. To examine the real-time response of silica materials, the change of shear stress was investigated while the electric field was alternately turned on

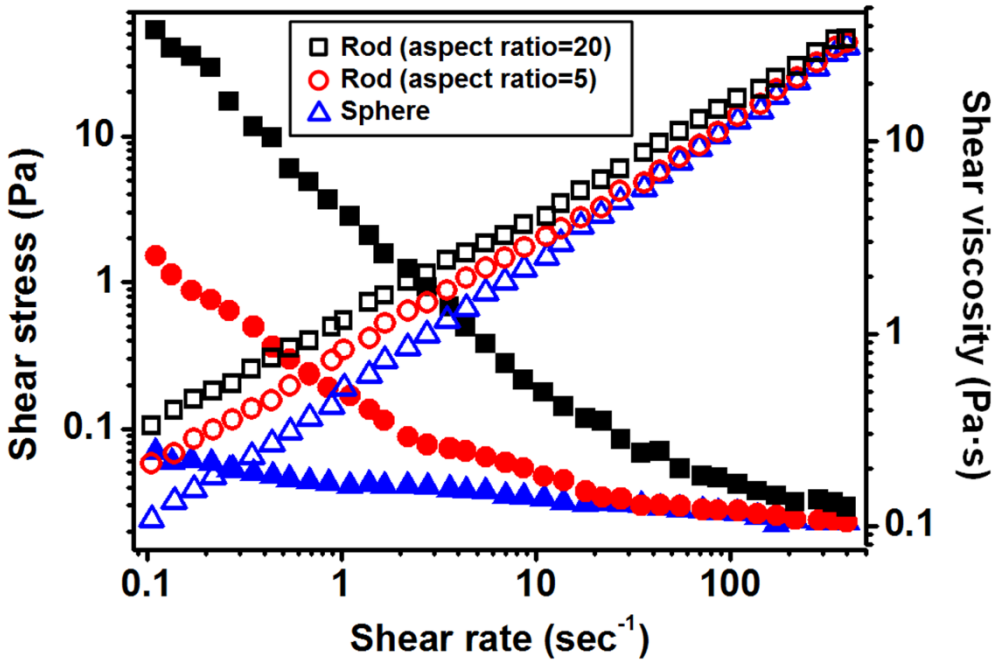

Figure 13. Shear stress (open symbol) and shear viscosity (closed symbol) of various silica materials-based ER fluids (5.0 wt% in silicone oil) without the electric field.

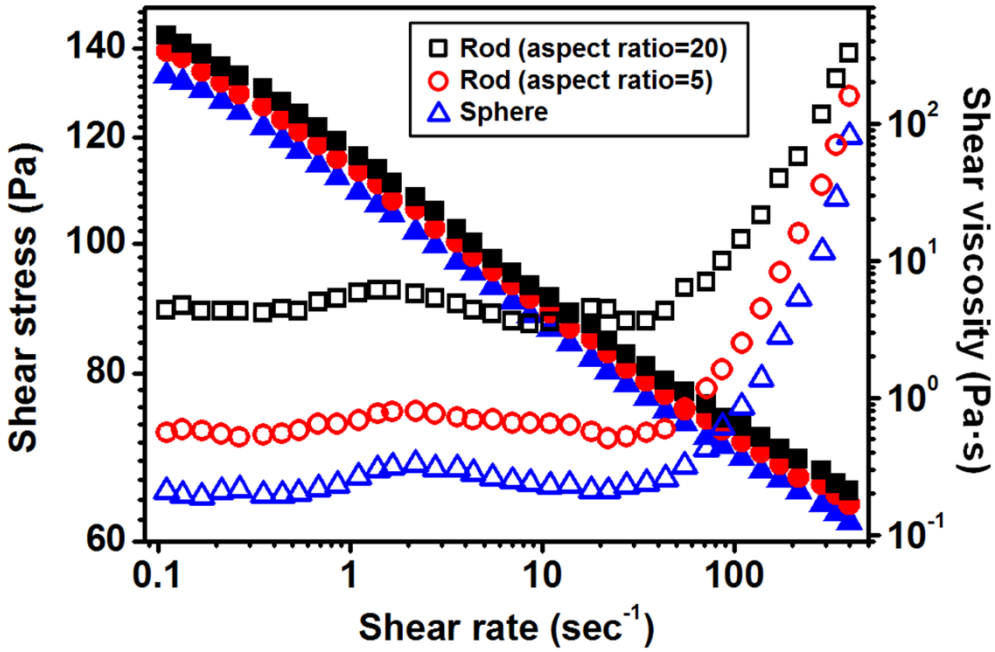

Figure 14. Shear stress (open symbol) and shear viscosity (closed symbol) of various silica materials-based ER fluids (5.0 wt% in silicone oil) under 5 kV mm^{-1} of electric field.

and off (Figure 15). The reproducibility and reversibility were confirmed by repeating the cyclical application of the electric field.

To examine the electro-responsive behavior with varying several experimental conditions and parameters, the dried GO-wrapped silica materials were dispersed in silicone oil. When an electric field was not applied, the shear stress of the GO-wrapped silica material-based fluids increased linearly in proportion to the shear rate, corresponding to the Bingham plastic behavior (Figure 16). The GO-wrapped silica material-based ER fluid exhibited higher shear stress as an aspect ratio of the material increased. The shear viscosity of the GO-wrapped silica material-based ER fluids was reduced with enhancing the shear rate under the same conditions, demonstrating Bingham plastic behavior. Slight rise in the viscosity was observed as the aspect ratio increased because of the increased flow resistance between materials. In addition, the shear stress and shear viscosity were measured as a function of the shear rate under fixed electric field strength of 5 kV mm^{-1} (Figure 17). The behavior of the GO-wrapped silica material-based ER fluids under an electric field was similar to typical Bingham plastic behavior [175, 176]. In the low shear rate range, a plateau region was observed due to the competition between induced electrostatic interaction caused by interfacial polarization of ER material and the hydrodynamic force generated by shear flow. Even though the chain-like

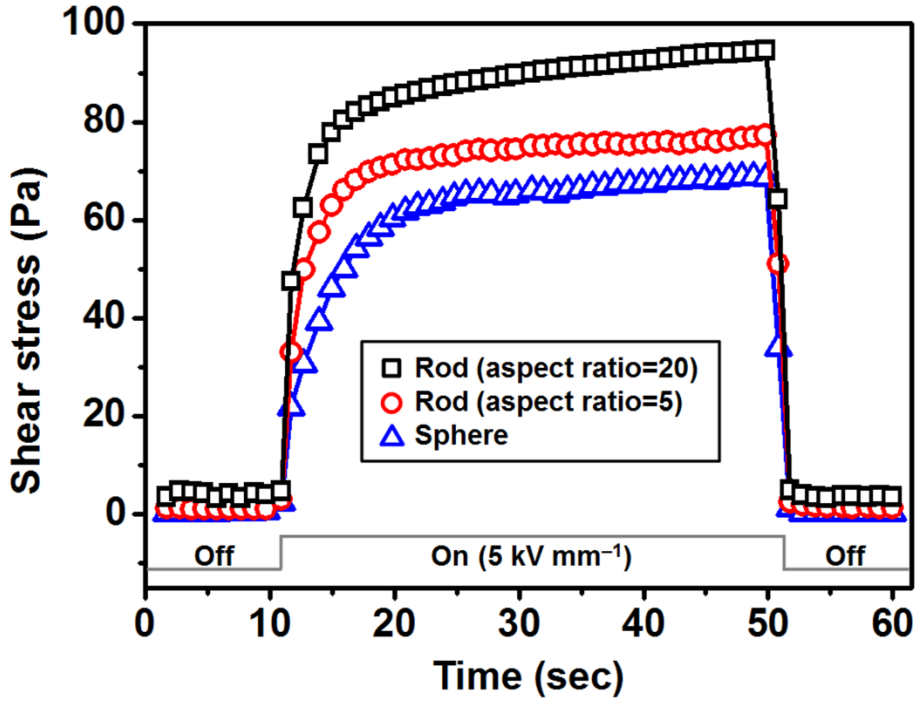

Figure 15. Effect of switching the applied electric field on the shear stress of various silica materials-based ER fluids (5.0 wt% in silicone oil).

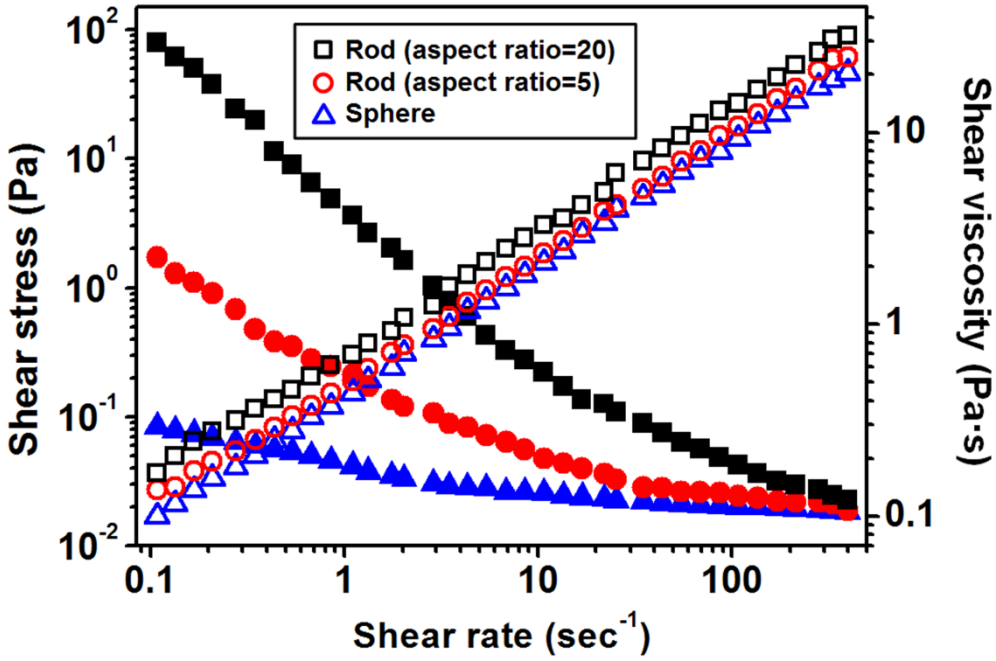

Figure 16. Shear stress (open symbol) and shear viscosity (closed symbol) of various GO-wrapped silica material-based ER fluids (5.0 wt% in silicone oil) without the electric field.

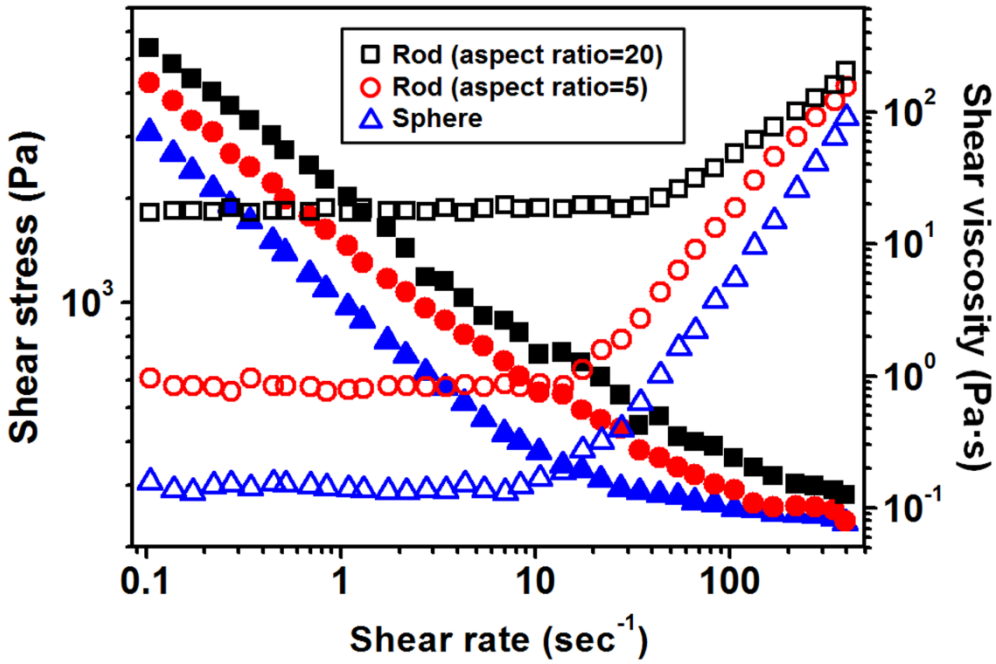

Figure 17. Shear stress (open symbol) and shear viscosity (closed symbol) of various GO-wrapped silica material-based ER fluids (5.0 wt% in silicone oil) under 5 kV mm^{-1} of electric field.

structures were broken by shear deformantion, the induced electrostatic interact ions between the electro-responsive materials initiated reformation of fibril structures. As the shear rate increased, the deformation rate was increased more rapidly than the reformation rate due to the insufficient time for reformation against rapid shear deformation, resulting in the destruction of the fibrous structure by high shear forces. Accordingly, the shear stress increased with increasing the shear rate beyond the critical shear rate, the end of the plateau region, which corresponds to the typical Newtonian fluid behavior [92, 105]. In addition, the shear viscosity of ER fluids was reduced as the shear rate increased.

The dynamic yield stress was also examined as a function of applied electric field strength at a fixed shear rate (Figure 18). In general, the dynamic yield stress is proportional to applied electric field strength at a constant shear rate. When an electric field of 1 kV mm^{-1} was applied, the yield stress of GO-wrapped silica material-bsed ER fluids was enhanced in proportion to the square of electric field strength. In case of applying high electric field (>1 kV mm^{-1}), the yield stress increased in proportion to the 1.5 power of the electric field strength. More rigid and highly-linked fibrous structures were formed because of the strong electrostatic interactions induced between ER materials as the applied electric field strength increased.

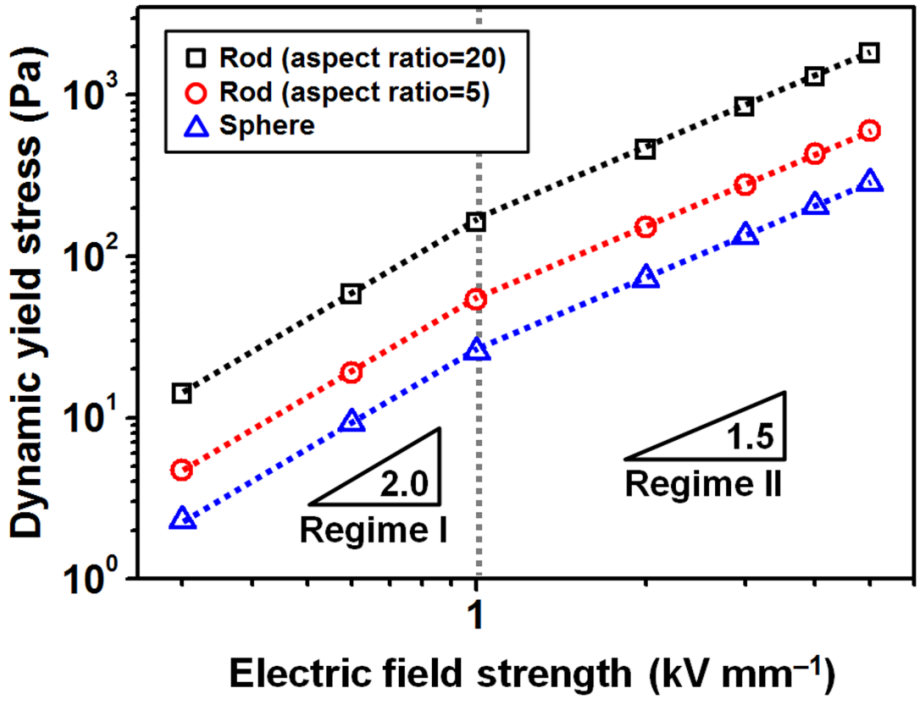

Figure 18. Dynamic yield stress of various GO-wrapped silica material-based ER fluids as a function of electric field strength (5.0 wt% in silicone oil).

To gain an in-depth insight into the real-time response of electro-responsive materials, the shear stress was measured while the electric field was alternately turned on and off (Figure 19). During cyclical switching of the electric field application, the shear stress of GO-wrapped silica material-based ER fluids increased and decreased alternately over several seconds. By repeated cyclical application application of the electric field, reproducibility and reversibility were confirmed. The GO-wrapped silica materials with a high aspect ratio represented a shorter response time (t_{res}) which was defined as a time to reach 90% of its final value. The recovery time (t_{rec}), a time required for recovery from 90% of its final value to its original level, was also shorter for the GO-wrapped silica materials with a high aspect ratio. Judging from these results, it was considered that the materials with a high aspect ratio were highly polarized along the applied electric field direction and formed highly-linked fibrillar structures.

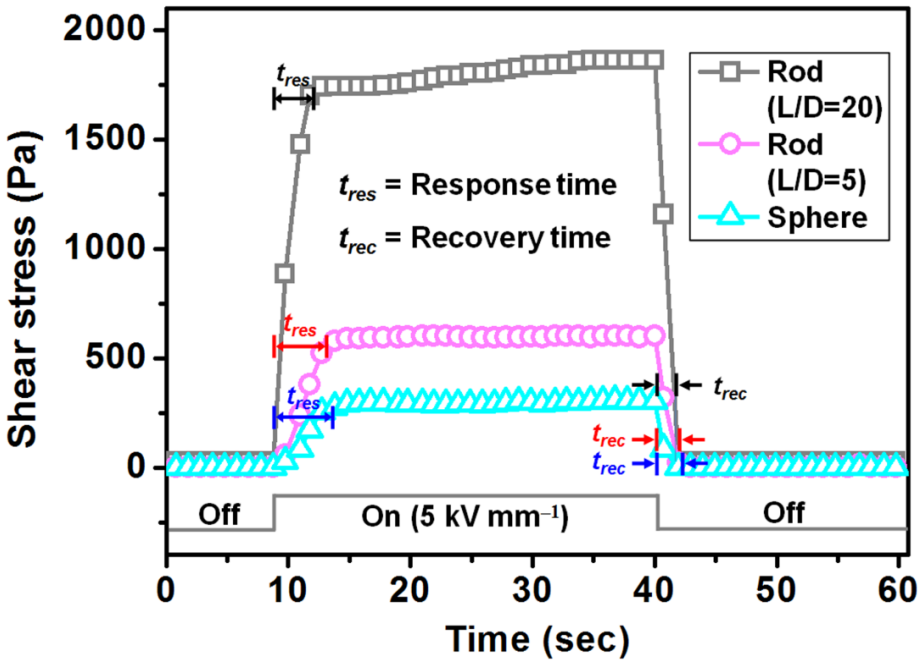

Figure 19. XPS spectra of oxidized GPCNFs with different mass ratios of $R_{K/GP}$ value.

Real-time structural change was observed using an optical microscope (Figure 20). Only a few tens of a millisecond was needed for the randomly distributed ER materials to form a chian-like structure along the applied electric field direction. The fibril-like structures were closely linked and appeared to become progressively denser over time under the electric field; this phenomenon was ascribed to the dominant electrostatic interactions between electro-responsive materials against the hydrodynamic force.

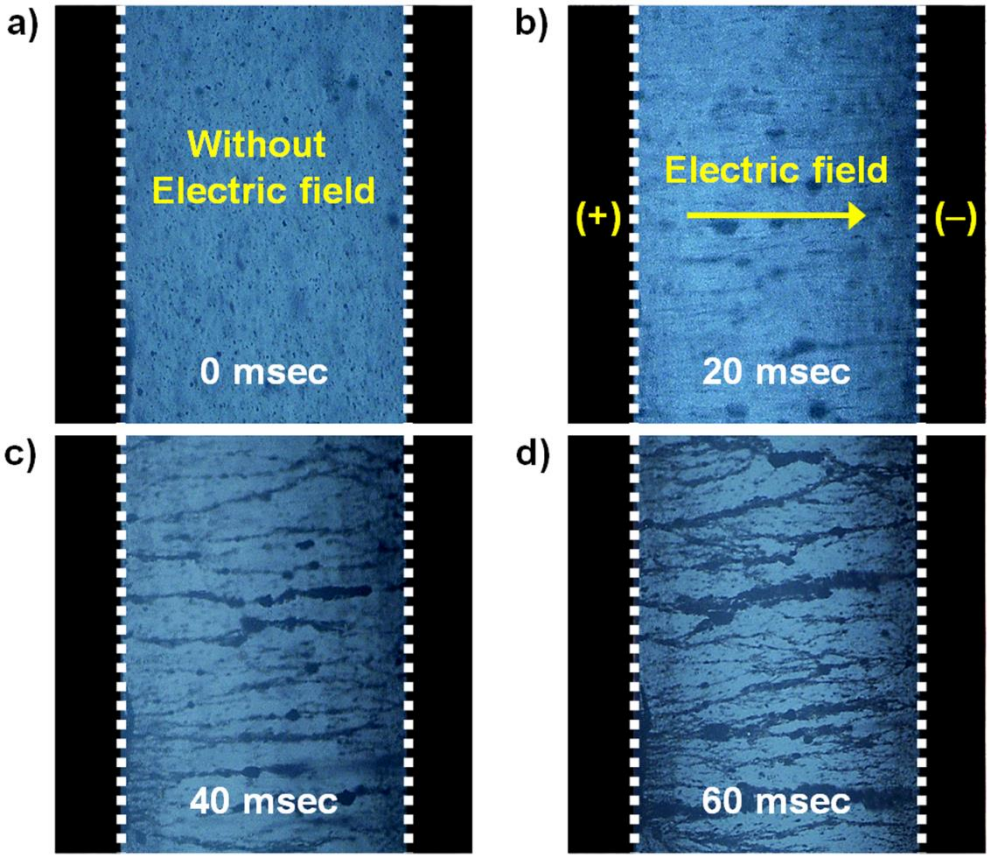

Figure 20. (a–d) Microscopy images of chain formation in silicone oil suspension of GO-wrapped silica materials (5.0 wt% in silicone oil) under an applied electric field of 5 kV mm^{-1}. The gap between two electrodes was fixed to 1.0 mm.

3.1.3. Influence of particle aspect ratio on electro-responsive behavior

The maximum shear stress of the GO-wrapped silica sphere, rod with an aspect ratio of 5, and rod with an aspect ratio of 20 were *ca*. 305, 604, and 1862 Pa respectively under identical conditions (5 wt% in silicone oil and 5 kV mm^{-1} of electric field strength). Considering the results of investigation, the ER materials with a high aspect ratio performed superior ER activities. This can be elucidated in terms of the flow resistance, mechanical stability, and dielectric properties of the fluids. Firstly, the flow resistance between the dispersed electro-responsive materials and medium oil increased as the aspect ratio of the materials increased. The relationship between the flow resistance and an aspect ratio can be determined according to the dynamic drag force (F_d):

$$F_d = \frac{1}{2}\rho C_d A v^2$$

where ρ denotes the density of fluid, C_d means the drag coefficient which is ~0.47 for a smooth sphere, A indicates the cross-sectional area, and v is the relative velocity [177, 178]. In general, the drag coefficient, C_d, varies depending on the shape of the body. For instance, the dispersed material with a high aspect ratio has a high drag coefficient, resulting in a rise in the flow resistance. Because of the increased flow resistance, the stronger steric hindrance to the shear force induced a larger shear stress. Secondly, the

relationship between ER properties and an aspect ratio of ER material also can be explained by the mechanical stability of the fibillar structure. The dispersed ER materials formed a chain-like structure along the electric field direction due to electrostatic interactions when an electric field was applied. The ER material with a high aspect ratio is better able to link together such that a stronger and more rigid fibril-like structure is generated, substantially enhancing the shear stress. Consequently, the geometrical effect caused by the high aspect ratio of the ER material contributed to the enhancement of ER effect.

In addition to the geometrical effect, the dielectric properties of the dispersed material are associated with ER behavior, because both orientational polarization (Debye polarization) and interfacial polarization (Wagner polarization) are generated in ER fluids under an electric field [148, 179]. To better comprehend the influence of dielectric properties on ER performance, the permittivity was measured as a function of an electric field frequency, as well as Cole–Cole plots for GO-wrapped silica material-based ER fluids (Figure 21, 22). The fitting lines plotted in Figure 21 were calculated based on the Havriliak–Negami equation:

$$\varepsilon^* = \varepsilon' + \mathrm{i}\varepsilon'' = \varepsilon_\infty + \frac{\Delta\varepsilon}{\{1 + (i\omega\lambda)^{1-\alpha}\}^\beta}$$

where ε' indicates the permittivity, ε'' denotes the dielectric loss factor, ε_0 describes the static permittivity ($\varepsilon_0 = \lim_{\omega\to 0} \varepsilon^*(\omega)$), ε_∞ denotes the fictitious

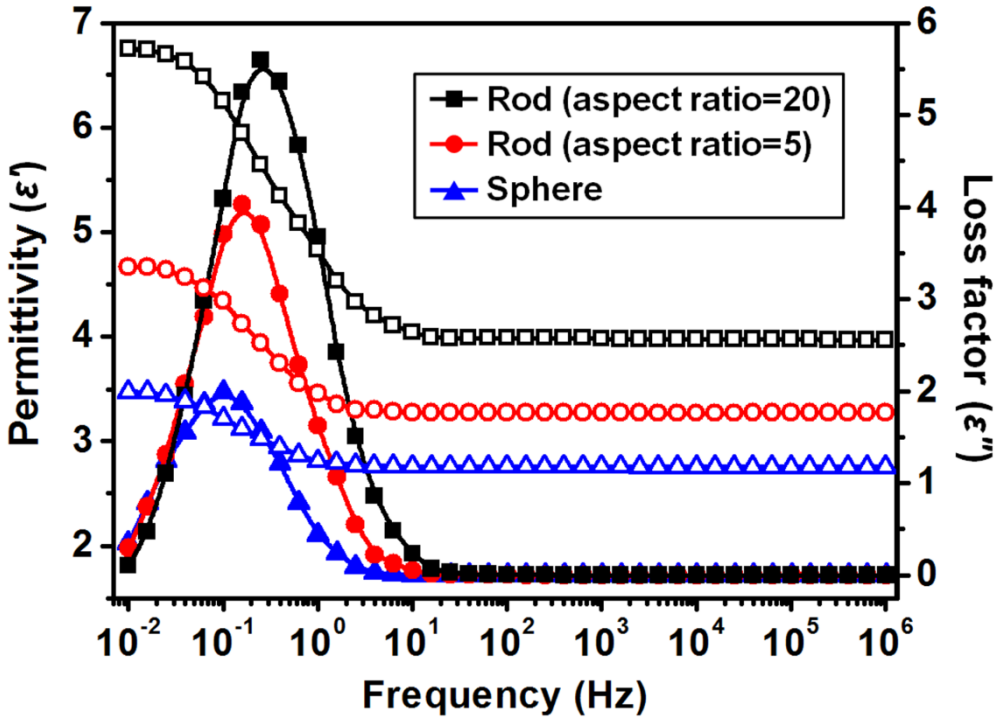

Figure 21. Permittivity (ε') and loss factor (ε'') as a function of frequency for various GO-wrapped silica material-based ER fluids (5.0 wt%). Open and closed symbols indicate permittivity and loss factor, respectively.

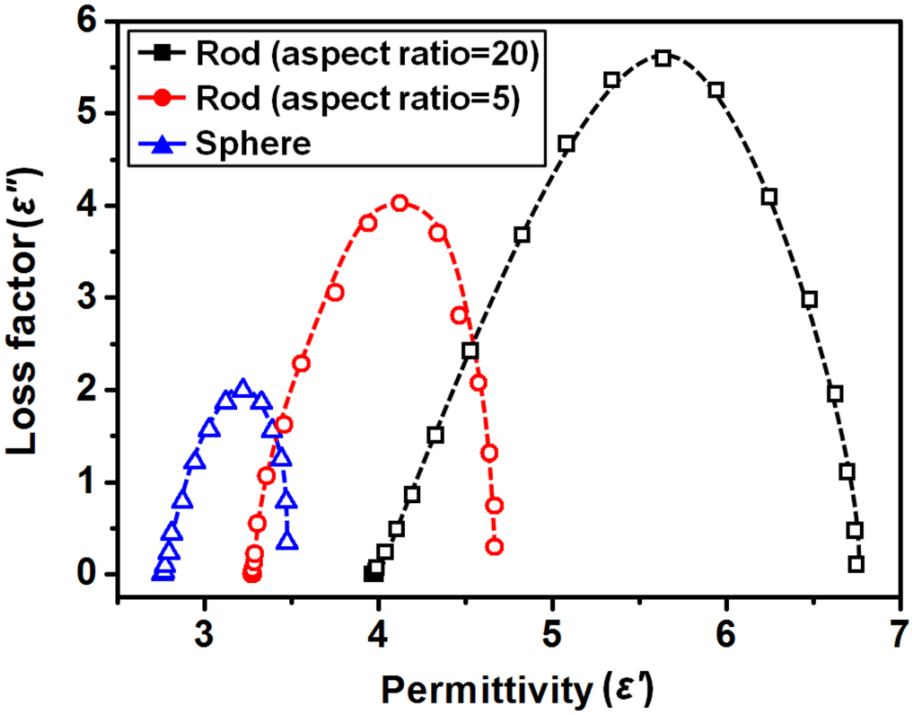

Figure 22. Cole–Cole plots for various GO-wrapped silica material-based ER fluids.

permittivity defined as the permittivity at the high frequency limit ($\varepsilon_\infty = \lim_{\omega\to\infty} \varepsilon^*(\omega)$), $\Delta\varepsilon$ is the polarizability ($\Delta\varepsilon = \varepsilon_0 - \varepsilon_\infty$), ω is the angular frequency, and λ is the characteristic relaxation time of the medium [180]. The exponents α and β depicts the asymmetry and broadness of the corresponding spectra, respectively. Cole–Cole relaxation corresponds to a particular case of the Havriliak–Negami relaxation when the relaxation peaks are symmetric. In the case of Cole–Cole relaxation, the exponent parameter α is a value between 0 and 1 ($0 \leq \alpha < 1$), and β is equal to 1 ($\beta = 1$). The Cole–Cole equation is proposed as follows:

$$\varepsilon^* = \varepsilon_\infty + \frac{\Delta\varepsilon}{1 + (i\omega\lambda)^{1-\alpha}}, \qquad (0 \leq \alpha < 1)$$

where $\Delta\varepsilon$ is related to the electrostatic interaction between the dispersed materials [181]. The value of $\Delta\varepsilon$ for GO-wrapped silica sphere, rod with an aspect ratio of 5, and rod with an aspect ratio of 20 was 0.71, 1.40, and 2.78 respectively (Table 2). Accordingly, the higher the aspect ratio of ER materials was, the stronger the electrostatic interaction between ER materials was. The dielectric relaxation time (λ) is associated with the interfacial polarization and is determined by f_{max}, the frequency corresponding to the maximum value of ε'' or the steepest slope for the permittivity as a function of frequency. The relaxation time can be estimated using the following equation: [127]

$$\lambda = \frac{1}{2\pi f_{max}}$$

Table 2. Dielectric parameters for various GO-wrapped silica materials-based ER fluids.[a]

Sample	ε_0	ε_∞	$\Delta\varepsilon = \varepsilon_0 - \varepsilon_\infty$	f_{max}[b]	λ[c]
Spheres	3.47	2.76	0.71	0.1 Hz	1.592 s
Rods (aspect ratio = 5)	4.67	3.27	1.40	0.158 Hz	1.007 s
Rod (aspect ratio = 20)	6.75	3.97	2.78	0.251 Hz	0.634 s

[a] Dielectric parameters were evaluated by a Solartron SI 1260 Impedence/gain-phase analyzer with a Solartron 1296 dielectric interface.

[b] The local frequency of the peak on the dielectric loss factor ε'' and the f_{max} values were acquired by nonlinear regression analysis using OriginPro.

[c] The relaxation time, denoted by $\lambda=1/(2\pi f_{max})$ (f_{max} is the frequency of the loss peak).

The relaxation time for GO-wrapped silica sphere, rod with an aspect ratio of 5, and rod with an aspect ratio of 20 was 1.592, 1.007, and 0.634 s respectively. Since the relaxation time is associated with the interfacial polarization response, it can be concluded that the polarization rate of GO-wrapped silica rod with higher aspect ratio is faster than that of other two ER materials under an electric field.

To achieve more insight into the relationship between dielectric properties and ER behavior, the effect of particle geometry on the dielectric properties was evaluated on the basis of the electrostatic polarization model. According to the theory provided by Stratton, the material with a higher aspect ratio should have a larger dielectric constant, because polarization increases with increasing aspect ratio. For this reason, the electro-responsive material having a high aspect ratio displayed better ER performance than the spherical-shaped particle under the same conditions. The larger induced dipole moment resulted in strong polarization for the material with a higher aspect ratio. The magnitude of the dipole moment for spherical-shaped particle can be defined according to the equation given by Stratton:[182, 183]

$$p = 4\pi\epsilon_0\epsilon_c a^3\beta E, \qquad \beta = \frac{\epsilon_p - \epsilon_c}{\epsilon_p + 2\epsilon_c}$$

where p denotes the dipole moment, ϵ_0 is the permittivity in vacuum (8.854×10^{-12} F m^{-1}), ϵ_c is the permittivity of the dispersing medium, ϵ_p is the

permittivity of the particle, a indicates the radius of the sphere, β describes the particle's relative polarizability, and E is the electric field intensity. For an ellipsoid-shaped particle oriented along the direction of the electric field, the dipole moment can be decided using the equations given by Dukhin:[184]

$$p = V\epsilon_0\epsilon_c \frac{\epsilon_p - \epsilon_c}{\epsilon_c + (\epsilon_p - \epsilon_c)A_z} E, \quad A_z = (\xi^2 - 1)[\frac{\xi}{2}\ln\left(\frac{\xi+1}{\xi-1}\right) - 1]$$

where V is the volume of the ellipsoid-shaped particle ($V = \frac{4}{3}\pi a^3 \frac{L}{a}$), A_z denotes the depolarization factor verified by Stratton and Lam, a is the radius of the minor axis of an ellipsoid-shaped particle, L is the radius of the major axis of an ellipsoid-shaped particle, and ξ denotes a geometric parameter calculated as follows:

$$\xi = \frac{L}{\sqrt{L^2 - a^2}}$$

From these equations related to the magnitude of the dipole moment for electro-responsive materials, a stronger polarization is generated as an aspect ratio of the ER particle increases, because of a larger induced dipole moment. Consequently, the ER fluid composed of GO-wrapped silica rod with a higher aspect exhibited the largest dielectric constant and the shortest relaxation time due to the strong polarization created by the large dipole moment, which in turn, resulted in a considerably higher shear stress under the electric field.

3.2. Electro-Responsive Performance Depending on Particle Shell Structure

3.2.1. Fabrication of size-controlled double-shell SiO_2/TiO_2 hollow nanoparticles

Double-shell-structured SiO_2/TiO_2 hollow nanoparticles were successfully fabricated *via* the procedures illustrated in Figure 23. First, silica nanoparticles, which act as core template, were synthesized by the Stöber method. The TiO_2 shell was formed on the silica core template by the sol–gel method using TTIP as precursor. To enhance affinity between the TiO_2 shell and SiO_2 precursor, PVP was adsorbed on the ST CS NPs. Hydroxyl groups in oxide surfaces interact with negatively charged carbonyl groups of PVP, leading to affinity enhancement. Subsequently, TEOS was added dropwise to the reacting solution in order to coat SiO_2 layer on the ST CS NPs, resulting in formation of $SiO_2/TiO_2/SiO_2$ core/shell nanoparticles (STS CS NPs). By adding TTIP to the solution of STS CS NPs, STST CS NPs were synthesized *via* the sol–gel reaction. Finally, STST CS NPs were etched using sonication with NH_4OH to obtain DS HNPs.

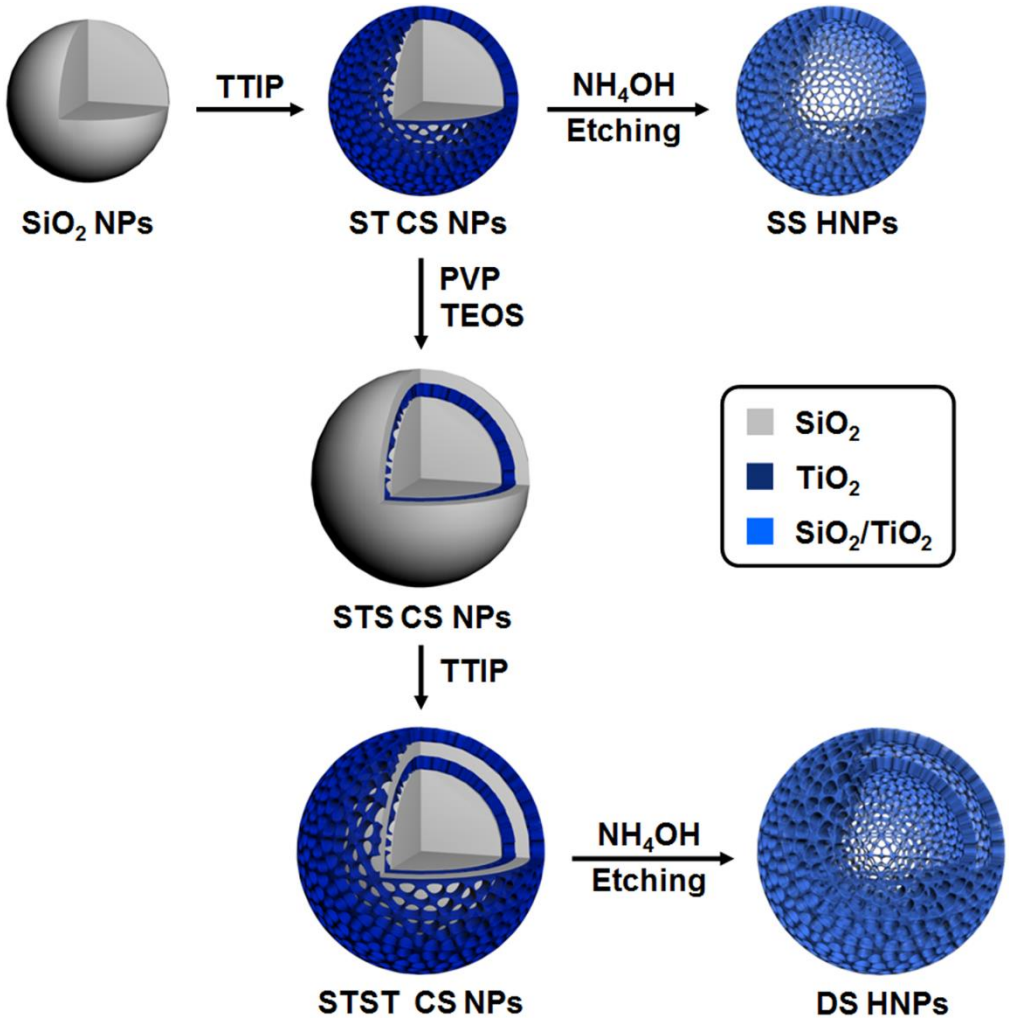

Figure 23. Schematic illustration of the formation procedure of DS HNPs with a highly porous structure *via* PVP adsorption on the TiO_2, sol–gel reaction, and etching process.

Uniform single shell SiO_2/TiO_2 hollow nanoparticles (SS HNPs) and DS HNPs having an average diameter of 240 nm were successfully fabricated (Figure 24). The SS HNPs were synthesized *via* the procedures similar to the method for fabricating DS HNPs, except that ST CS NPs were etched instead of STST CS NPs. For the preparation of SS HNPs, silica particles with an average diameter of 150 nm were used as a core template. The shell thickness of SS HNP was confirmed as *ca*. 57 nm (Figure 24a). The DS HNP with same diameter has the inner and outer shell thicknesses of *ca*. 27 and 34 nm respectively (Figure 24b). The shell thickness of SS HNPs and DS HNPs can be controlled by adjusting the amount of TTIP and TEOS during the course of the fabrication.

The size of DS HNPs was controlled by 120, 150, 180, and 240 nm by adopting different-sized silica particles as core templates (Figure 25). The diameter of silica core templates utilized for the synthesis of 120, 150, 180, and 240 nm-sized DS HNPs was 40, 60, 80, and 120 nm, respectively. It was confirmed that both inner and outer shell thicknesses of DS HNPs increased as the size of DS HNPs increased (Table 3). As mentioned above, shell thicknesses of DS HNPs can be adjusted by adding different amounts of TTIP and TEOS. However, an excess amount of TTIP and TEOS brings about an adherence of inner and outer shells, forming of a thick single shell.

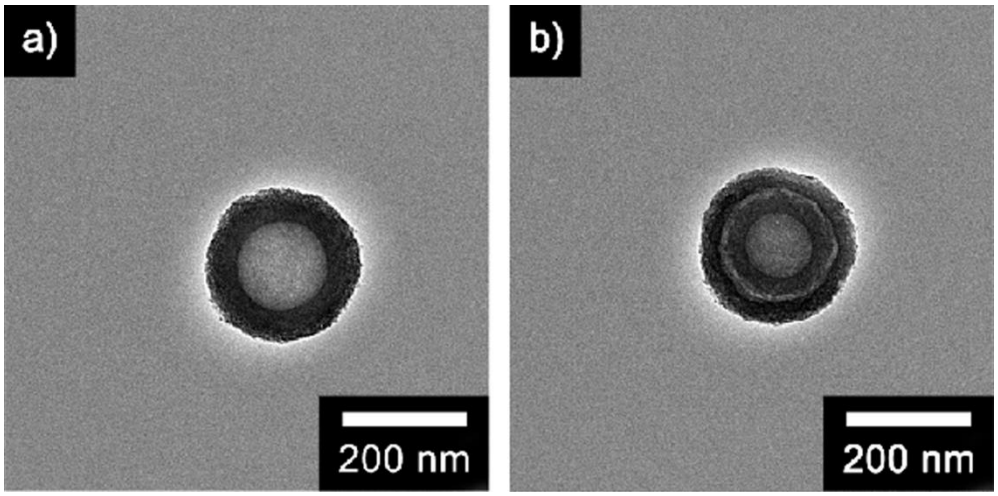

Figure 24. TEM images of a) SS HNP and b) DS HNP with a diameter of 240 nm.

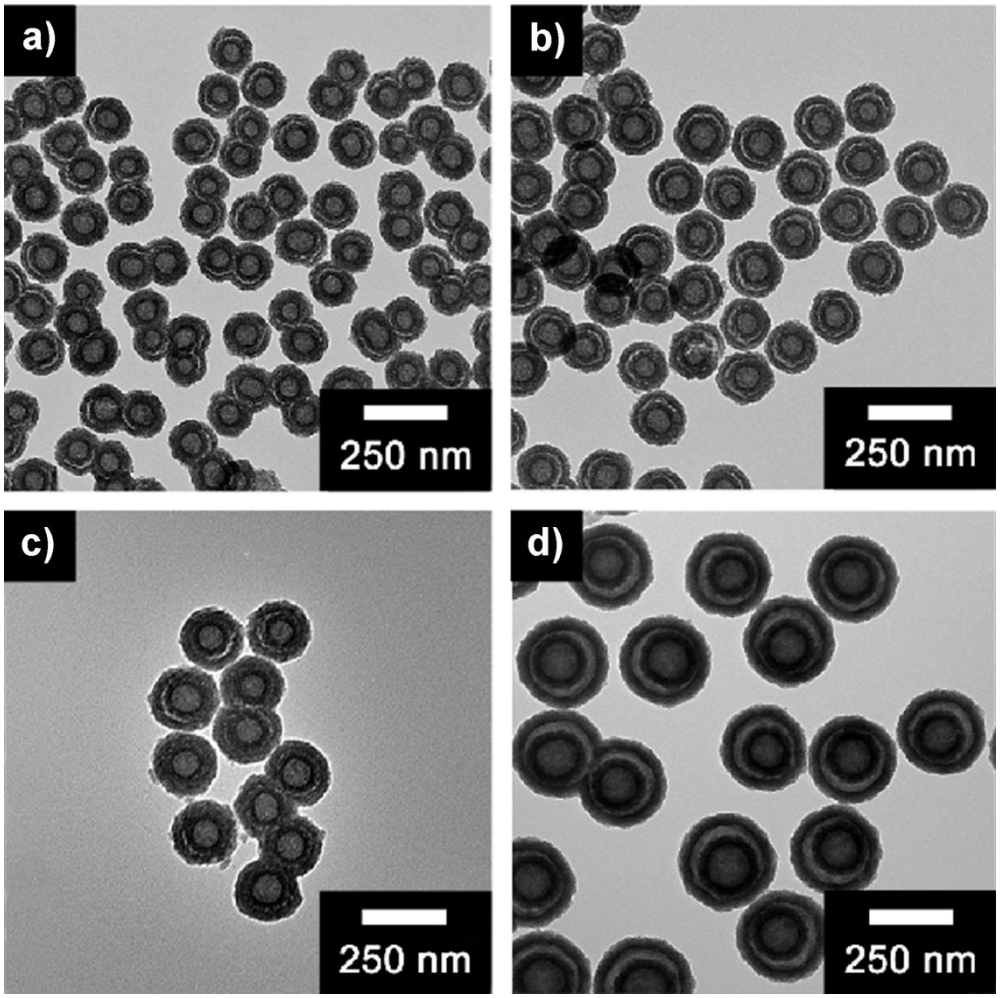

Figure 25. TEM images of DS HNPs with a diameter of a) 120, b) 150, c) 180, and d) 240 nm.

Table 3. Inner and outer shell thicknesses of four different-sized DS HNPs.

Samples	Inner shell thickness[a]	Outer shell thickness[b]
	[nm]	[nm]
120 nm DS HNPs	10.8 ± 5	13.5 ± 5
150 nm DS HNPs	13.5 ± 5	16.9 ± 5
180 nm DS HNPs	19.9 ± 5	24.9 ± 5
240 nm DS HNPs	27.1 ± 5	33.9 ± 5

[a,b] The average thicknesses were confirmed by TEM (50 particles counted).

The elemental composition of the SS HNP and four different-sized (120, 150, 180, and 240 nm) DS HNPs were investigated using elemental analyzer (EA) and inductively coupled plasma-atomic emission spectrometer (ICP-AES). Judging from the results of elemental analysis, the SS HNPs and the four different-sized DS HNPs contain a small amount of organic materials. It is estimated that these organic materials are residues of PVP and NH_4OH which were used for the formation of SiO_2 shell and etching process, respectively. However, it is considered that the residual organic materials did not affect the ER performance because the amount of organic residues was very small. In addition, the difference of ER performance was not attributed to the residual organic materials since the contents of C, H, and N were similar in the SS HNPs and the four different-sized DS HNPs. From the elemental analysis using ICP-AES, the contents of each element including Si and Ti were abtained as described in Table 4. Moreover, the elemental mapping images were acquired by STEM-EDS to visualize the elemental distribution of the SS HNP and the DS HNPs (Figure 26).

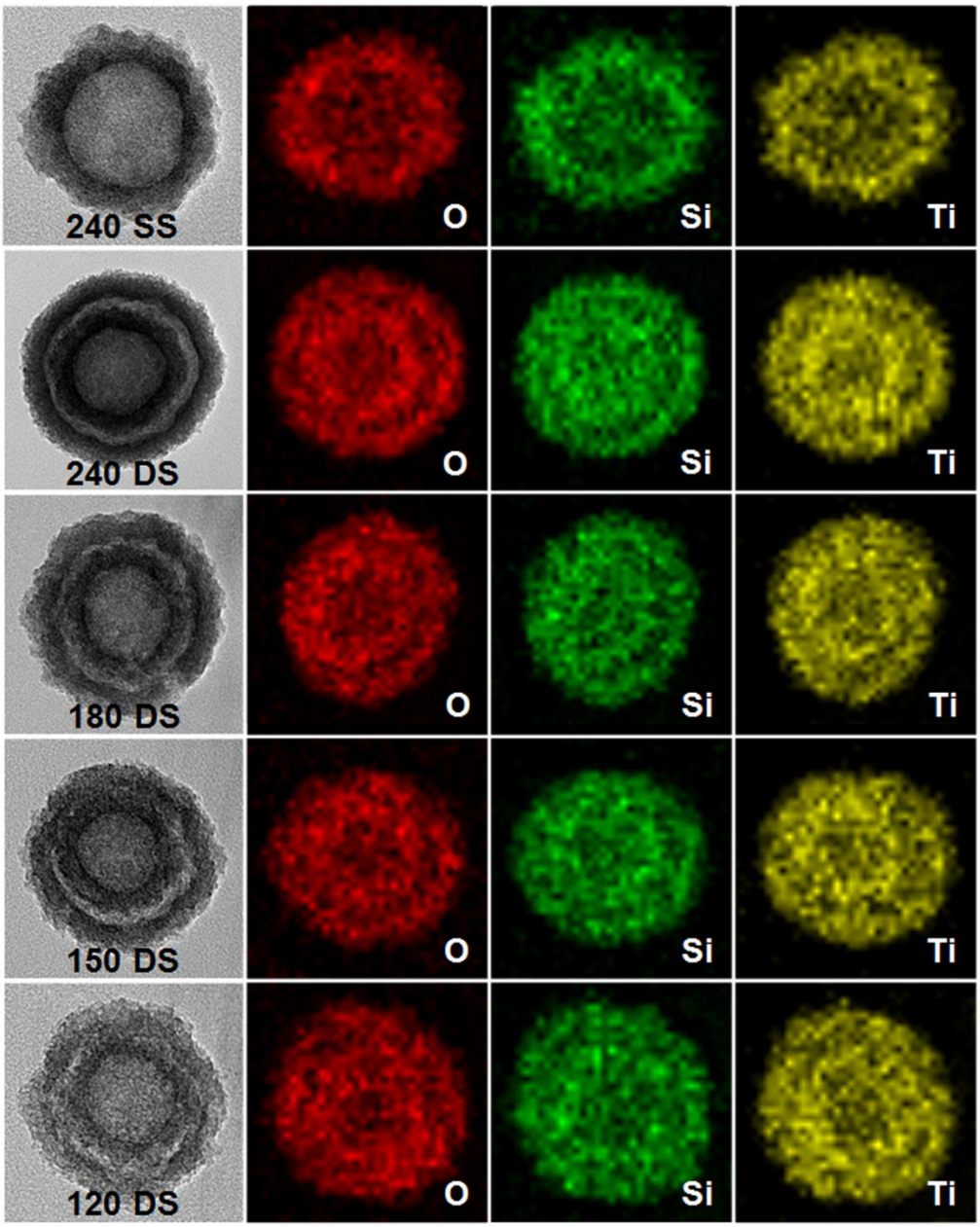

Figure 26. STEM-elemental-mapping images of 240 nm-sized SS HNP and four different-sized (240, 180, 150 and 120 nm) DS HNPs.

Table 4. Elemental analysis of the 240 nm-sized SS HNPs and the four different-sized (120, 150, 180 and 240 nm) DS HNPs.

Samples	Diameter [nm]	Elemental ratio (wt%)[a]						
		C	H	N	S	Si	Ti	O
SS HNPs[b]	240	3.0	2.0	2.9	0.0	5.7	47.9	38.5
DS HNPs[c]	120	3.8	2.1	2.7	0.0	9.3	42.9	39.2
	150	2.6	2.1	2.7	0.0	9.2	43.7	39.7
	180	3.1	2.1	2.6	0.0	10.7	41.6	39.9
	240	3.7	2.1	2.5	0.0	9.3	43.1	39.3

[a] The values for C, H, S and S were acquired by elemental analyzer (EA1110, CE Instrument). The values for Si and Ti were obtained by inductively coupled plasma-atomic emission spectrometer (ICPS-7500, SHIMADZU Corporation, Japan).

[b] SS HNPs : single shell SiO_2/TiO_2 hollow nanoparticles

[c] DS HNPs : double shell SiO_2/TiO_2 hollow nanoparticles

3.2.2. Influence of the number of SiO_2/TiO_2 shell on electro-responsive property

To examine the relationship between the number of shells and electro-responsive properties, the SS HNP-based ER fluid and the DS HNP-based ER fluid were prepared by dispersing the dried particles in silicone oil, a dispersing media. Both shear stress and viscosity were measured as a function of the shear rate under an electric field of 3 kV mm^{-1} (Figure 27). When an electric field of kV mm^{-1} was applied, the leakage current of the SS HNPs and the DS HNPs was 0.010 and 0.012 mA, respectively. In the case of 240 nm-sized DS HNPs-based ER fluid, the plateau region was observed at the low shear rate region because of the competition between induced electrostatic interaction of electro-responsive particles and hydrodynamic force generated by shear flow, corresponding to typical Bingham plastic behavior [45, 181, 185]. At the end of plateau region, critical shear rate, the shear stress increased gradually, which represents typical Newtonian fluid behavior [100, 186]. Meanwhile, in the case of SS HNPs-based ER fluid, the shear stress decreased as the shear rate increased approaching to a minimum shear stress at a critical shear rate. To cover this shear stress decrease phenomenon at the low shear rate region, a modified theology equation called the Cho–Choi–Jhon (CCJ) model was suggested as follows:

$$\tau = \frac{\tau_y}{1 + (t_1\dot{\gamma})^{\alpha}} + \eta_{\infty}\left(1 + \frac{1}{(t_2\dot{\gamma})^{\beta}}\right)\dot{\gamma}$$

where τ indicates the shear stress, τ_y means the dynamic yield stress, $\dot{\gamma}$ is the shear rate, t_1 and t_2 are time constants, η_{∞} denotes the viscosity at infinite shear rate, and the exponent α is related to the decrease of shear stress at a low shear rate region, whereas β is for the high shear rate region ($0 < \beta \leq 1$) [187, 188]. Due to the relatively weak electrostatic interactions between the electro-responsive particles, the reduction of shear stress occurred for the SS HNPs-based ER fluid, which is analogous with the CCJ model. Furthermore, the shear viscosity of ER fluids decreased with increasing the shear rate. Judging from the value of yield stress, it was revealed that the DS HNP-based ER fluid exhibited approximately 4.1 times higher yield stress than the SS HNP-based ER fluid.

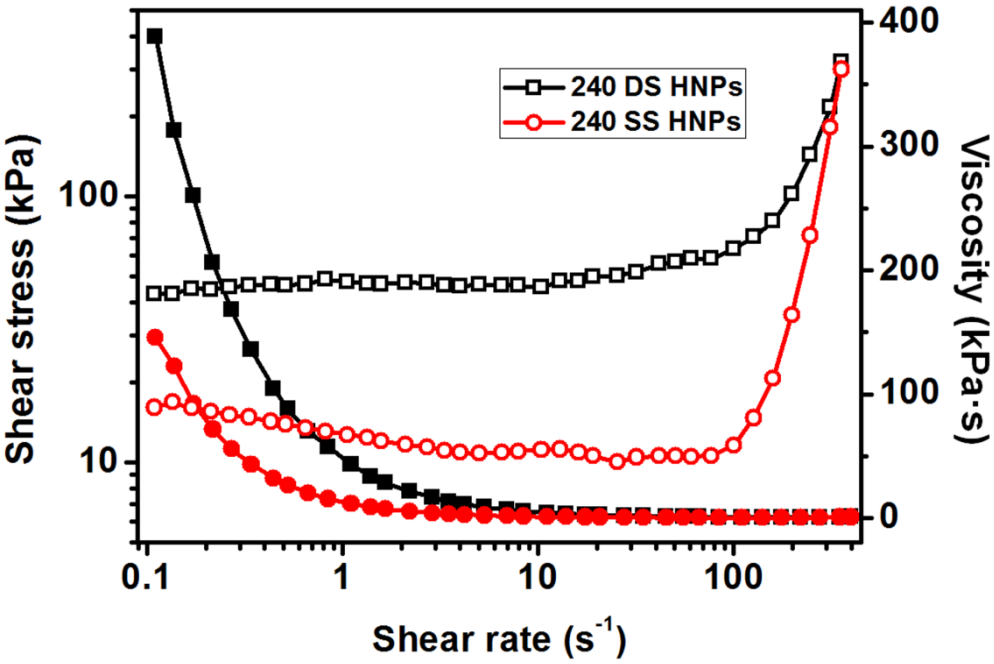

Figure 27. Shear stress (open symbol) and viscosity (closed symbol) of 240 nm-sized single shell SiO_2/TiO_2 hollow nanoparticles (240 SS HNPs)-based ER fluid and 240 nm-sized double-shell SiO_2/TiO_2 hollow nanoparticles (240 DS HNPs)-based ER fluid (10 wt% in silicone oil) under 3 $kVmm^{-1}$ of electric field.

To identify the reproducibility of ER fluids, the shear stress was measured during the electric field on and off (Figure 28). The reproducibility can be proved by the response time and recovery time, which is defined as the time required for reaching 90% of its final value. It was confirmed that the DS HNP-based ER fluid exhibited faster response and recovery time than the SS HNP-based ER fluid.

The schematic illustration for elucidation on the influence of the number of SiO_2/TiO_2 shell was provided in Figure 29. When an external electric field was applied in the fluid, the polarization was generated on the electro-responsive particles along the electric field direction. Due to the generated polarization, the particles formed fibril-liker structures along the electric field direction by the induced electrostatic interaction between the dispersed electro-responsive particles. In the case of the DS HNP-based ER fluid, additional electrostatic interactions were formed between the two shells in the particle, leading to stronger shear stress. High surface area of DS HNPs achieved by increasing the number of shells produced the interfacial polarizability under an electric field, resulting in the enhancement of ER effect. In other words, more surface sites for charge accumulation were produced because of the high surface area additionally formed by the inner cavity of DS HNPs, which accounted for strong particle polarization [189]. Consequently, the DS HNPs-based ER fluid

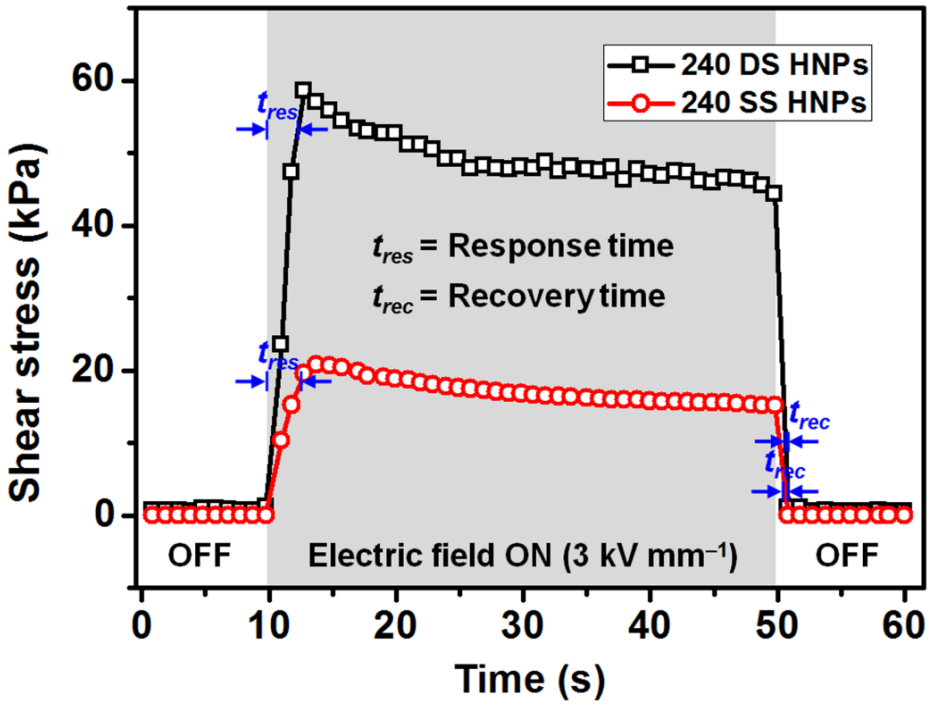

Figure 28. Effect of switching the electric field on shear stress. The shear rate was 0.1 s^{-1}.

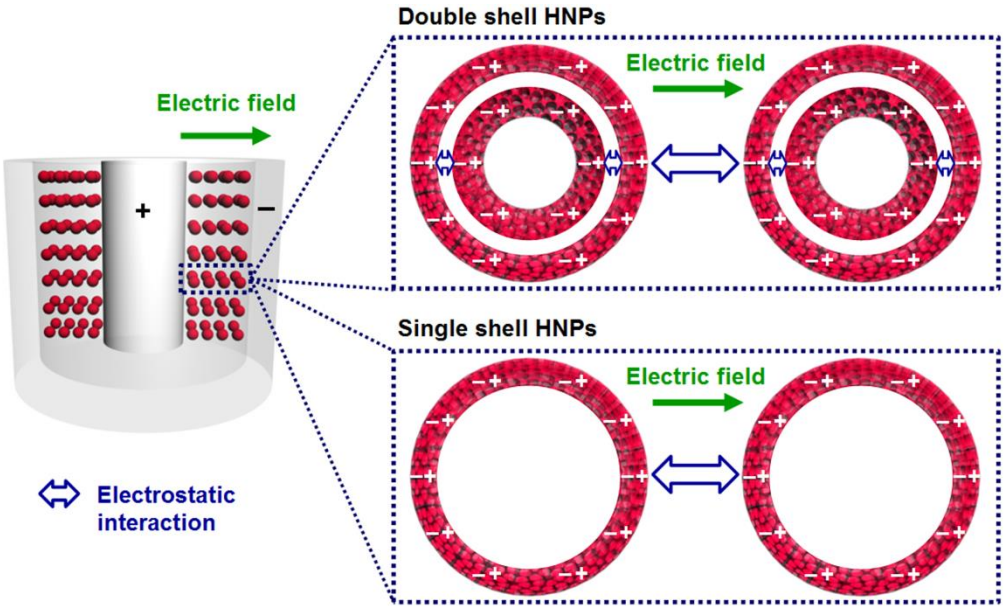

Figure 29. Schematic illustration for the polarization behavior of DS HNPs and SS HNPs under an applied electric field.

represented higher ER performance than the SS HNPs-based ER fluid.

The structural change depending on the electric field on and off was observed by optical microscope (Figure 30). When an electric field was switched on, the randomly dispersed electro-responsive particles formed fibrillar structures within a few tens of milliseconds.

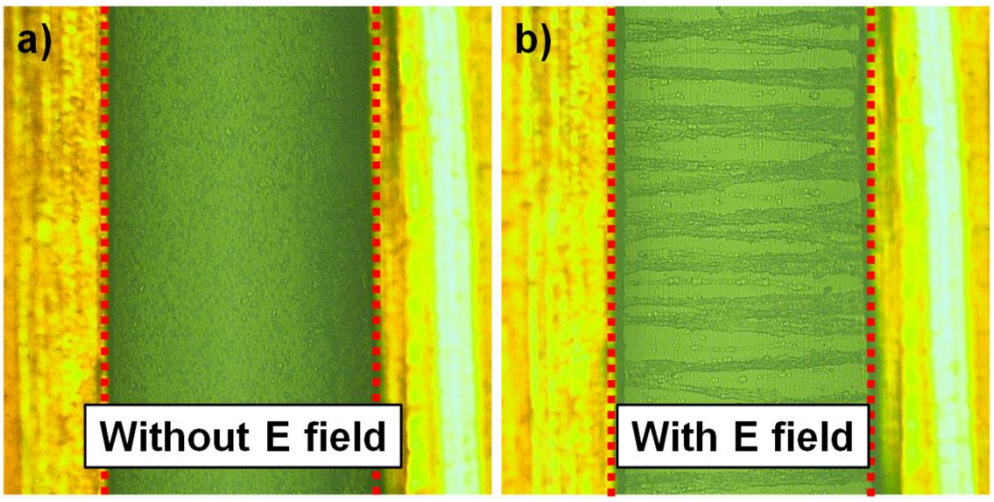

Figure 30. Optical microscopy images of DS HNPs-based ER fluid (a) without an electric field and (b) under an electric field. The gap distance between two electrodes was adjusted to 1 mm.

3.2.3. Electro-responsive activity of double-shell SiO_2/TiO_2 hollow nanoparticles depending on particle size

To achieve an in-depth insight into the size effect of electro-responsive materials, four different-sized (120, 150, 180, and 240 nm) DS HNP-based ER fluids were prepared for analysis of ER properties. Both shear stress and viscosity depending on the shear rate were measured under the electric field strength of 3 kV mm^{-1}. The leakage current of the 120, 150, 180 and 240 nm-sized DS HNPs-based ER fluids were 0.036, 0.028, 0.022, and 0.012 mA, respectively, under the electric field strength of 3 kV mm^{-1}. As demonstrated in Figure 31, all ER fluids except 120 nm-sized DS HNPs-based ER fluid presented the typical Bingham plastic behavior below the critical shear rate and the typical Newtonian fluid behavior beyond the critical shear rate. In the case of the 120 nm-sized DS HNPs-based ER fluid, the shear stress slightly decreased with increasing the shear rate at low shear rate region, corresponding to the CCJ model. Because the 120 nm-sized DS HNPs had relatively low density compared with other DS HNPs, it was more difficult for the 120 nm-sized DS HNPs to sustain their chain-like structure against the hydrodynamic force.

Particularly, the yield stress was enhanced as the diameter of particle decreased, which was attributed to the high mobility and high external surface

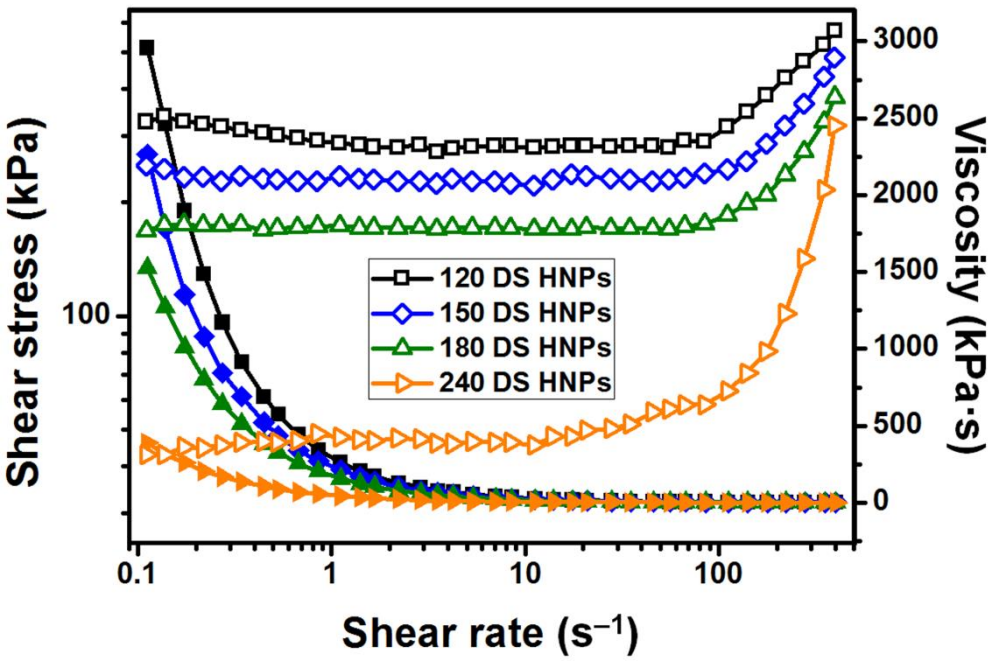

Figure 31. Shear stress (open symbol) and viscosity (closed symbol) of four different-sized (120, 150, 180, 240 nm) DS HNPsbased ER fluid (10 wt% in silicone oil) under 3 $kVmm^{-1}$ of electric field.

area of a small-sized particle. The 120 nm-sized DS HNPs-based ER fluid exhibited approximately 7.6 times higher yield stress than 240 nm-sized DS HNPs-based ER fluid. In particular, the yield stress of 120, 150, and 180 nm-sized DS HNPs-based ER fluids were beyond 130 kPa, which corresponded to the giant electrorheological (GER) fluids. The GER fluids are set apart from the conventional ER fluids since the yield stress of GER fluids exceeds the theoretical upper bound [190]. One of the most popular theories for describing the mechanism of ER fluid under an electric field is the polarization model (conventional ER fluid mechanism) [191]. In the polarization model, yield stress is attributed to the formation of a fibril-like structure by the electrostatic interactions between the particles and the Maxwell–Wagner interfacial polarization. The induced electrostatic force is dependent on the dielectric constant mismatch between the solid particles and liquid medium. The relationship between the yield stress (τ_y) and applied electric field strength (E_0) can be explained by using the following point-dipole approximation:

$$\tau_y \propto \varphi K_f E_0^2 f(\beta)$$

where φ is the particle volume fraction, β denotes the dimensionless dielectric mismatch parameter ($\beta = (K_p - K_f)/(K_p + 2K_f)$). Here, K_p and K_f indicate the dielectric permittivity of particles and fluid, respectively [192]. However, in some systems especially under high electric field strength, the

rheological behavior of fluid does not follow the polarization model. The conduction model demonstrates particle interactions after formation of fibrillar structures, irrespective of the microstructural changes when an electric field is turned on. In the conduction model, the yield stress is proportional to the applied electric field strength to the power of 1.5 ($\tau_y \propto E_0^{3/2}$), which is attributed to the nonlinear conductivity effect caused by the electrical breakdown of fluids [193]. Although several models have been proposed to account for the behavior of ER fluids, these models have some limit to cover the behavior of GER fluids. Huang *et al*. suggested the surface polarization layer model based on their experimental observation [73, 194]. In the surface polarization layer model, it is a crucial element that the surface dipoles form two aligned layers in the contact region. The aligned dipole layers generate an electrostatic force that holds the two particles together. The overlap of two particles is determined by the equilibrium of the electrostatic force and the elastic force between the neighboring particles. According to this model, the yield stress is referred to as the shear stress at which the two neighboring particles irreversibly lose contact.

The fast response and reproducibility of small-sized DS HNP-based ER fluid were observed by measuring shear stress under the electric field on and off (Figure 32). The small-sized DS HNP-based ER fluid showed more

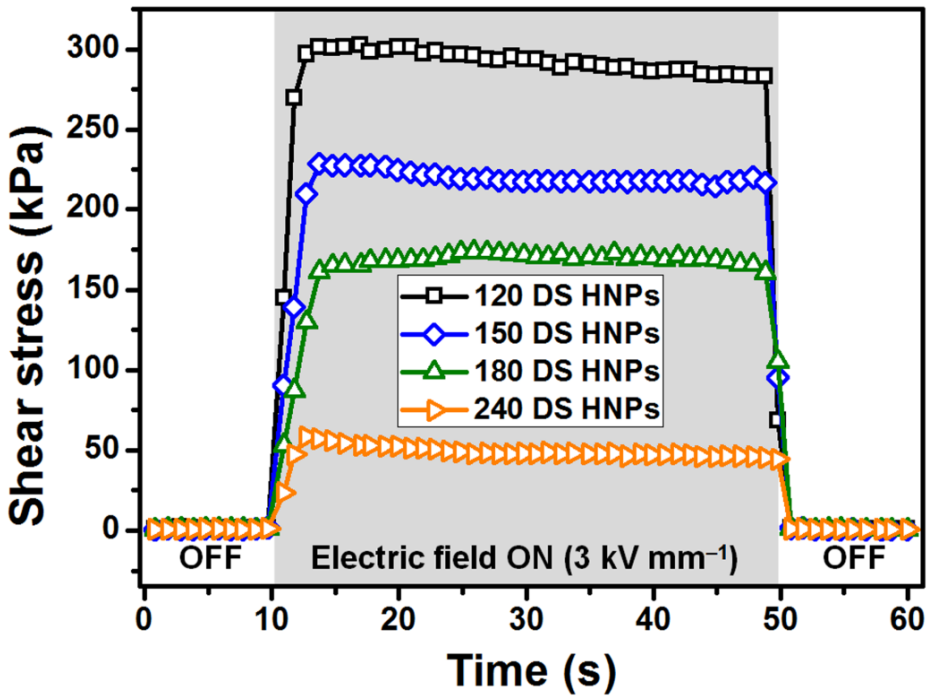

Figure 32. Effect of switching the electric field on shear stress. The shear rate was 0.1 s^{-1}.

enhanced shear stress and faster response and recovery time than the ER fluid having relatively large-sized particles. These phenomena were ascribed to the synergistic effect of higher mobility and higher external surface area resulted from the small-sized diameter [122].

Total surface area (A_{BET}) and pore distribution of the DS HNPs were directly acquired from Brunauer–Emmett–Teller (BET) analysis (Table 5). In addition, surface area of the small pores within shells (A_{ISP}) and the surface of the shells except small pores within shells (A_{shell}) were calculated in order to investigate the relationship between surface area and ER performance using the formula below:

$$A_{shell} = 3V_{SiO_2/TiO_2}(R^2 + r^2)/(R^3 - r^3)$$

$$A_{BET} = A_{ISP} + A_{shell}$$

where V_{SiO_2/TiO_2} (= 0.333 $cm^3\ g^{-1}$) is the specific volume of the SiO_2/TiO_2 composites, and R and r are the outer and inner radius of the shell, respectively [195]. A_{BET} increased with increasing the size of DS HNPs, reaching 497 $m^2\ g^{-1}$ at 240 nm. The DS HNPs contain small pores (size : 3–4 nm) and large pores (size : 30–35 nm) formed in the intrashell and inner cavity, respectively. At the initial stage of the etching process, silica in the titania/silica interface is first etched out but not titania. With continuous etching under sonication, high intensity energy arises from the cavity between silica and titania made at the

Table 5. Brunauer-Emmett-Teller (BET) analysis of four different-sized (120, 150, 180, and 240 nm) DS HNPs for measurement of surface area and volume ratio of small pores (3–4 nm) and large pores (30–35 nm) in DS HNPs.

Samples	A_{BET}[a]	A_{shell}[b]	A_{ISP}[c]	Small pore	Large pore
	[$m^2 g^{-1}$]	[$m^2 g^{-1}$]	[$m^2 g^{-1}$]	[%]	[%]
120 DS HNPs	317	112	205	36	64
150 DS HNPs	351	89.0	262	49	51
180 DS HNPs	366	63.0	303	55	45
240 DS HNPs	497	45.0	452	85	15

[a] A_{BET} : total surface area.

[b] A_{shell} : surface area of the shell except small pores within shells

[c] A_{ISP} : surface area of the small pores within shells

initial stage. Therefore, corrosion of both titania and silica occurs under the stringent conditions [174]. The etched fragments of titania and silica are released and diffused to the titania shell layer. Subsequently, these fragments of titania and silica condensate and redeposit on the titania shell by Ostwald ripening [196, 197]. Consequently, small pores (size : 3–4 nm) and large pores (size : 30–35 nm) are formed in the intrashell and inner cavity, respectively, as a result of the sonication-mediated etching and redeposition process. The ratio of small pores to large pores increased with the increasing size of DS HNPs, which verifies that more intrashell pores exist in bigger sizes of DS HNPs (Figure 33). Therefore, the DS HNPs having an average diameter of 240 nm exhibited the largest A_{BET} due to the large A_{ISP} generated by the small pores within thicker shells of the DS HNPs. However, small pores within shells have little effect on enhancing ER performance because the polarization derived by large pores formed in the inner cavity is stronger than the polarization derived by small pores within the shell under an electric field. In other words, charge accumulation occurs more readily in surface sites formed by large pores than in those formed by small pores. Consequently, the surface area of the shell, except small pores within shells (A_{shell}), plays a critical role in enhancing ER properties by increasing the interfacial polarizability of particles. Among the fabricated DS HNPs with different diameters, 120 nm-sized DS HNPs (120 DS

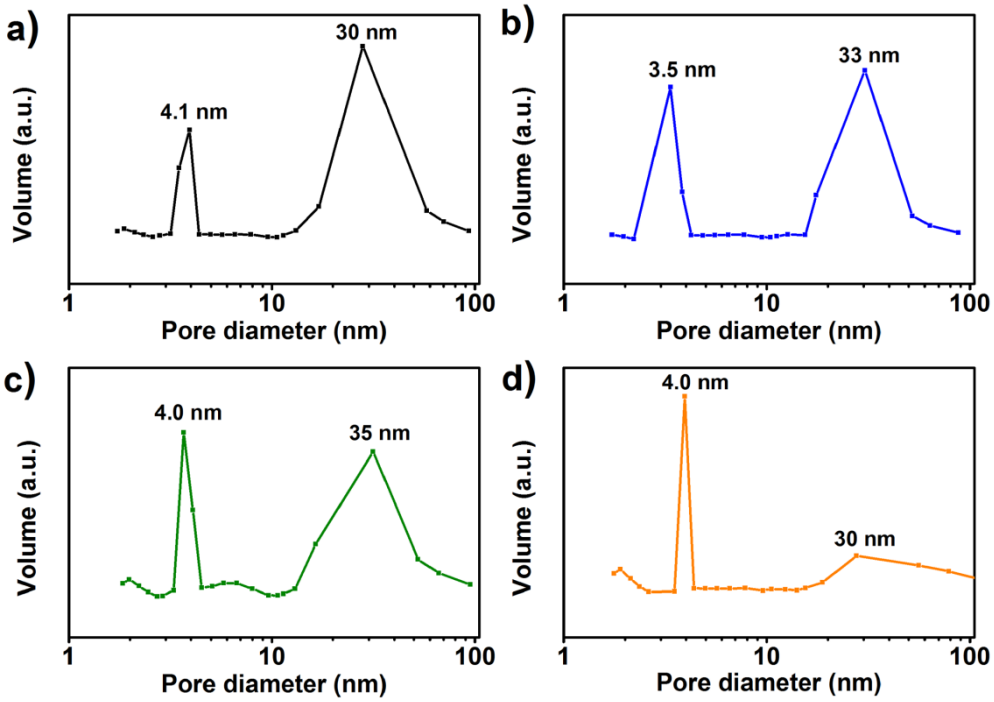

Figure 33. The pore volume distribution of a) 120 nm, b) 150 nm, c) 180 nm, and d) 240 nm DS HNPs derived from the desorption isotherms.

HNPs) exhibited the highest A_{shell} of 112 $m^2 g^{-1}$, which means 120 DS HNPs tends to polarize more easily under an applied electric field.

In addition, the dielectric properties of electro-responsive materials are associated with ER activities because of the orientational polarization (Debye polarization) and interfacial polarization (Wagner polarization) generated under an electric field [148, 179]. To gain an in-depth insight into the influence of dielectric properties of electro-responsive materials on ER effect, permittivity and loss factor were measured as a function of the electric field frequency (Figure 34, 35). The plotted lines in Figure 34 were obtained by the following equation:

$$\varepsilon^* = \varepsilon' + \mathrm{i}\varepsilon'' = \varepsilon_\infty + \frac{\Delta\varepsilon}{\{1 + (i\omega\lambda)^{1-\alpha}\}^\beta}$$

where ε' is the permittivity, ε'' is the dielectric loss factor, ε_0 is the static permittivity ($\varepsilon_0 = \lim_{\omega\to 0} \varepsilon^*(\omega)$), ε_∞ is the fictitious permittivity ($\varepsilon_\infty = \lim_{\omega\to\infty} \varepsilon^*(\omega)$), $\Delta\varepsilon$ is the polarizability ($\Delta\varepsilon = \varepsilon_0 - \varepsilon_\infty$), ω is the angular frequency, and λ is the characteristic relaxation time of the medium. The exponents α and β denotes the asymmetry and broadness of the corresponding spectra, respectively [180, 198]. The specific values of dielectric parameters for DS HNP-based ER fluids were described in Table 6. The smaller DS HNPs-based ER fluid exhibits larger polarizability, which is associated with the strong particle polarization [199, 200]. This phenomenon can be elucidated

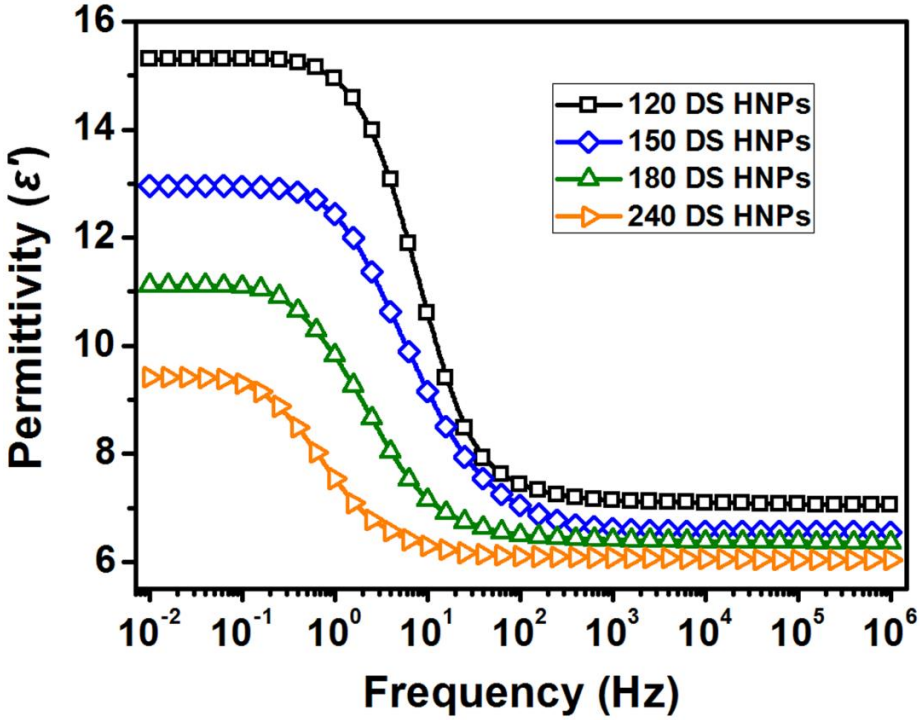

Figure 34. Permittivity (ε') as a function of electric field frequency for four different-sized (120, 150, 180, 240 nm) DS HNPs-based ER fluids (10 wt% in silicone oil).

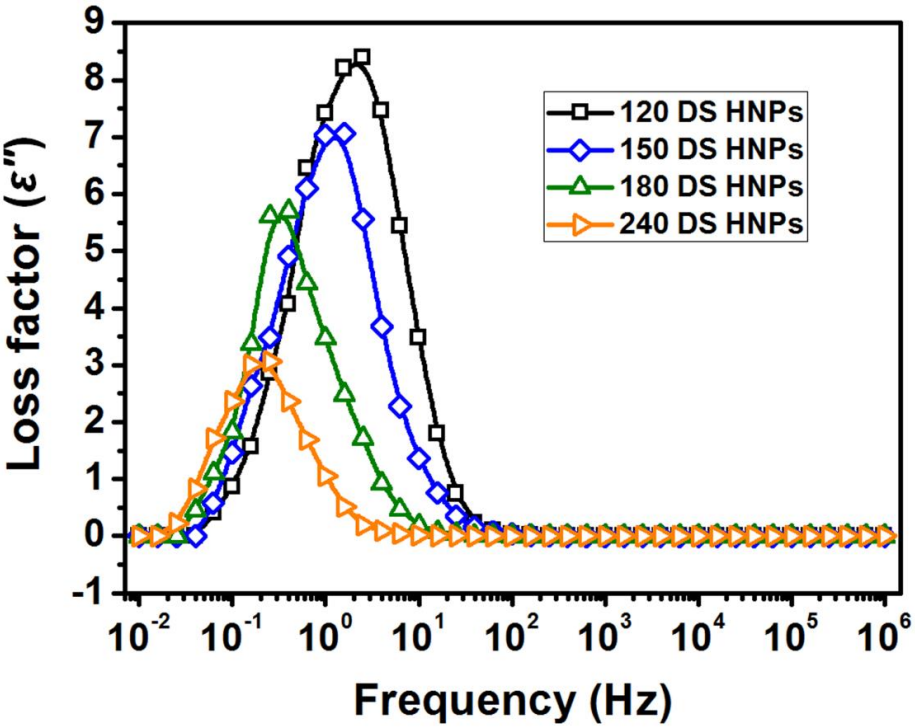

Figure 35. Loss factor (ε'') as a function of electric field frequency for four different-sized (120, 150, 180, 240 nm) DS HNPs-based ER fluids (10 wt% in silicone oil).

Table 6. Dielectric parameters for DS HNPs-based ER fluids.[a]

Particle size	ε_0	ε_∞	$\Delta\varepsilon=\varepsilon_0-\varepsilon_\infty$	f_{max}[b]	λ[c]
120 nm	15.30	7.06	8.24	2.05 Hz	0.0776 s
150 nm	12.95	6.55	6.40	1.24 Hz	0.128 s
180 nm	11.12	6.36	4.76	0.343 Hz	0.464 s
240 nm	9.42	6.04	3.38	0.209 Hz	0.762 s

[a] Dielectric parameters were examined by an impedance analyzer (1260, Solartron) with a dielectric interface (1296, Solartron).

[b] The local frequency of the peak on the dielectric loss factor ε'' and the f_{max} values were measured by nonlinear regression analysis using OriginPro.

[c] The relaxation time, denoted by $\lambda=1/(2\pi f_{max})$ (f_{max} is the frequency of the loss peak).

by higher surface area of the shell except small pores within shells in the smaller DS HNPs because the high surface area of the shell except small pores within shells can produce more surface sites for charge carrier accumulation [201, 202]. Furthermore, the relaxation times (λ) which is related to the interfacial polarization are estimated by the following equation:

$$\lambda = \frac{1}{2\pi f_{max}}$$

where f_{max} denotes the frequency at maximum dielectric loss factor [203, 204]. The relaxation time significantly decreased as the diameter of DS HNPs was reduced. In other words, the smaller DS HNPs-based ER fluid represented the faster polarization rate than the larger DS HNPsbased ER fluid.

The yield stress of ER fluids was measured as a function of temperature under a zero field condition (Figure 36). The yield stress of ER fluids was reduced as temperature increased, which is attributed to the reduction of both zero-field viscosity and dielectric constant of silicone oil with rising temperature [205, 206]. On the contrary, the yield stress was enhanced with increasing temperature under an electric field (Figure 37). Even though Brownian motion was intensified due to the increased temperature, the Brownian force could be overcome by the increased interparticle interaction force which was ascribed to the enhanced interfacial polarization [207]. The enhancement of interfacial polarization is related to the dielectric constant of

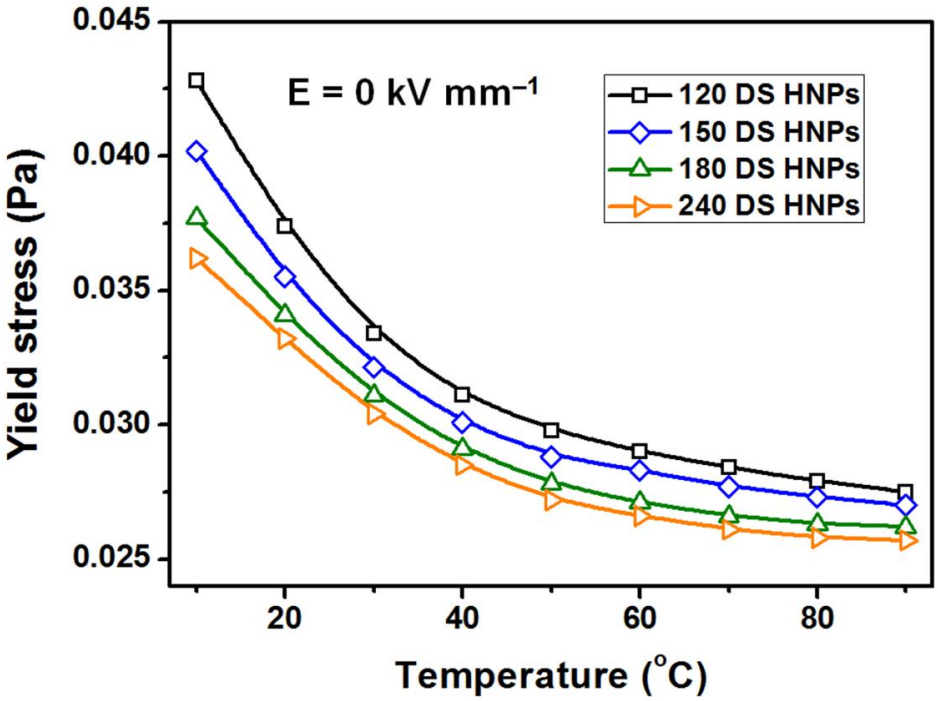

Figure 36. Yield stress of four different-sized (120, 150, 180 and 240 nm) DS HNPs-based ER fluids (10 wt% in silicone oil) without an electric field.

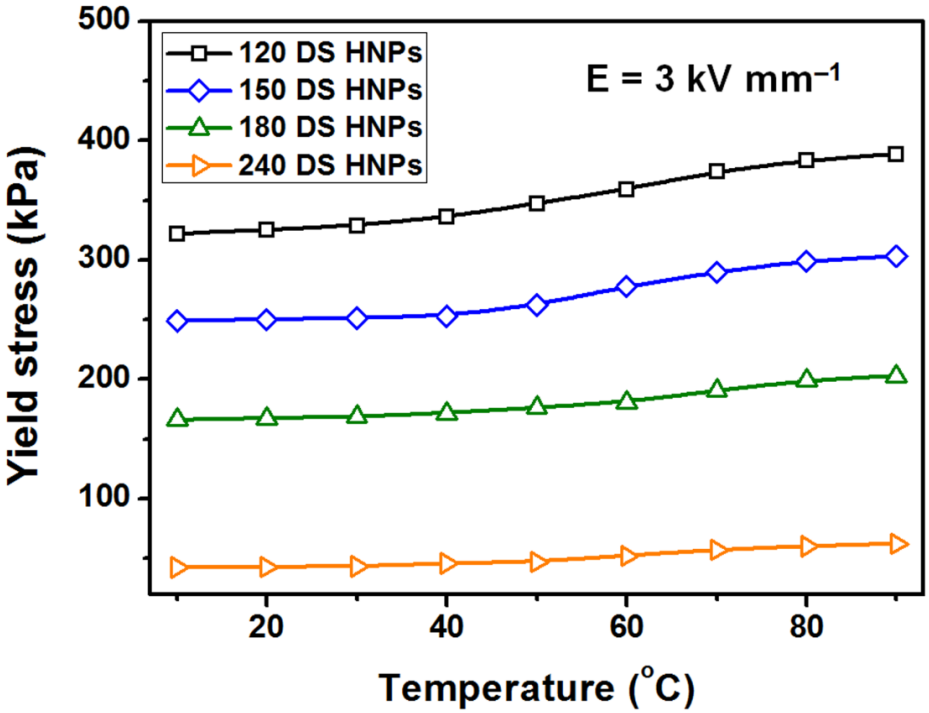

Figure 37. Yield stress of four different-sized (120, 150, 180 and 240 nm) DS HNPs-based ER fluids (10 wt% in silicone oil) under an electric field of 3 kV mm^{-1}.

ER fluids. It has been reported that the dielectric constant of ER fluids generally increased with rising temperature, which is associated with the enhancement of interfacial polarization with increasing temperature under an electric field [208, 209]. Moreover, the viscosity of silicone oil which was used as a liquid medium decreased with rising temperature, which makes it easy for electro-responsive materials to form fibril-like structure under an electric field [207]. For the reasons mentioned above, the yield stress of ER fluids was enhanced with increasing temperature. This tendency was observed for all ER fluids fabricated in this work. Namely, the prepared ER fluids composed of double-shell SiO_2/TiO_2 hollow nanoparticles exhibited excellent and stable performance over a wide range of temperature.

In particular, the DS HNPs dispersed in silicone oil showed an outstanding antisedimentation property because of their low density ascribed to the hollow structure (Figure 38). The sedimentation ratio was maintained above 0.88 even after ninety days. It is noteworthy that the antisettling property was improved as the diameter of DS HNPs decreased. To evaluate the antisedimentation property of the DS HNPs mathematically, sedimentation velocity of the DS HNPs was determined using the Stokes' law as follows:

$$V_g = d^2(\rho_p - \rho_l)/18\eta \times G$$

where V_g denotes sedimentation velocity, d is particle diameter, ρ_p indicates

particle density, ρ_l indicates liquid density, η is liquid viscosity, and G is gravitational acceleration [210, 211]. As described in Table 7, the sedimentation velocities of DS HNPs were remarkably low. Judging from the calculated sedimentation velocities of DS HNPs, the small-sized DS HNPs showed superior antisedimentation behavior.

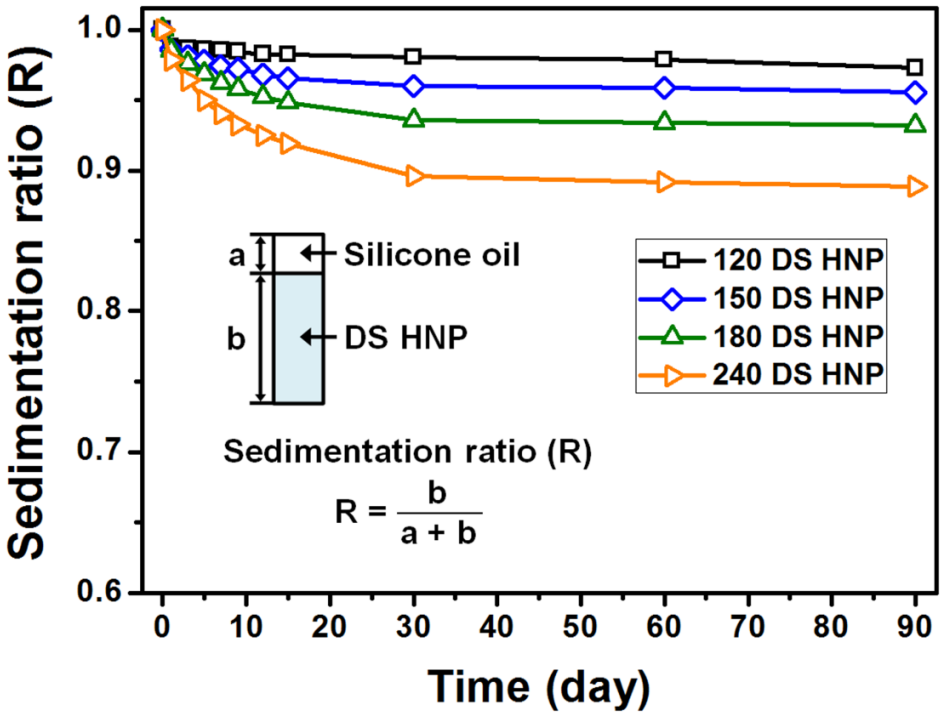

Figure 38. Sedimentation properties of the DS HNPs-based ER fluids with four different diameters (120, 150, 180, and 240 nm). Concentration of the ER fluilds was 10 wt% in silicone oil [inset: definition of sedimentation ratio].

Table 7. Physical parameters and sedimentation velocity of DS HNPs.

Particle size[a]	120 nm	150 nm	180 nm	240 nm
Particle density[b] (g cm^{-3})	2.68	2.70	2.71	2.74
Fluid density[c] (g cm^{-3})	1.01	1.01	1.01	1.01
Fluid viscosity[c] (Pa·s)	0.101	0.101	0.101	0.101
Sedimentation velocity[d] ($\times 10^{-10}$ m s^{-1})	1.30	2.05	2.97	5.37

[a] The average particle size was confirmed by TEM (50 particles counted).

[b] Particle density was measured using density hydrometer at a standard temperature of 20 ℃.

[c] Silicone oil [poly(methylphenylsiloxane), kinetic viscosity = 100 cSt] was used as a dispersing medium.

[d] Sedimentation velocity was determined according to Stokes' law. Particle Reynolds number was less than 0.2.

3.3. Electro-Responsive Behavior Depending on Electrical Conductivity

3.3.1. Fabrication of few-layer MoS_2 nanosheets

Few-layer MoS_2 nanosheets were fabricated through mild grinding and subsequent delamination step using sonication. Lightly-exfoliated MoS_2 nanosheets were collected as a powder form for the characteristic analysis of MoS_2 nanosheets and fabrication of MoS_2 nanosheets-based ER fluids. To obtain few-layer nanosheets, additional steps for selecting the certain size were conducted by using centrifugation. The additional steps facilitated not only size selection of the few-layer nanosheets but also high-yield production which is imperative for preparing ER fluids. The yield of the few-layer MoS_2 nanosheets was *ca.* 62.5%.

The size and morphology of the fabricated few-layer MoS_2 nanosheets were identified by TEM (Figure 39). Judging from the TEM images, it was confirmed that the MoS_2 nanosheets after peeling the bulk MoS_2 off consisted of few layers. The size of the few-layer MoS_2 nanosheets was *ca*. 200–400 nm which is approximately 3 times smaller than that of pristine MoS_2. The thickness of the few-layer MoS_2 nanosheets was examined using AFM (Figure 40). By analyzing the height profile, the thickness of the MoS_2 nanosheets was estimated as *ca.* 5.1 nm, indicating that the few-layer MoS_2 nanosheets were

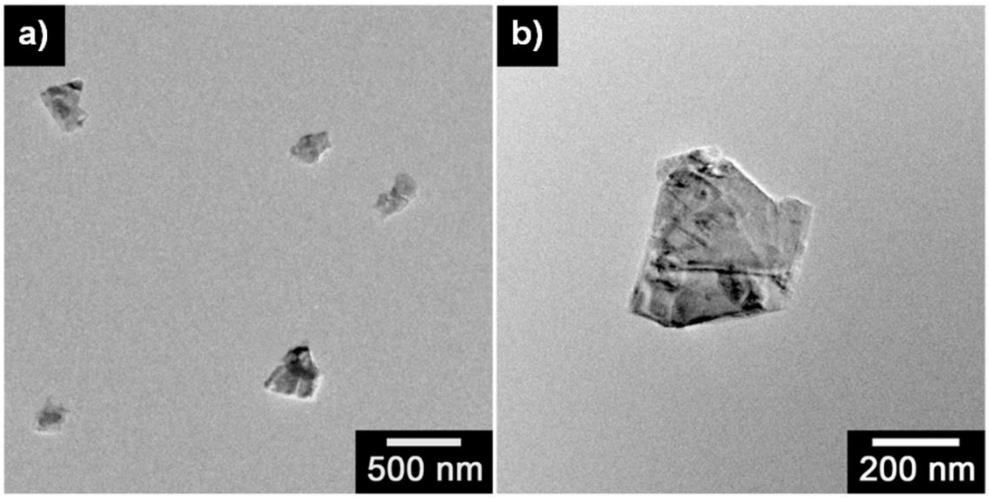

Figure 39. TEM images of few-layer MoS_2 nanosheets at a) low magnification, and b) high magnification.

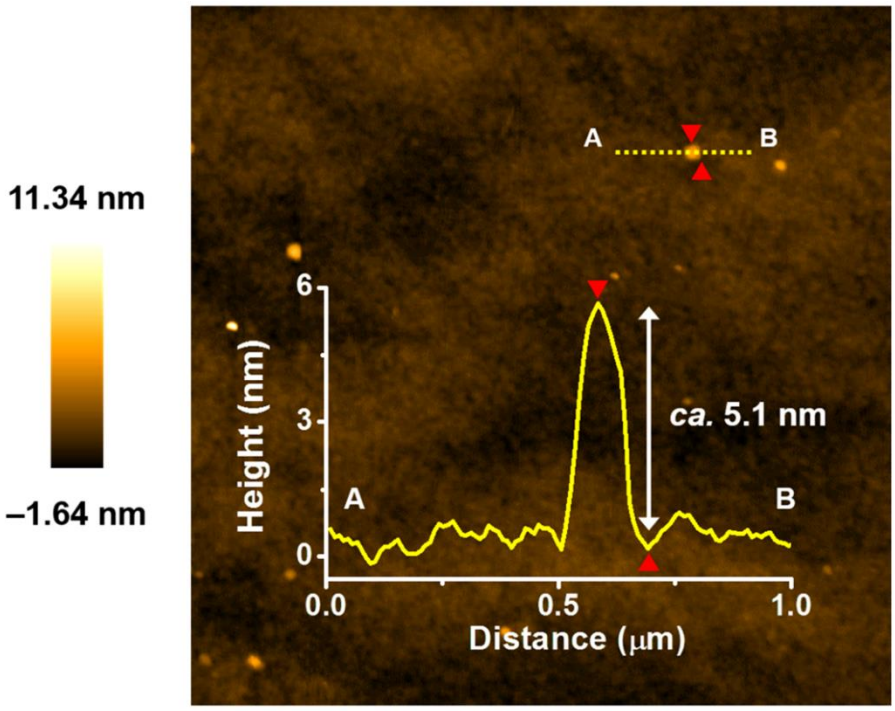

Figure 40. AFM image of few-layer MoS_2 nanosheets. From the height profile analysis, the thickness of the MoS_2 nanosheets was measured as *ca.* 5.1 nm.

composed of 5–6 layers since the thickness of monolayer MoS_2 was generally close to 1 nm [212].

To characterize the structural polytypes of the prepared MoS_2 nanosheets, XPS was adopted. The chemical states of Mo 3d and S 2s regions were identified depending on the annealing temperature (Figure 41). The binding energies of Mo^{4+} $3d_{3/2}$ and Mo^{4+} $3d_{5/2}$ correspond to the peaks at 232.6 eV and 229.5 eV, respectively. The Mo^{6+} peak observed at 236.0 eV was associated with the oxidation of MoS_2 during the fabrication process. No obvious difference of XPS spectra was discovered with the change of the annealing temperature, demonstrating no phase transition after heat treatment (Figure 42).

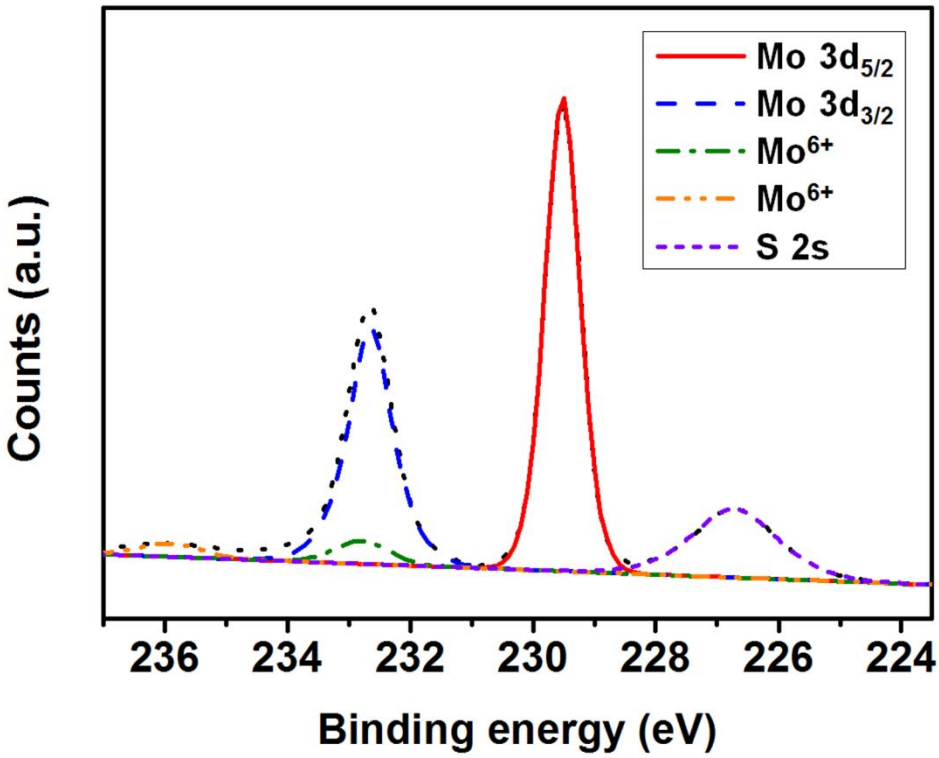

Figure 41. XPS spectra of few-layer MoS_2 nanosheets prepared without thermal treatment.

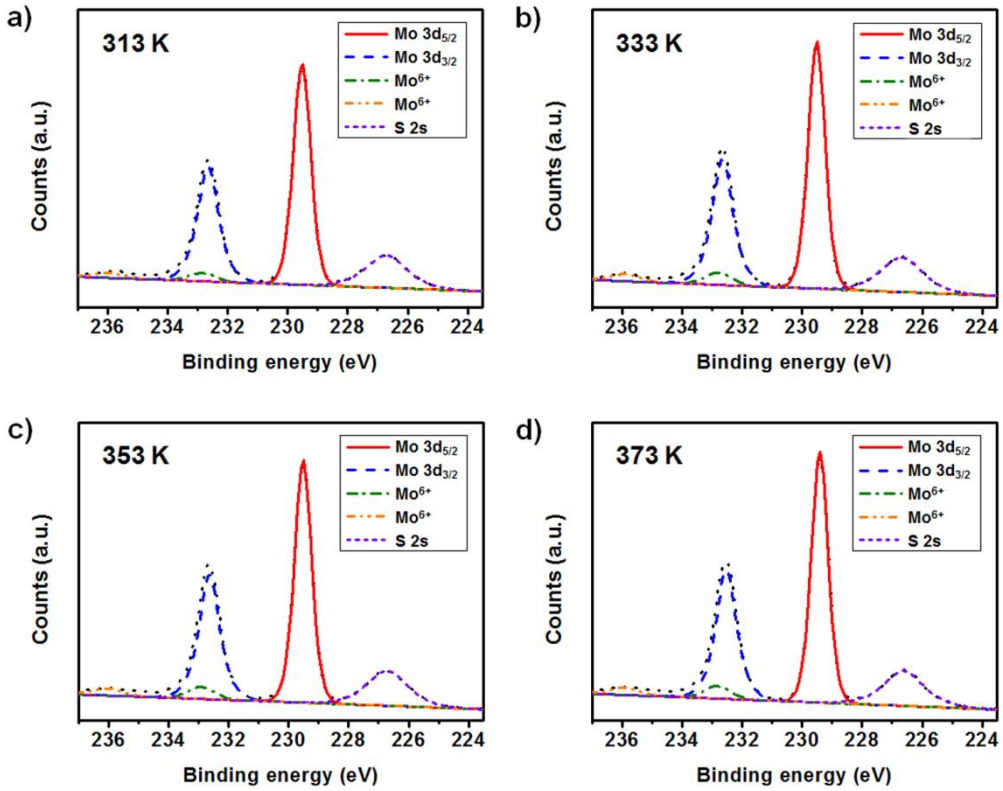

Figure 42. XPS spectra of few-layer MoS_2 nanosheets prepared through thermal treatment at a) 313 K, b) 333 K, c) 353 K, and d) 373 K.

3.3.2. Characteristics analysis of few-layer MoS_2 nanosheets depending on annealing temperature

To achieve an in-depth insight into the structural information of the few-layer MoS_2 nanosheets depending on the annealing temperature, Raman spectra were measured with ex-situ heat treatments (Figure 43). Two prominent peaks at 380 cm^{-1} and 406 cm^{-1} correspond to the in-plane phonon mode E^1_{2g} and out-of-plane phonon mode A_{1g} of MoS_2, respectively. The number of layers can be deduced from the gap of E^1_{2g} and A_{1g} peaks since the peaks are more separated with increasing the number of layers owing to the stiffening of A_{1g} mode [213]. Unlike the monolayer MoS_2 whose gap between E^1_{2g} and A_{1g} was *ca*. 19 cm^{-1}, an increase in the number of layers induces the redshift of E^1_{2g} mode and the blueshift of A_{1g} mode simultaneously. As the gap of these two peaks in this work was *ca*. 25.7 cm^{-1}, judging from the gap of E^1_{2g} and A_{1g} peaks, it can be estimated that the fabricated MoS_2 nanosheets are comprised of 5–6 layers, which is in agreement with the thickness confirmed by AFM [213, 214].

Both peaks from the phonon modes E^1_{2g} and A_{1g} displayed explicit redshifts at elevated temperature. To demonstrate the thermal behavior of the few-layer MoS_2 nanosheets, the aforementioned shift in peak position of two phonon modes was evaluated by fitting the peak position (ω) with the change

of temperature (T) according to the following equation:

$$\omega(T) = \omega_0 + \chi T$$

where ω_0 denotes the peak position of phonon modes E^1_{2g} or A_{1g} at 0 K, and χ is the 1st-order temperature coefficient of E^1_{2g} or A_{1g} modes. Previous studies on the thermal behaviors of the layered bulk MoS_2 and few-layer MoS_2 prepared by chemical vapor deposition (CVD) reported that the χ values of E^1_{2g} and A_{1g} peaks were found to be –0.0132 cm^{-1} K^{-1} and –0.0123 cm^{-1} K^{-1} for vapor-phase grown few-layer MoS_2. In addition, the χ values of E^1_{2g} and A_{1g} peaks for bulk MoS_2 were revealed as –0.0147 cm^{-1} K^{-1} and –0.0123 cm^{-1} K^{-1} respectively [215]. For the few-layer MoS_2 nanosheets fabricated in this work, the χ values of E^1_{2g} and A_{1g} peaks were calculated as –0.016 cm^{-1} K^{-1} and –0.017 cm^{-1} K^{-1} respectively, which was similar with the results of previous research. Moreover, the peak intensity ratio of E^1_{2g} mode to A_{1g} mode decreased from 0.99 to 0.73 as the temperature was elevated, indicating that interlayer phonon modes were enhanced through annealing process. In addition, both E^1_{2g} and A_{1g} peaks broadened with increased full width at half maximum (FWHM) values. The change of FWHM depending on annealing temperature was attributed to the thermal expansion or temperature contribution caused by anharmonicity [215, 216].

Moreover, the vibration modes J_1 (150 cm^{-1}), J_2 (196 cm^{-1}), and J_3 (339

cm^{-1}) related to the distorted state (1T' phase) were detected for the few-layer MoS_2 nanosheets [217]. On the contrary, no such peaks were detected for the bulk MoS_2 and vapor-phase grown few-layer MoS_2. Considering the differences of the χ values and the presence of J_1–J_3 modes, the fabricated MoS_2 nanosheets behave as 2H-MoS_2 with distortions, different from erstwhile reports that introduced the bulk MoS_2 and few-layer MoS_2 prepared by CVD [215, 216]. Moreover, the peak intensity of J_1–J_3 vibration modes were more diminished at higher annealing temperature. The atomic rearrangements of MoS_2 from 1T' to 2H phase resulted in the decrease in the J_1–J_3 peaks as those peaks are the evidence of recovering superlattice formation with distorted Mo atoms in a unit cell [218].

Besides, the J_1–J_3 peaks of Raman spectra remained even after repeating the centrifugation step several times. This phenomenon indicated that the precipitated MoS_2 nanosheets maintained their structures without restacking since the intensity of the peaks originated from 1T' phase were not distinctly observed in the case of restacked MoS_2 [219].

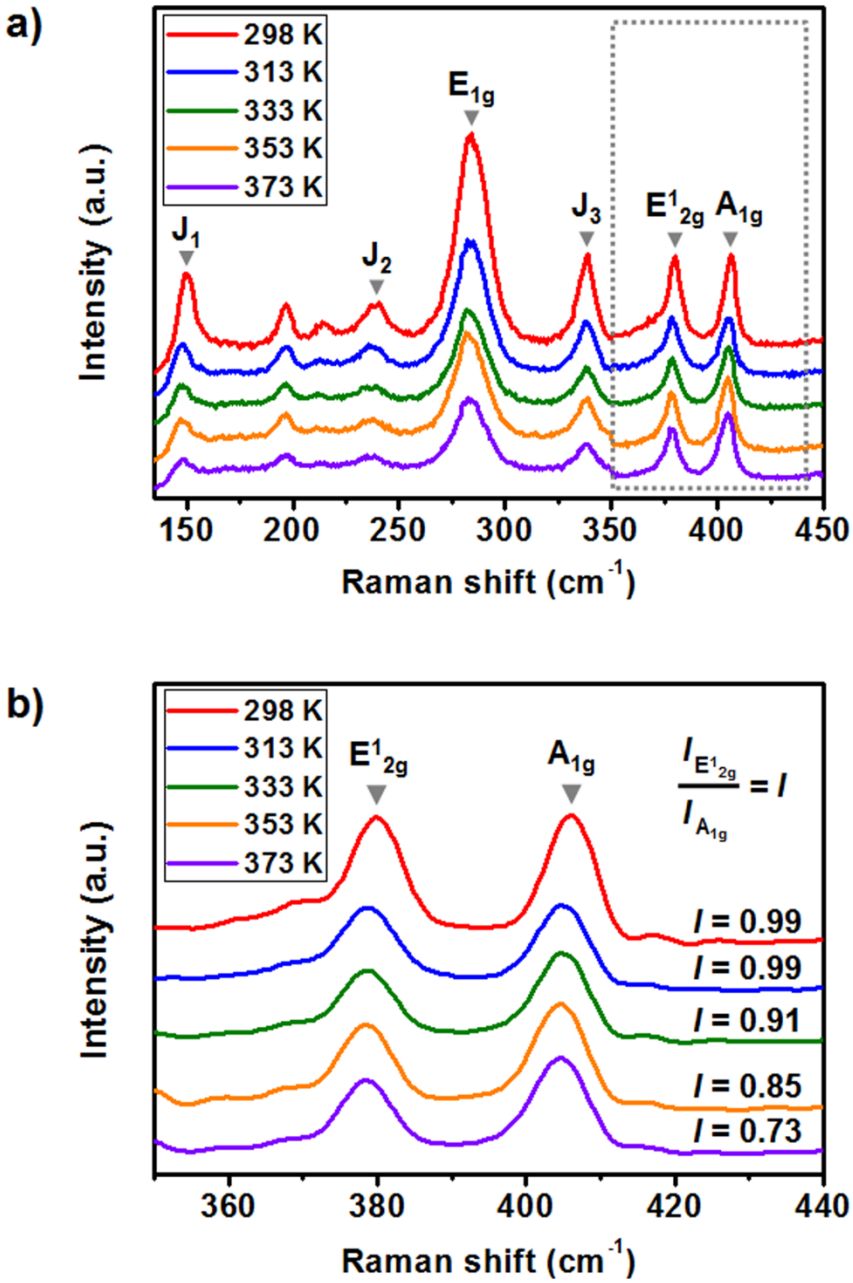

Figure 43. a) Raman spectra of few-layer MoS_2 nanosheets prepared through thermal treatment at different annealing temperature. b) Enlarged Raman spectra of the rectangular part.

To understand the electronic behaviors of the few-layer MoS_2 nanosheets, UV-visible spectra were examined at room temperature (Figure 44). The resultant UV-visible spectra offered information about the excitonic transitions of the few-layer MoS_2. Prior to the measurement of UV-visible spectra, the MoS_2 nanosheets were suspended and diluted in the mixture of ethyl alcohol and distilled water. Remarkable peaks were observed at 629 nm (1.97 eV) and 693 nm (1.79 eV) which were suggested as the proof of an existence of MoS_2 nanosheets [220, 221]. Two peaks verified direct transitions of A and B excitons at the K point of the Brillouin zone, respectively. Furthermore, the shoulder peaks at 824 nm (1.50 eV) and 891 nm (1.39 eV) with small intensity corresponded to the indirect-gap transitions of MoS_2. Broad peak centered around 504 nm (2.46 eV) indicated the transition between the deeper states at the M point of the Brillouin zone. These notable peaks of the few-layer MoS_2 nanosheets fairly agreed with the results of previous reports [222, 223].

To investigate the luminescence properties of the few-layer MoS_2 nanosheets, MoS_2 suspension was characterized by photoluminescence (PL) spectroscopy at room temperature (Figure 44 inset). The concentration of MoS_2 suspension was same with what was taken for UV-visible spectroscopy. Under 532-nm laser excitation, the appreciable emission peaks at 638 nm and 670 nm can be assigned to the direct-gap luminescence influenced by an interlayer

coupling and spin-orbit coupling [224]. Furthermore, the diminutive peak at 722 nm implied the indirect-gap luminescence [220].

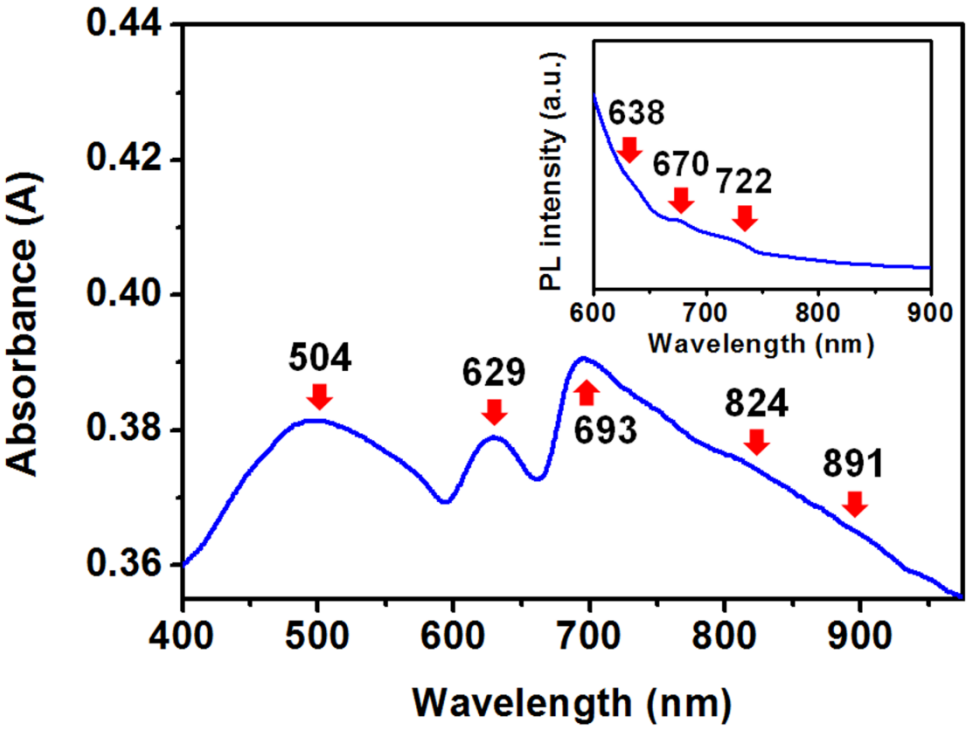

Figure 44. UV-Vis spectrum of few-layer MoS_2 nanosheets. Inset shows PL spectrum of few-layer MoS_2 nanosheets.

Since the vibrational modes of the few-layer MoS_2 were transformed as the annealing temperature was changed, the electrical conductivity thereof was varied depending on the annealing temperature. Figure 45 demonstrates the change of the electrical conductivity of the few-layer MoS_2 nanosheets at elevated temperature from 298 K to 373 K. The electrical conductivity of the few-layer MoS_2 nanosheets increased with increasing the annealing temperature since the MoS_2 is a semiconducting material. The conductivity of the few-layer MoS_2 nanosheets at room temperature was about 9.4×10^{-7} S cm^{-1}. As the temperature increased, the conductivity of the few-layer MoS_2 nanosheets was enhanced to reach 2.2×10^{-4} S cm^{-1} at 373 K, which was approximately two orders of magnitude greater than that of the few-layer MoS_2 nanosheets annealed at 298 K. This conductivity increment with temperature rise was attributed to the typical feature of semiconductors [225].

In the case of semiconductors, it is important to look into the conductivity as a function of temperature because both mobility and carrier concentration are deeply related to the temperature. Two basic types of scattering mechanisms are lattice scattering and impurity scattering that have an effect on the mobility of electron and hole [226]. The impurity scattering which is originated from crystal defects including ionized impurities is typically observed only at fairly low temperature (below 200 K). In the temperature

range at which the analysis carried out, the lattice scattering is dominant in the prepared MoS_2 system. In this case, the electrical conductivity (σ) is proportional to the density of conduction electrons which increases exponentially with temperature as follows:

$$\sigma \propto \exp\left(-E_g/2kT\right)$$

where E_g is the band gap energy of the semiconductor, and k is the Boltzmann constant. In order to determine the band gap energy of the few-layer MoS_2 nanosheets, the logarithm of conductivity was plotted against inverse temperature (Figure 45 inset). From the slope of the plotted curve, the band gap energy of the few-layer MoS_2 nanosheets was acquired as 1.4 eV. The calculated band gap energy of the few-layer MoS_2 nanosheets is in accordance with excitonic transitions from indirect band gap.

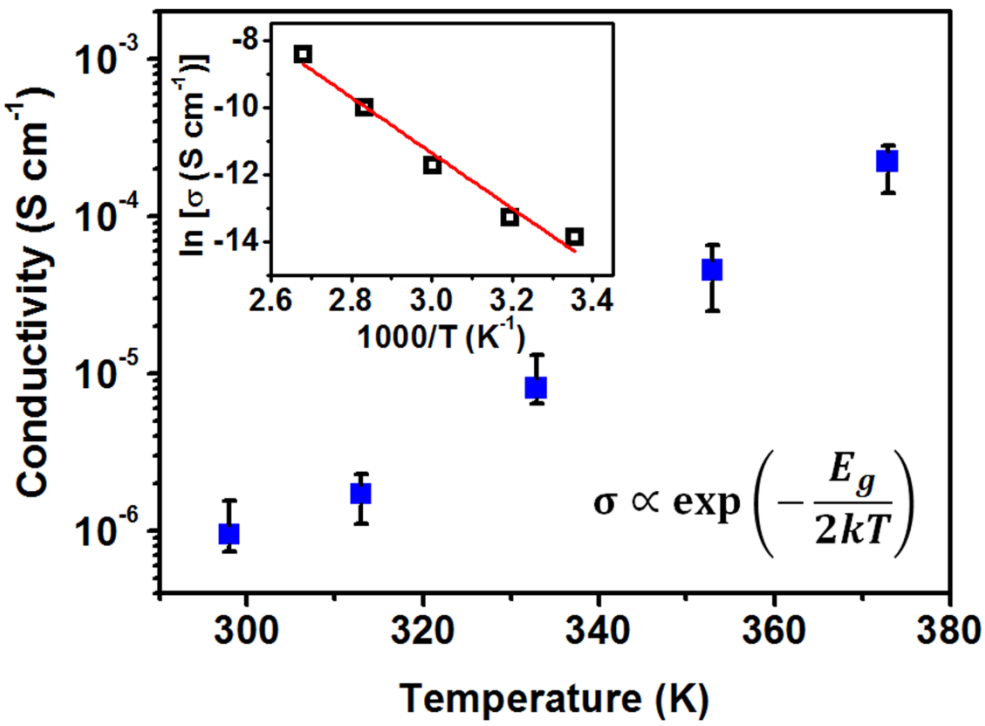

Figure 45. Conductivity of few-layer MoS_2 nanosheets depending on temperature. Inset represents a linear plot of ln σ versus 1/T.

3.3.3. Effect of electrical conductivity on electro-responsive behavior

To gain in-depth insight into the dependence of ER performance on the electrical conductivity of ER material, the few-layer MoS_2 nanosheets-based ER fluids were prepared by dispersing the dried samples in silicone oil. The electrical conductivity of the few-layer MoS_2 nanosheets was controlled by adjusting the annealing temperature. When an electric field was not applied, the ER fluids composed of the few-layer MoS_2 nanosheets represented similar shear stress and viscosity regardless of the electrical conductivity of the MoS_2 nanosheets (Figure 46). The flow behavior of the few-layer MoS_2 nanosheets-based ER fluids corresponds to the Bingham plastic behavior which is described by the following equation:

$$\tau = \tau_0 + \eta_0 \dot{\gamma} \qquad \text{for } \tau \geq \tau_0$$

$$\dot{\gamma} = 0 \qquad \text{for } \tau < \tau_0$$

where τ denotes the shear stress, τ_0 indicates the yield stress, $\dot{\gamma}$ is the shear rate, and η_0 is the shear viscosity [175, 176]. Under an electric field strength of 3.5 kV mm^{-1}, the shear stress of the few-layer MoS_2 nanosheets-based ER fluids slightly decreased with increasing the shear rate until a critical shear rate (Figure 47). Beyond the critical shear rate, the shear stress significantly increased in proportion to the shear rate. At the high shear rate region, all the ER fluids represented similar flow curve because the insufficient time for

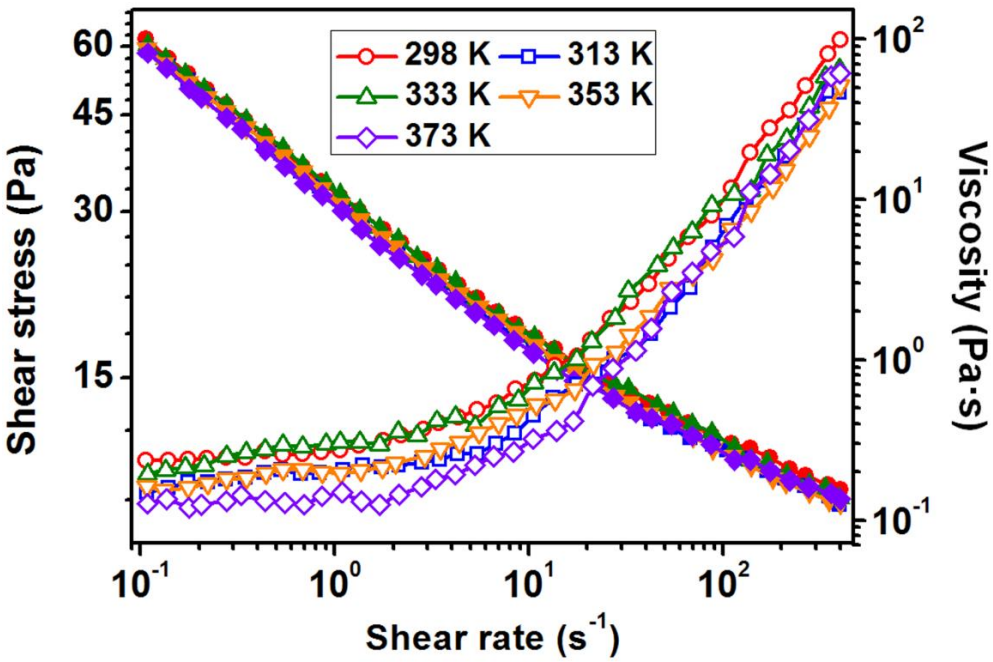

Figure 46. Shear stress (open symbol) and viscosity (closed symbol) of MoS_2-based ER fluids as a function of shear rate without an electric field.

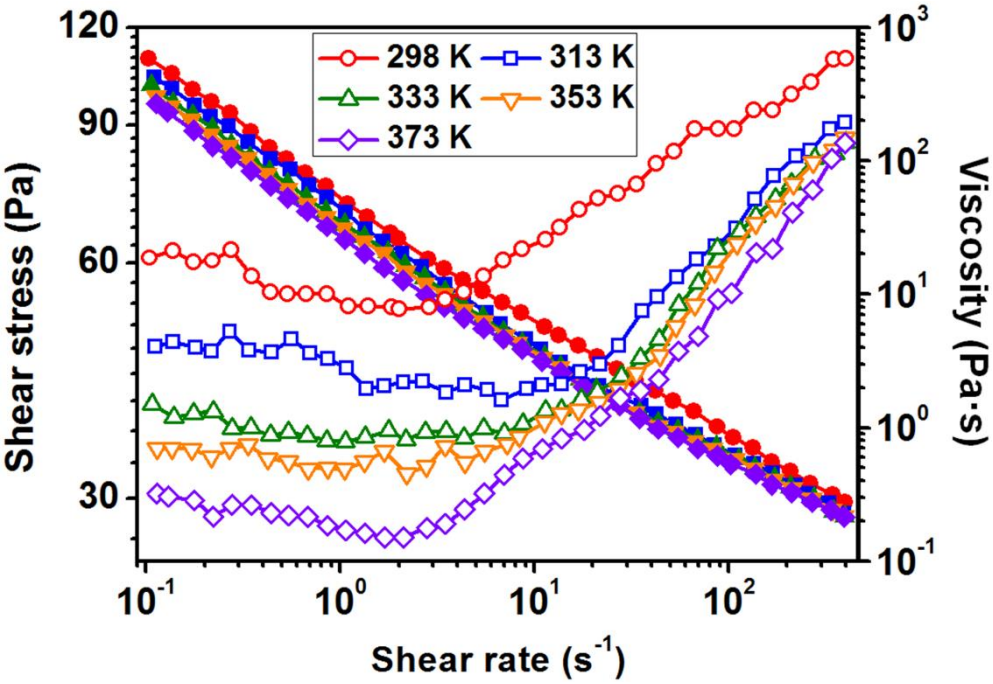

Figure 47. Shear stress (open symbol) and viscosity (closed symbol) of MoS_2-based ER fluids as a function of shear rate under an electric field of 3.5 kV mm^{-1}.

reformation of fibrous structure against shear deformation caused the chain-like structure to collapse. The rheological behavior of the few-layer MoS_2 nanosheets-based ER fluids under the electric field corresponds to the Cho–Choi–Jhon (CCJ) model which was described as follows:

$$\tau = \frac{\tau_y}{1 + (t_1\dot{\gamma})^{\alpha}} + \eta_{\infty}\left(1 + \frac{1}{(t_2\dot{\gamma})^{\beta}}\right)\dot{\gamma}$$

where τ denotes the shear stress, τ_y indicates the dynamic yield stress, t_1 and t_2 are time constants, $\dot{\gamma}$ is the shear rate, η_{∞} refers to the viscosity at infinite shear rate, and the exponent α is associated with the diminishment of shear stress at a low shear rate region, whereas β is related to the high shear rate region ($0 < \beta \leq 1$) [187, 188]. It was noticeable that the few-layer MoS_2 nanosheets-based ER fluids exhibited different ER performance depending on the annealing temperature, which was attributed to the different electrical conductivity. ER efficiency which can be delineated as $(\tau_E - \tau_0)/\tau_0 \times 100$, where τ_E and τ_0 are the yield stress with and without an electric field respectively, of the few-layer MoS_2 nanosheets-based ER fluid was reduced from 475% to 243% as the annealing temperature was enhanced from 298 K to 373 K (Table 8).

To identify the correlation between the electrical conductivity and ER performance, the Wagner model which depicts the interfacial polarization existing in a heterogeneous system was adopted. Since the electrical

Table 8. Electro-responsive properties of MoS_2 nanosheets-based fluids.[a]

Annealing temperature	Zero-field yield stress[b] (Pa)	Yield stress[c] (Pa)	ER efficiency[d] (%)	Response time (s)	Recovery time (s)
298 K	10.6	61.0	475	2.0	1.2
313 K	9.3	47.0	405	1.8	1.1
333 K	10.0	39.7	297	1.7	1.0
353 K	9.5	34.8	266	1.6	0.9
373 K	8.9	30.5	243	1.5	0.8

[a] The concentration of the few-layer MoS_2 nanosheets-based ER fluids was 10 vol% in silicone oil [poly(dimethylsiloxane), kinetic viscosity = 100 cSt].

[b] Zero-field yield stress refers to the yield stress without an electric field.

[c] Yield stress under an applied electric field strength of 3.5 kV.

[d] ER efficiency was calculated according to the following equation: $(\tau_E - \tau_0)/\tau_0 \times 100$, where τ_E and τ_0 denoted the yield stress with and without an electric field respectively.

conductivity of the dispersed materials was far higher than that of the medium in this work, a simplified Wagner model was employed for the interpretation. According to the Wagner's analysis, the dielectric loss tangent ($\tan\delta$) is presented as follows:

$$\tan\delta = \frac{K\omega t}{1+K+\omega^2 t^2}.$$

In this equation,

$$K = \frac{9\phi\epsilon_1}{2\epsilon_1+\epsilon_2},$$

$$t = \frac{2\epsilon_1(n-1)+\epsilon_2}{4\pi\sigma_2},$$

where ϵ_1 and ϵ_2 denote the dielectric constant of the insulating (continuous) phase and conducting (dispersed) phase respectively, σ_2 indicates the electrical conductivity of the latter, ϕ denotes the volume fraction of the conducting material, t signifies the relaxation time of polarization, n is an eccentricity coefficient (n = 1 for a layer type material), ω is the angular frequency of alternating electric field [227, 228].

On the basis of the Wagner's equation, an optimum electrical conductivity of the few-layer MoS_2 nanosheets leading to the strongest ER effect was estimated. Considering that the dielectric loss tangent of the whole ER system strongly rely on the conductivity (σ_2) but weakly rely on the dielectric constant (ϵ_2) of the dispersed material, ϵ_2 is assumed to be constant and to not vary

with σ_2. The dielectric constant of the insulating and conducting phases were assumed to be 2 and 4 respectively (ϵ_1 = 2, ϵ_2 = 4), corresponded to the dielectric constant of the silicone oil and few-layer MoS_2. In addition, the volume fraction of the conducting material was set as 10 vol% (ϕ = 0.1), in accordance with the actual experimental condition of this work. Since the response time of ER fluids is typically scaled at milliseconds, the frequency of the alternating electric field was supposed to be 1000 Hz. As a result of the calculation based on the Wagner's equation, the theoretical optimum conductivity for the strongest ER effect was determined as *ca.* 2.0×10^{-9} S cm^{-1}. Namely, when the electrical conductivity of the ER fluid is *ca.* 2.0×10^{-9} S cm^{-1}, the highest dielectric loss tangent is achieved, resulting in the strongest ER effect.

The measured dielectric constant and the dielectric loss tangent of the few-layer MoS_2 nanosheets-based ER fluids were coincided with the theoretically calculated results (Figure 48, 49). In other words, the ER fluid having conductivity closer to *ca.* 2.0×10^{-9} S cm^{-1} showed higher dielectric constant and loss tangent at a frequency of 1000 Hz, contributing to the stronger ER effect. It has been reported that the suspensions exhibiting a strong ER effect have a high dielectric constant and loss tangent at the frequency 1,000 Hz. Moreover, the ER effect increases as the difference of dielectric constant

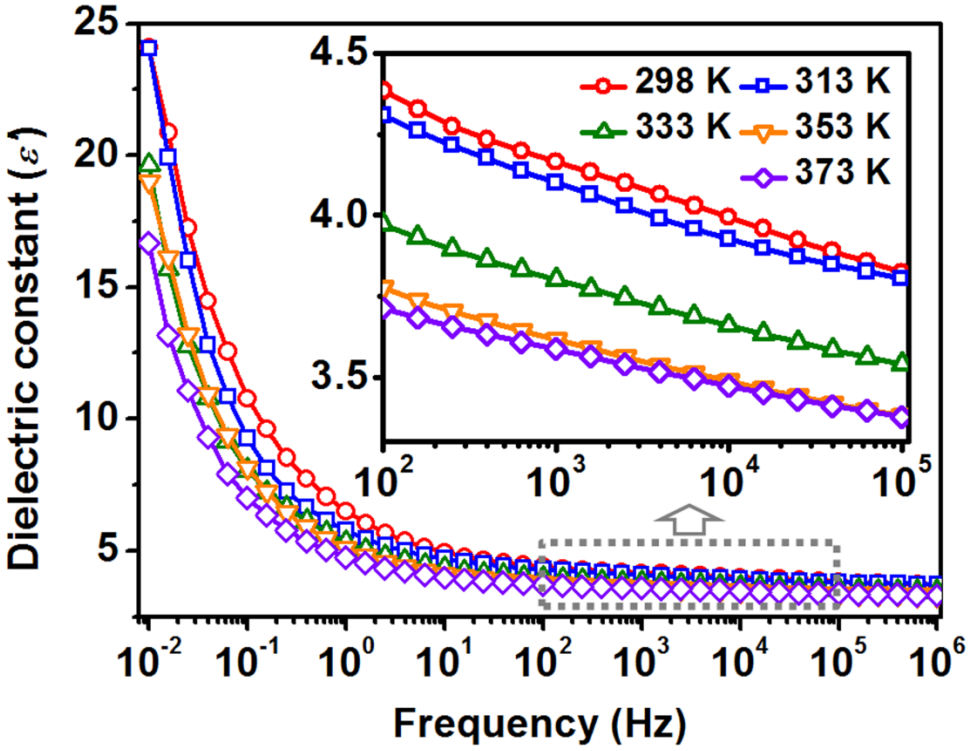

Figure 48. Dielectric constant of various MoS_2-based ER fluids (10 vol% in silicone oil).

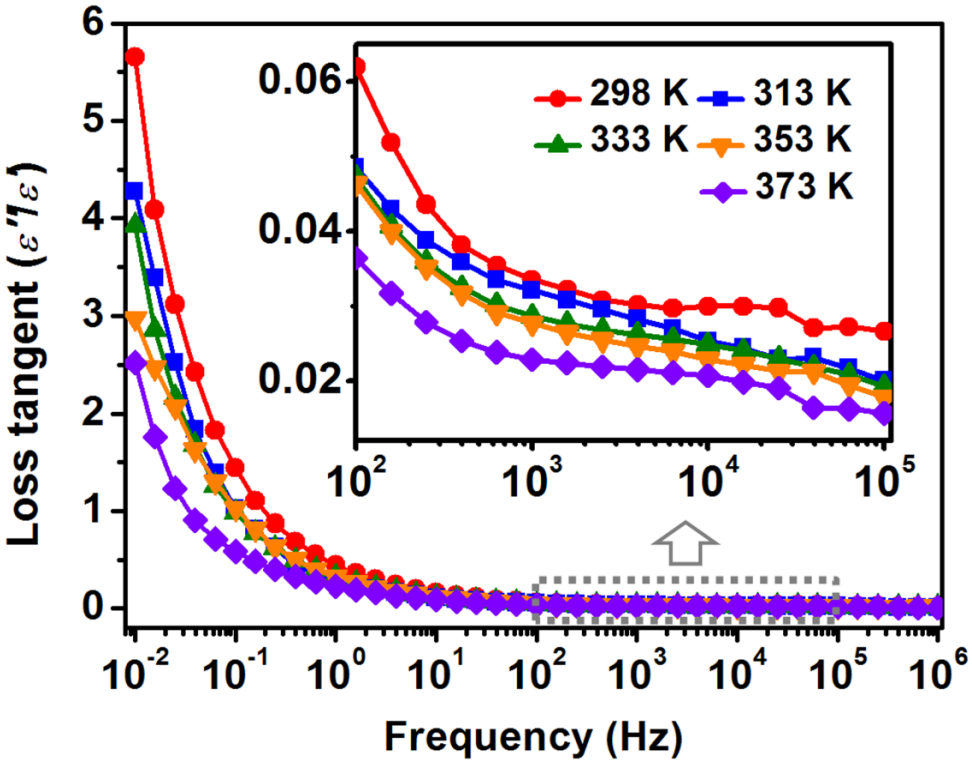

Figure 49. Loss tangent of various MoS_2-based ER fluids (10 vol% in silicone oil).

between 10^2 and 10^5 Hz increases, corresponding to the Maxwell-Wagner polarization. In case of the few-layer MoS_2 nanosheets-based ER fluids, the difference of dielectric constant between 10^2 and 10^5 Hz increased from 0.24 to 0.39 with decreasing the annealing temperature from 373 K to 298 K, resulting in the enhancement of the ER efficiency.

The reproducibility and reversibility of the few-layer MoS_2 nanosheets-based ER fluids were confirmed by measuring the shear stress while an electric field was turned on and off (Figure 50). The response time and recovery time, defined as the time required to reach 90% of its final value, were reduced as the conductivity of ER fluids was enhanced (Figure 51 and Table 8). This phenomenon can be elucidated with the Wagner's equation regarding the relaxation time of polarization. As described in Wagner's equation, the relaxation time of polarization was getting shorter with increasing the electrical conductivity of the dispersed material. It was considered that the electrical conductivity was major factor for the fast response and recovery time since the difference of dielectric constant was slight compared to that of the conductivity.

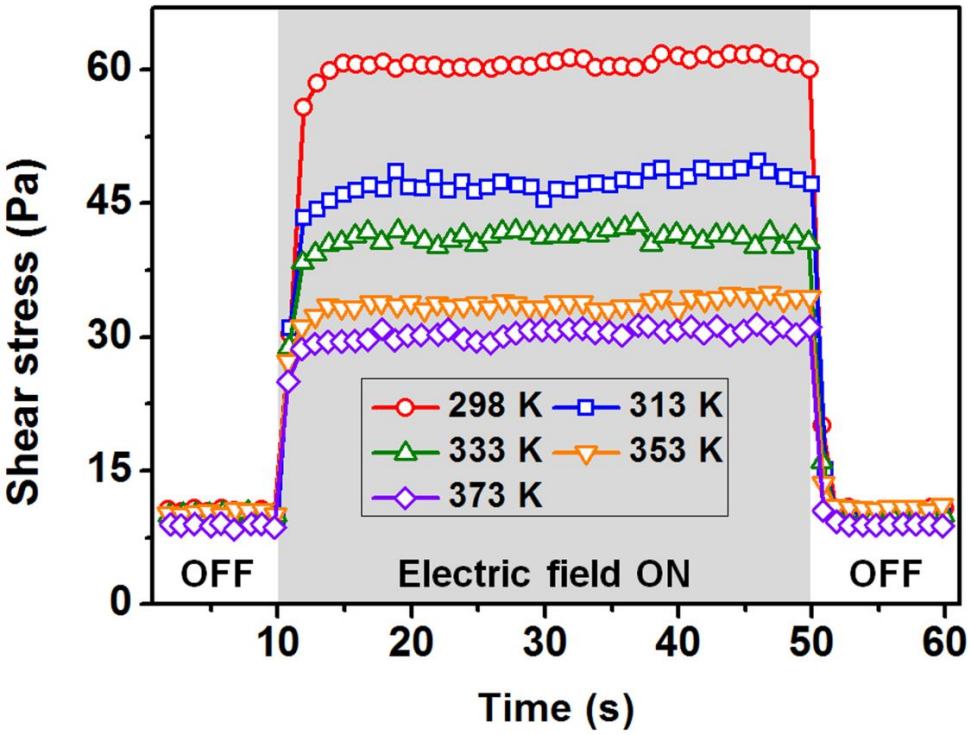

Figure 50. Effect of switching the applied electric field on the shear stress of various MoS_2-based ER fluids. Concentration of MoS_2-based ER fluids was 10 vol% in silicone oil.

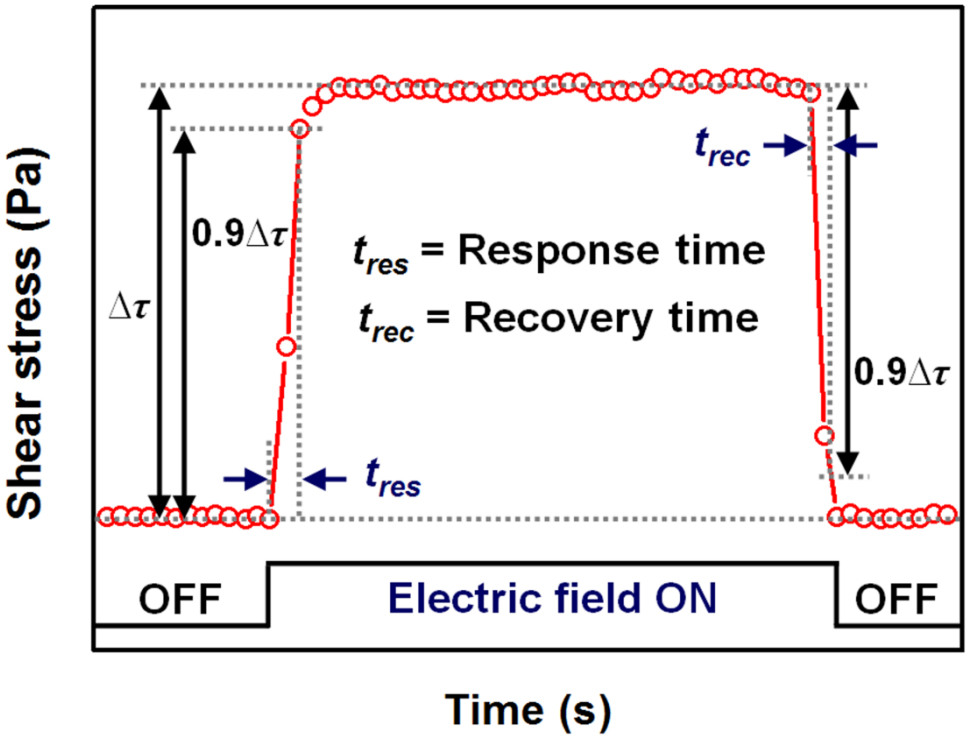

Figure 51. Typical change of shear stress in response to an electric field.

Structural change under an applied electric field was observed in real-time by an optical microscope (Figure 52). As soon as the electric field was applied, the MoS_2 nanosheets were aligned along an applied electric field direction, forming the fibrillar structure. Over time, the fibrous structure became gradually denser and closely linked, which was ascribed to the predominant electrostatic interactions between electro-responsive materials.

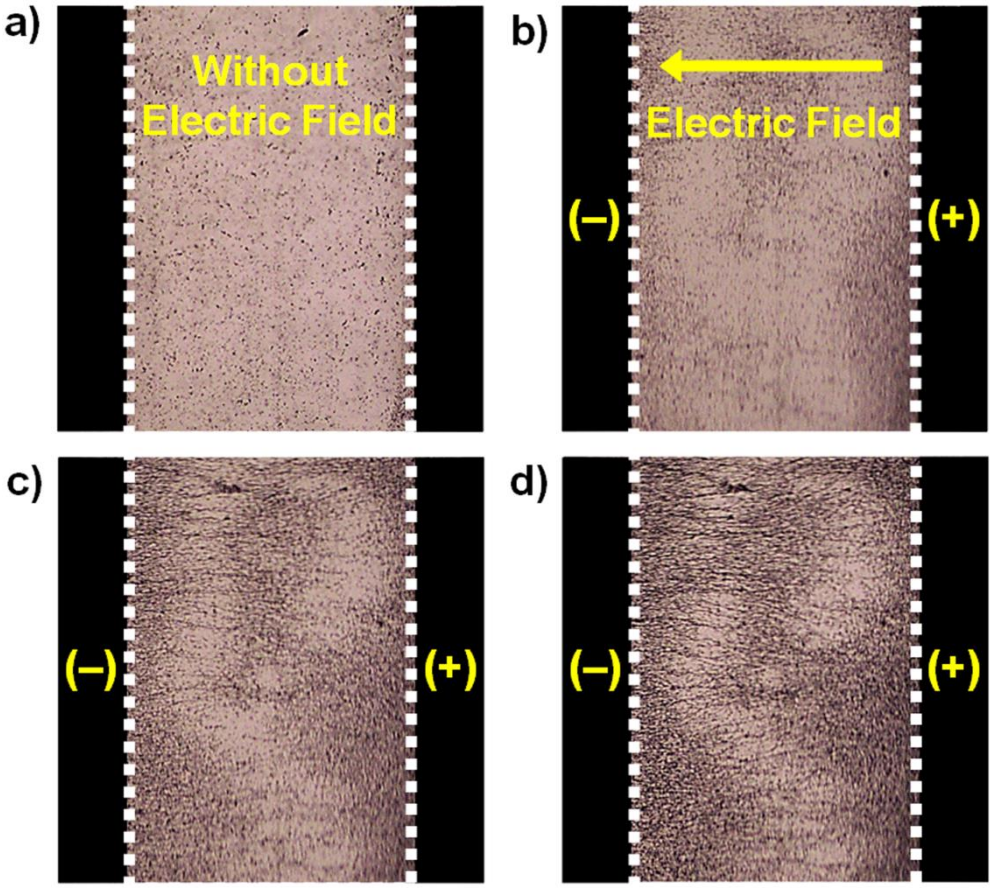

Figure 52. (a–d) Microscopy images of few-layer MoS_2 nanosheets-based ER fluid under an electric field.

4. CONCLUSIONS

1. To investigate the relationship between the geometrical shapes of electro-responsive materials and ER performance, the GO-wrapped silica materials with different geometrical aspect ratios were successfully fabricated by using a facile and straightforward method. This method does not require a complicated process, and the simple process provides a great possibility to fabricate GO-wrapped silica materials in large quantities. This reliable approach may offer an opportunity for the further investigation of practical or industrial applications.
2. To achieve an in-depth into the effect of particle geometry on ER fluid, the electro-responsive activities of GO-wrapped silica materials-based fluids were examined under various experimental conditions. It was demonstrated that the electro-responsive properties improved as the aspect ratio of the electro-responsive material increased, which could be elucidated by the geometrical effect and dielectric properties of material. The geometrical effect played a dominant role in the enhancement of ER performance, which was explained by flow resistance and mechanical stability. Additionally, from the analysis of dielectric properties according to the dielectric loss model, it was confirmed that the GO-wrapped silica rod with a high aspect ratio provided the strongest polarizability and the shortest

relaxation time, compared with the spherical and rod-like materials. Accordingly, the ER properties of the fluids were improved on increasing the aspect ratio of the electro-responsive material, due to geometrical effects and the influence of the dielectric properties.

3. To examine the influence of the shell structure of the electro-responsive materials on ER performance, the DS HNPs were successfully synthesized. To the best of our knowledge, this is the first attempt to employ double-shell-structured hollow nanoparticles in ER fluid.
4. The DS HNPs-based ER fluids represented significantly enhanced ER performance compared with the SS HNPs-based ER fluids. In particular, the DS HNPs-based fluid showed the yield stress value of *ca.* 45.5 kPa, which was 4.1-fold higher than that of same weight fraction of the SS-HNPs based fluid. The improvement of ER activities was explained by pore structure and distribution. Because of the interfacial polarization produced by the increased number of shells, the DS HNPs-based ER fluid exhibited higher yield stress under an electric field.
5. Four different-sized DS HNPs were fabricated to investigate the effect of particle size on electro-responsive behavior. The ER performance of the DS HNPs-based fluids was observed to increase with a decrease in the diameter of particles, which was ascribed to the increased surface area of

the shell but not the small pores within shells. The yield stress of DS HNPs-based fluids was improved by 6.6 times as the diameter of DS HNPs was reduced by half. The enhanced achievable polarizability of the smaller DS HNPs was also confirmed by measuring the dielectric parameters of the DS HNPs. Moreover, the DS HNPs-based fluids exhibited outstanding anti-sedimentation properties, which promise a sufficient potential for practical and commercial applications.

6. To identify the correlation of electrical conductivity and electro-responsive characteristics, the few-layer MoS_2 nanosheets were prepared through mild grinding and delamination method using sonication. Electrical conductivity of the few-layer MoS_2 nanosheets was easily controlled by adjusting the annealing temperature, which was attributed to the typical feature of semiconductors. The strongest ER efficiency was observed when the electrical conductivity was closer to *ca*. 2.0×10^{-9} S cm^{-1}, corresponed to the theoretical result of the calculation based on the Wagner's equation. This intensive study on the influence of electrical conductivity on ER performance had significance for providing the possibility of transition-metal dichalcogenides as a candidate of electro-responsive material.

In summary, characteristics of electro-responsive materials were demonstrated as a function of several critical parameters, including particle geometry, electric field strength, dielectric property, and electrical conductivity. The influence of particle geometry on the electro-responsive activity was investigated by preparing the GO-wrapped silica materials with different aspect ratios through a straightforward and facile method. Interestingly, ER performance was enhanced as the aspect ratio of electro-responsive material increased, ascribed to the geometrical effect (*e.g.* flow resistance and mechanical stability) and dielectric properties. The effect of shell structure to electro-responsive performance was also examined by synthesizing the double-shell-structured SiO_2/TiO_2 hollow nanoparticles. The DS HNPs exhibited noticeable ER performance, corresponded to giant ER fluid, attributed to the enhanced interfacial polarization. Additionally, the effect of particle size was confirmed by controlling the diameter of DS HNPs. With decreasing the particle diameter, ER properties of the DS HNPs-based fluids were observed to increase, due to the larger achievable polarizability of the smaller particles. An in-depth study on relationship between the electro-responsive behavior and electrical conductivity was carried out by adopting the few-layer MoS_2 nanosheets as an ER material which is one of layered transition-metal dichalcogenides. The electrical conductivity of the few-layer MoS_2 nanosheets

was easily controlled by adjusting the annealing temperature since the MoS_2 represented semi-conducting characteristics. The electro-responsive behavior of few-layer MoS_2 nanosheets-based fluids corresponded to the Wagner's model which depicted the interfacial polarization existing in a heterogeneous system.

The electro-responsive behavior depending on the nanoparticle characteristics was clarified by adjusting the particle geometry and properties. This study may provide promising strategies for performance enhancement of electro-responsive smart fluids.

REFERENCES

[1] Y. Lu, W. Sun, Z. Gu, *J. Control. Release*, **2014**, *194*, 1.

[2] M. A. C. Stuart, W. T. S. Huck, J. Genzer, M. Müller, C. Ober, M. Stamm, G. B. Sukhorukov, I. Szleifer, V. V. Tsukruk, M. Urban, F. Winnik, S. Zauscher, I. Luzinov, S. Minko, *Nat. Mater.*, **2010**, *9*, 101.

[3] M. Motornov, Y. Roiter, I. Tokarev, S. Minko, *Prog. Polym. Sci.*, **2010**, *35*, 174.

[4] Z. S. Liu, P. Calvert, *Adv. Mater.*, **2000**, *12*, 288.

[5] M. H. Li, P. Keller, *Soft Matter*, **2009**, *5*, 927.

[6] S. L. R. Barker, D. Ross, M. J. Tarlov, M. Gaitan, L. E. Locascio, *Anal. Chem.*, **2000**, *72*, 5925.

[7] D. Cunliffe, C. de las H. Alarcón, V. Peters, J. R. Smith, C. Alexander, *Langmuir*, **2003**, *19*, 2888.

[8] M. Yamato, C. Konno, M. Utsumi, A. Kikuchi, T. Okano, *Biomaterials*, **2002**, *23*, 561.

[9] J. Raula, J. Shan, M. Nuopponen, A. Niskanen, H. Jiang, E. I. Kauppinen, H. Tenhu, *Langmuir*, **2003**, *19*, 3499.

[10] A. S. Hoffman, *J. Control. Release*, **2008**, *132*, 153.

[11] P. M. Mendes, *Chem. Soc. Rev.*, **2008**, *4*, 714.

[12] J. Kost, R. Langer, *Adv. Drug Delivery Rev.*, **2002**, *54*, 53.

[13] L. K. Ista, G. P. Lopez, *J. Ind. Microbiol. Biotechnol.*, **1998**, *20*, 121.

[14] J. Hoffman, M. Plotner, D. Kuckling, W. J. Fischer, *Sens. Actuators, A*, **1999**, *77*, 139.

[15] Z. Gu, M. Yan, B. Hu, K. I. Joo, A. Biswas, Y. Huang, Y. Lu, P. Wang, Y. Tang, *Nano Lett.*, **2009**, *9*, 4533.

[16] L. Wang, M. Liu, C. Gao, L. Ma, D. Cui, *React. Funct. Polym.*, **2010**, *70*, 159.

[17] M. H. Cho, E. J. Lee, M. Son, J. H. Lee, D. Yoo, J. W. Kim, S. W. Park, J. S. Shin, J. Cheon, *Nat. Mater.*, **2012**, *11*, 1038.

[18] A. Schroeder, M. S. Goldberg, C. Kastrup, Y. Wang, S. Jiang, B. J. Joseph, C. G. Levins, S. T. Kannan, R. Langer, D. G. Anderson, *Nano Lett.*, **2012**, *12*, 2685.

[19] Y. Y. Song, F. Schmidt-Stein, S. Bauer, P. Schmuki, *J. Am. Chem. Soc.*, **2009**, *131*, 4230.

[20] M. X. Zhao, B. L. Hu, Z. Gu, K. I. Joo, P. Wang, Y. Tang, *Nano Today*, **2013**, *8*, 11.

[21] M. X. Zhao, A. Biswas, B. L. Hu, K. I. Joo, P. Wang, Z. Gu, Y. Tang, *Biomaterials*, **2011**, *32*, 5223.

[22] M. Yan, J. J. Du, Z. Gu, M .Liang, Y. F. Hu, W. J. Zhang, S. Priceman, L. L. Wu, Z. H. Zhou, Z. Liu, T. Segura, Y. Tang, Y. F. Lu, *Nat. Nanotechnol.*, **2010**, *5*, 48.

[23] Y. Liu, J. J. Du, M. Yan, M. Y. Lau, J. Hu, H. Han, O. O. Yang, S. Liang, W. Wei, H. Wang, J. M. Li, X. Y. Zhu, L. Q. Shi, W. Chen, C. Ji, Y. F. Lu, *Nanotechnol.*, **2013**, *8*, 187.

[24] X. J. Wu, S. Q. Wu, L. Yang, J. H. Han, S. F. Han, *J. Mater. Chem.*, **2012**, *22*, 17121.

[25] W. B. Liechty, R. Chen, F. Farzaneh, M. Tavassoli, N. K. H. Slater, *Adv. Mater.*, **2009**, *21*, 3910.

[26] Y. Lee, T. Ishii, H. J. Kim, N. Nishiyama, Y. Hayakawa, K. Itaka, K. Kataoka, *Angew. Chem. Int. Ed.*, **2010**, *49*, 2552.

[27] Y. Lee, T. Ishii, H. Cabral, H. J. Kim, J. H. Seo, N. Nishiyama, H. Oshima, K. Osada, K. Kataoka, *Angew. Chem. Int. Ed.*, **2009**, *48*, 5309.

[28] X. Gu, J. Wang, Y. Wang, Y. Wang, H. Gao, G. Wu, *Colloids Surf. B*, **2013**, *108*, 205.

[29] V.-R. María, B. Franscisco, A. Daniel, *Angew. Chem. Int. Ed.*, **2007**, 46, 7548.

[30] Y. W. Zhang, Z. X. Wang, Y. S. Wang, H. X. Zhao, C. X. Wu, *Polymer*, **2007**, *48*, 5639.

[31] M. Motornov, R. Sheparovych, R. Lupitskyy, E. MacWilliams, S. Minko, *J. Collod Interface Sci.*, **2007**, *310*, 481.

[32] M. Motornov, R. Sheparovych, R. Lupitskyy, E. MacWilliams, O. Hoy, I. Luzinov, S. Minko, *Adv. Funct. Mater.*, **2007**, *17*, 2307.

[33] S. Fujii, S. P. Armes, B.P. Binks, R. Murakami, *Langmuir*, **2006**, *22*, 6818.

[34] J. Shi, N. M. Alves, J. F. Mano, *Adv. Funct. Mater.*, **2007**, *17*, 3312.

[35] L. E. Bromberg, E. S. Ron, *Adv. Drug Deliv. Rev.*, **1998**, *31*, 197.

[36] D. J. Gan, L. A. Lyon, *Anal. Chim. Acta.*, **2003**, *496*, 53.

[37] I. Berndt, J. S. Pedersen, W. Richtering, *Angew. Chem. Int. Ed.*, **2006**, *45*, 1737.

[38] J. F. Mano, *Adv. Eng. Mater.*, **2008**, *10*, 515.

[39] C. de las H. Alarcón, S. Pennadam, C. Alexander, *Chem. Soc. Rev.*, **2005**, *34*, 276.

[40] S. A. Stanley, J. E. Gagner, S. Damanpour, M. Yoshida, J. S. Dordick, J. M. Friedman, *Science*, **2012**, *336*, 604.

[41] Y. Hu, N. N. Zhao, J. S. Li, W. T. Yang, F. J. Xu, *J. Mater. Chem.*, **2012**, *22*, 21257.

[42] S. Arnott, A. Fulmer, W. E. Scott, I. C. Dea, R. Moorhouse, D. A. Rees, *J. Mol. Biol.*, **2005**, *103*, 609.

[43] J. Y. Wu, S. Q. Liu, P. W. Heng, Y. Y. Yang, *J. Control. Release*, **2005**, *102*, 361.

[44] T. Hao, *Adv. Mater.*, **2001**, *13*, 1847.

[45] T. C. Halsey, *Adv. Mater.*, **1993**, *5*, 711.

[46] H. Block, J. P. Kelly, *J. Phys. D: Appl. Phys.*, **1988**, *21*, 1661.

[47] T. C. Halsey, *Science*, **1992**, *258*, 761.

[48] J. M. Ginder, L. C. Davis, *Appl. Phys. Lett.*, **1994**, *65*, 3410.

[49] J. H. Park, B. D. Chin, O. O. Park, *J. Colloid Interface Sci.*, **2001**, *240*, 349.

[50] S. Lee, K.-Y. Shin, J. Jang, *Nanoscale*, **2015**, *7*, 9646.

[51] R. Tomer, D. Dimitrijevic, A. T. Florence, *J. Control. Release*, **1995**, *33*, 405.

[52] M. Jensen, P. Birch Hansen, S. Murdan, S. Frokjaer, A. T. Florence, *Eur. J. Pharm. Sci.*, **2002**, *15*, 139.

[53] M. Chorny, E. Hood, R. J. Levy, V. R. Muzykantov, *J. Control. Release*, **2010**, *146*, 144.

[54] X. Huang, X. Meng, F. Tang, L. Li, D. Chen, H. Liu, Y. Zhang, J. Ren, *Nanotechnology*, **2008**, *19*, 445101.

[55] M. Chorny, I. Fishbein, S. Forbes, I. Alferiev, *IUBMB Life*, **2011**, *63*, 613.

[56] L. Luo, Y. Guo, J. Yang, Y. Liu, S. Chu, F. Kong, Y. Wang, Z. Zou, *Chem. Commun.*, **2011**, *47*, 11243.

[57] H. Tang, H. Kobayashi, Y. Niidome, T. Mori, Y. Katayama, T. Niidome, *J. Control. Release*, **2013**, *171*, 178.

[58] D. E. De Rossi, P. Chiarelli, G. Buzzigoli, C. Domenici, L. Lazzeri, *ASAIO Trans*, **1986**, *32*, 157.

[59] M. Yamato, M. Utsumi, A. Kushida, C. Konno, A. Kikuchi, T. Okano, *Tissue Eng.*, **2001**, *7*, 473.

[60] H. G. Schild, *Prog. Polym. Sci.*, **1992**, *17*, 163.

[61] S. J. Kim, S. J. Park, S. M. Lee, Y. M. Lee, H. C. Kim, S. I. Kim, *J. Appl. Polym. Sci.*, **2003**, *89*, 890.

[62] D. W. Urry, *Biopolymers*, **1998**, *47*, 167.

[63] N. Peppas, *Curr. Opin. Colloid Interface Sci.*, **1997**, *2*, 531.

[64] S. K. Li, A. D'Emanuele, *J. Control. Release*, **2001**, *75*, 55.

[65] A. Kikuchi, T. Okano, *Adv. Drug Delivery Rev.*, **2002**, *54*, 53.

[66] I. Y. Galaev, B. Mattiasson, *Trends Biotechnol.*, **1999**, *17*, 335.

[67] M. Orlov, I. Tokarev, A. Scholl, A. Doran, S. Minko, *Macromolecules*, **2007**, *40*, 2086.

[68] I. Tokarev, M. Orlov, S. Minko, *Adv. Mater.*, **2006**, *18*, 2458.

[69] I. Tokarev, S. Minko, *Adv. Mater.*, **2009**, *21*, 241.

[70] V. Gopishetty, Y. Roiter, I. Tokarev, S. Minko, *Adv. Mater.*, **2008**, *20*, 4588.

[71] Y. G. Ko, U. S. Choi, *Soft Matter*, **2012**, *8*, 253.

[72] R. Shen, X. Eang, Y. Lu, D. Wang, G. Sun, Z. Cao, K. Lu, *Adv. Mater.*, **2009**, *21*, 4631.

[73] W. Wen, X. Huang, S. Yang, K. Lu, P. Sheng, *Nat. Mater.*, **2003**, *2*, 727.

[74] H. J. Choi, M. S. Jhon, *Soft Matter*, **2009**, *5*, 1562.

[75] T. Hao, *Adv. Colloid Interface Sci.*, **2002**, *97*, 1.

[76] M. Grzelczak, J. Vermant, E. M. Furst, L. M. Liz-Marzán, *ACS Nano*, **2010**, *4*, 3591.

[77] K. Negita, Y. Misono, T. Yamaguchi, J. Shinagawa, *J. Colloid Interface Sci.*, **2008**, *321*, 452.

[78] J. A. Marins, B. G. Soares, A. A. Silva, M. G. Hurtado, S. Livi, *J. Colloid Interface Sci.*, **2013**, *405*, 64.

[79] S. J. Park, M. S. Cho, S. T. Lim, H. J. Choi and M. S. Jhon, *Macromol. Rapid Commun.*, **2005**, *26*, 1563.

[80] W. M. Winslow, *J. Appl. Phys.*, **1949**, *20*, 1137.

[81] C. J. Gow, C. F. Zukoski, *J. Colloid Interface Sci.*, **1990**, *126*, 175.

[82] S. Wu, F. Zeng, J. Shen, *J. Appl. Polym. Sci.*, **1998**, *67*, 2077.

[83] U. Choi, *Colloids Surf. A*, **1999**, *157*, 193.

[84] U. Choi, B. Ahn, *Colloids Surf. A*, **2000**, *168*, 71.

[85] U. Choi, Y. Park, S. Lee, *Colloids Surf. A*, **2002**, *211*, 85.

[86] Y. Xu, R. Liang, *J. Rheol.*, **1991**, *35*, 1355.

[87] Z. Gao, X. Zhao, *J. Appl. Polym. Sci.*, **2004**, *93*, 1681.

[88] Z. Gao, Z. Zhao, *Materials Lett.*, **2002**, *57*, 615.

[89] B. H. Sung, U. S. Choi, H. G. Jang, Y. S. Park, *Colloids Surf. A*, **2006**, *274*, 37.

[90] V. Pavlínek, P. Sáhaa, T. Kitanob, J. Stejskalc, O. Quadratc, *Physica A*, **2005**, *353*, 21.

[91] J.-Y. Hong, J. Jang, *Soft Matter*, **2010**, *6*, 4669.

[92] J.-Y. Hong, E. Kwon, J. Jang, *Soft Matter*, **2009**, *5*, 951.

[93] W. L. Zhang, H. J. Choi, *Langmuir*, **2012**, *28*, 7055.

[94] W. L. Zhang, H. J. Choi, *Chem. Commun.*, **2011**, *47*, 12286.

[95] J.-Y. Hong, J. Jang, *Soft Matter*, **2012**, *8*, 3348.

[96] W. L. Zhang, Y. D. Liu, H. J. Choi, S. G. Kim, *ACS Appl. Mater. Interfaces*, **2012**, *4*, 2267.

[97] J. Y. Hong, E. Lee, J. Jang, *J. Mater. Chem. A*, **2013**, *1*, 117.

[98] W. L. Zhang, Y. D. Liu, H. J. Choi, *Carbon*, **2012**, *50*, 290.

[99] W. L. Zhang, B. J. Park, H. J. Choi, *Chem. Commun.*, **2010**, *46*, 5596.

[100] K.-Y. Shin, S. Lee, S. Hong, J. Jang, *ACS Appl. Mater. Interfaces*, **2014**, *6*, 5531.

[101] W. H. Zhang, X. D. Fan, W. Tian, W. W. Fan, *eXPRESS Polym. Lett.*, **2012**, *6*, 532.

[102] Y. D. Liu, W. L. Zhang, H. J. Choi, *Colloid Polym. Sci.*, **2012**, *290*, 855.

[103] Y. D. Liu, F. F. Fang, H. J. Choi, Y. Seo, *Colloids Surf. A*, **2011**, *381*, 17.

[104] Q. Cheng, V. Pavlinek, Y. He, Y. Yan, C. Li, P. Saha, *Colloid Polym. Sci.*, **2011**, *289*, 799.

[105] J. Yin, X. Zhao, L. Xiang, X. Xia, Z. Zhang, *Soft Matter*, **2009**, *5*, 4687.

[106] M. Sedlačík, M. Mrlík, V. Pavlínek, P. Sáha, O. Quadrat, *Colloid Polym. Sci.*, **2012**, *290*, 41.

[107] T. Dürrschmidt, H. Hoffmann, *Colloids Surf. A*, **1999**, *156*, 257.

[108] B. Wang, X. Zhao, *J. Mater. Chem.*, **2003**, *13*, 2248.

[109] Z. Y. Qiu, L. W. Liu, Z. W. Wang, L. W. Zhou, *Int. J. Mod. Phys. B*, **2001**, 610.

[110] J. C. Ryu, J. W. Kim, H. J. Choi, S. B. Choi, J. H. Kim, *J. Mater. Sci. Lett.*, **2003**, *22*, 807.

[111] K. Prekas, T. Shah, N. Soin, M. Rangoussi, S. Vassiliadis, E. Siores, *J. Colloid Interface Sci.*, **2013**, *401*, 58.

[112] G. Schwarz, S. Maisch, S. Ullrich, J. Wagenhöfer, D. G. Kurth, *ACS Appl. Mater. Interfaces*, **2013**, *5*, 4031.

[113] J. A. Marins, K. Dahmouche, B. G. Soares, *Mater. Sci. Eng. C*, **2013**, *33*, 133.

[114] Y. Tian, Y. Meng, S. Wen, *Mater. Lett.*, **2001**, *50*, 120.

[115] N. K. Jaggi, J. Woestman, *Bull. Am. Phys. Soc.*, **1989**, *34*, 1019.

[116] D. L. Klass, T. W. Martinek, *J. Appl. Phys.*, **1967**, *38*, 67.

[117] C. Gehin, J. Persello, *Int. J. Mod. Phys. B*, **2002**, *16*, 2494.

[118] H. Y. Kim, H. J. Choi, *RSC Adv.*, **2014**, *4*, 28511.

[119] Y. P. Seo, H. J. Choi, Y. Seo, *Polymer*, **2011**, *52*, 5695.

[120] H. J. Choi, M. S. Jhon, *Soft Matter*, **2009**, *5*, 1562.

[121] T. Hao, Y. Chen, Z. Xu, Y. Xu, Y. Haung, *Chin. J. Polym. Sci.*, **1994**, *12*, 97.

[122] S. Lee, J.-Y. Hong, J. Jang, *J. Colloid Interface Sci.*, **2013**, *398*, 33.

[123] D. V. Miller, C. A. Randall, A. Bhalla, R. E. Newnham, J. H. Adair, *Ferroelectrics Lett.*, **1993**, *15*, 141.

[124] C. S. Coughlin, R. N. Capps, *Proc. SPIE-Intn. Soc. Opt. Eng.*, **1994**, *2190*, 17.

[125] R. Kanu, M. Shaw, *J. Rheol.*, **1998**, *42*, 657.

[126] R. W. Sillars, *JIEE*, **1937**, *80*, 378.

[127] H. Block, J. P. Kelley, A. Qin, T. Watson, *Langmuir*, **1990**, *6*, 6.

[128] T. Hao, Z. Xu, Y. Xu, *J. Colloid Interface Sci.*, **1997**, *190*, 334.

[129] T. Hao, *J. Colloid Interface Sci.*, **1998**, *206*, 240.

[130] K. D. Weiss, D. A. Nixon, J. D. Carlson, A. J. Margida, *Polym. Preprints*, **1994**, *35*, 325.

[131] L. C. Davis, *J. Appl. Phys.*, **1992**, *72*, 1334.

[132] J.-N. Foulc, P. Atten, N. Felici, *J. Electrostatic*, **1994**, *33*, 103.

[133] P. Atten, J.-N. Foulc, N. Felici, *Int. J. Mod. Phys. B*, **1994**, *8*, 2731.

[134] H. Uejima, *Jpn. J. Appl. Phys.*, **1972**, *11*, 319.

[135] D. L. Klass, T. W. Martinek, *J. Appl. Phys.*, **1967**, *38*, 75.

[136] Y. F. Deinega, K. K. Popko, N. Y. Kovganich, *Heat-Transfer-Sov. Res.*, **1978**, *10*, 50.

[137] Y. Tian, M. Zhang, J. Jiang, N. Pesika, H. Zeng, J. Israelachvili, Y. Meng, S. Wen, *Phys. Rev. E*, **2011**, *83*, 011401.

[138] T. C. Jordan, M. T. Shaw, *IEEE Trans. Electric Insul.*, **1989**, *24*, 849.

[139] A. P. Alice, C. F. Zukoski, *Adv. Colloid Interf. Sci.*, **1989**, *30*, 153.

[140] D. J. Klingenberg, *MRS Bulletin*, **1998**, *23*, 30.

[141] X. Tang, C. Wu, H. Conrad, *J. Rheol.*, **1995**, *39*, 1059.

[142] C. Wu, H. Conrad, *J. Phys. D: Appl. Phys.*, **1996**, *29*, 3147.

[143] Y. F. Deinega, G. V. Vinogradov, *Rheo. Acta*, **1984**, *23*, 636.

[144] W. Wen, K. Lu, *Phys. Fluids*, **1997**, *9*, 1828.

[145] W. Wen, K. Lu, *Phys. Fluids*, **1996**, *8*, 2789.

[146] J. E. Stangroom, *Phys. Technol.*, **1983**, *14*, 290.

[147] Y. D. Kim, D. J. Klingenberg, *J. Colloid Interface Sci.*, **1996**, *183*, 568.

[148] T. Hao, A. Kawai, F. Ikazaki, *Langmuir*, **1998**, *14*, 1256.

[149] T. Hao, A. Kawai, F. Ikazaki, *Langmuir*, **1999**, *15*, 918.

[150] T. Hao, A. Kawai, F. Ikazaki, *Langmuir*, **2000**, *16*, 3058.

[151] T. Hao, *Appl. Phys. Lett.* **1997**, *70*, 1956.

[152] L. Wang, M. Zhang, J. Li, X. Gong, W. Wen, *Lab Chip*, **2010**, *10*, 2869.

[153] J. Yin, X. Zhao, X. Xia, L. Xiang, Y. Qiao, *Polymer*, **2008**, *49*, 4413.

[154] X. Song, A. Hu, N. Tan, D. Ma, Y. Lin, *Mater. Chem. Phys.*, **2011**, *126*, 369.

[155] K. P. S. Parmar, Y. Meheust, B. Schjederupsen, J. O. Fossum, *Langmuir*, **2008**, *24*, 1814.

[156] L. C. Davis, *J. Appl. Phys.*, **1977**, *81*, 1985.

[157] H. J. Choi, M. S. Cho, J. W. Kim, *Appl. Phys. Lett.*, **2001**, *78*, 3806.

[158] W. G. Litvinov, *IMA J. Appl. Math.*, **2007**, *73*, 619.

[159] Q.-H. Nguyen, S.-B. Choi, *Smart Mater. Struct.*, **2009**, *18*, 115020.

[160] N. M. Wereley, J. Lindler, N. Rosenfeld, Y.-T. Choi, *Smart. Mater. Struct.*, **2004**, *13*, 743.

[161] M. Zhang, J. Wu, X. Niu, W. Wen, P. Sheng, *Phys. Rev. E*, **2008**, *78*, 066305.

[162] V. Shapiro, V. Freger, C. Linder, Y. Oren, *J. Phys. Chem. B*, **2008**, *112*, 9389.

[163] Y. Otsubo, Y. Suda, *J. Colloid Interface Sci.*, **2002**, *253*, 224.

[164] Y.-M. Han, S.-B. Choi, *Smart Mater. Struct.*, **2008**, *17*, 065012.

[165] W. Stöber, A. Fink, E. Bohn, *J. Colloid Interface Sci.*, **1968**, *26*, 62.

[166] H. Giesche, *J. Eur. Ceram. Soc.*, **1994**, *14*, 205.

[167] A. Kuijk, A. Van Blaaderen and A. Imhof, *J. Am. Chem. Soc.*, **2011**, *133*, 2346.

[168] J. He, B. Yu, M. J. Hourwitz, Y. Liu, M. T. Perez, J. Yang and Z. Nie, *Angew. Chem., Int. Ed.*, **2012**, *51*, 3628.

[169] J. He, M. J. Hourwitz, Y. Liu, M. T. Perezand Z. Nie, *Chem. Commun.*, **2011**, *47*, 12450.

[170] S. Lee, J.-Y. Hong, J. Jang, *Polym. Int.* **2013**, *62*, 901.

[171] S. Lee, J.-Y. Hong, J. Jang, *ACS Nano*, **2013**, *7*, 5784.

[172] J. Hong, K. Char and B. S. Kim, *J. Phys. Chem. Lett.*, **2010**, *1*, 3442.

[173] J. S. Lee, J. C. Yoon and J. H. Jang, *J. Mater. Chem. A*, **2013**, *1*, 7312.

[174] M. Choi, C. Kim, S. O. Jeon, K. S. Yook, J. Y. Lee, J. Jang, *Chem. Commun.*, **2011**, *47*, 7092.

[175] J. Y. Hong, J. Jang, *Soft Matter*, **2010**, *6*, 4669

[176] B. Wang, X. Zhao, *Langmuir*, **2005**, *21*, 6553.

[177] N. Moradian, D. S. K. Ting, S. Cheng, *Exp. Therm. Fluid Sci.*, **2009**, *33*, 460.

[178] Z. G. Feng, E. E. Michaelides, *J. Fluids Eng.*, **2001**, *123*, 841.

[179] H. J. Choi, C. H. Hong, M. S. Jhon, *Int. J. Mod. Phys. B*, **2007**, *21*, 4974.

[180] K. Asami, *Prog. Polym. Sci.*, **2002**, *27*, 1617.

[181] J.-Y. Hong, M. Choi, C. Kim, J. Jang, *J. Colloid Interface Sci.*, **2010**, *347*, 177.

[182] R. C. Kanu, M. T. Shaw, *J. Rheol.*, **1998**, *42*, 657;

[183] J. A. Stratton, Electromagnetic Theory, *McGraws-Hill*, New York and London, **1941**.

[184] S. S. Dukhin, Dielectric Properties of Disperse Systems, *Wiley-Interscience*, New York, **1971**.

[185] J. B. Yin, X. P. Zhao, *Chem. Mater.*, **2004**, *16*, 321.

[186] I. S. Sim, J. W. Kim, H. J. Choi, C. A. Kim, M. S. Jhon, *Chem. Mater.* **2001**, *13*, 1243.

[187] M. S. Cho, H. J. Choi, M. S. Jhon, *Polymer*, **2005**, *46*, 11484.

[188] Y. D. Liu, H. J. Choi, *Soft Matter*, **2012**, *8*, 11961.

[189] J. B. Yin, X. P. Zhao, *Chem. Mater.*, **2002**, *14*, 4633.

[190] S. H. Vemuri, M. S. Jhon, K. Zhang, H. J. Choi, *Colloid Polym. Sci.*, **2012**, *290*, 189.

[191] K. Zhang, Y. D. Liu, M. S. Jhon, H. J. Choi, *J. Colloid Interface Sci.*, **2013**, *409*, 259.

[192] M. Parthasarathy, D. J. Klingenberg, *Mater. Sci. Eng. R-Rep.*, **1996**, *17*, 57.

[193] Y. D. Liu, Y. Cheng, G. Xu, H. J. Choi, *Colloid Polym. Sci.*, **2013**, *291*, 1267.

[194] X. Huang, W. Wen, S. Yang, P. Sheng, *Solid State Commun.* **2006**, *139*, 581.

[195] Z. H. Chen, C. Kim, X.B. Zeng, S. H. Hwang, J. Jang, G. Ungar, *Langmuir*, **2012**, *28*, 15350.

[196] T. Zhang, J. Ge, Y. Hu, Q. Zhang, S. Aloni, Y. Yin, *Angew. Chem., Int. Ed.*, **2008**, *47*, 5806.

[197] S. J. Park, Y. J. Kim, S. J. Park, *Langmuir*, **2008**, *24*, 12134.

[198] S. Lee, C.-M. Yoon, J.-Y. Hong, J. Jang, *J. Mater. Chem. C*, **2014**, *2*, 6010.

[199] S. D. Kim, W. L. Zhang, H. J. Choi, *J. Mater. Chem. C*, **2014**, *2*, 7541.

[200] K. Kim, D. Stroud, X. Li, D. J. Bergman, *Phys. Rev. E*, **2005**, *71*, 031503.

[201] S. Kim, C. Kim, J.-Y. Hong, S. H. Hwang, J. Jang, *RSC Adv.*, **2014**, *4*, 6821.

[202] D. R. Gamota, A. W. Schubring, B. L. Mueller, F. E. Filisko, *J. Mater. Res.*, **1996**, *11*, 144.

[203] B. X. Wang, X. P. Zhao, *Adv. Funct. Mater.* **2005**, *15*, 1815.

[204] Y. D. Liu, X. Quan, B. Hwang, Y. K. Kwon, H. J. Choi, *Langmuir*, **2014**, *30*, 1729.

[205] H. Conrad, A. F. Sprecher, Y. Choi, Y. Chen, *J. Rheol.*, **1991**, *35*, 1393.

[206] S. G. Kim, J. Y. Lim, J. H. Sung, H. J. Choi, Y. Seo, *Polymer*, **2007**, *48*, 6622.

[207] J. Yin, X. Xia, L. Xiang, X. Zhao, *Smart Mater. Struct.*, **2011**, *20*, 015002.

[208] X. P. Zhao, J. B. Yin, *Chem. Mater.* **2002**, *14*, 2258.

[209] J. Yin, X. Zhao, *J. Phys. D: Appl. Phys.* **2001**, *34*, 2063.

[210] S. Lee, J.-Y. Hong, J. Jang, *J. Mater. Chem. C*, **2014**, *2*, 8525.

[211] C.-M. Yoon, S. Lee, S. H. Hong, J. Jang, *J. Colloid Interface Sci.* **2014**, *438*, 14.

[212] N. Lanzillo, A. G. Birdwell, M. Amani, F. J. Crowne, P. B. Shah, S. Najmaei, Z. Liu, P. M. Ajayan, J. Lou, M. Dubey, S, K. Nayak, T. P. O'Regan, *Appl. Phys. Lett.*, **2013**, *103*, 093102.

[213] C. Lee, H. Yan, L. E. Brus, T. F. Heinz, J. Hone, S. Ryu, *ACS Nano*, **2010**, *4*, 2695.

[214] Y. Yao, L. Tolentino, Z. Yang, X. Song, W. Zhang, Y. Chen, C. P. Wong, *Adv. Funct. Mater.*, **2013**, *23*, 3577.

[215] S. Sahoo, A. P. S. Gaur, M. Ahmadi, M. J. F. Guinel, R. S. Katiyar, *J. Phys. Chem. C*, **2013**, *117*, 9042.

[216] M. Thripuranthaka1, R. V. Kashid, C. S. Rout, D. J. Late, *Appl. Phys. Lett.*, **2014**, *104*, 081911.

[217] A. P. Nayak, T. Pandey, D. Voiry, J. Liu, S. T. Moran, A. Sharma, C. Tan, C. H. Chen, L. J. Li, M. Chhowalla, J. F. Lin, A. K. Singh, D. Akinwande, *Nano Lett.*, **2015**, *15*, 346.

[218] D. Yang, S. J. Sandoval, W. M. R. Divigalpitiya, J. C. Irwin, R. F. Frindt, *Phys. Rev. B*, **1991**, *43*, 12053.

[219] S. J. Sandoval, D. Yang, R. F. Frindt, J. C. Irwin, *Phys. Rev. B*, **1991**, *44*, 3955.

[220] K. F. Mak, C. Lee, J. Hone, J. Shan, T. F. Heinz, *Phys. Rev. Lett.*, **2010**, *105*, 136805.

[221] A. Splendiani, L. Sun, Y. Zhang, T. Li, J. Kim, C. Y. Chim, G. Galli, F. Wang, *Nano Lett.*, **2010**, *10*, 1271.

[222] G. Eda, H. Yamaguchi, D. Voiry, T. Fujita, M. Chen, M. Chhowalla, *Nano Lett.*, **2011**, *11*, 5111.

[223] B. Visic, R. Dominko, M. Gunde, N. Hauptman, S. D Skapin, M. Remskar, *Nano. Res. Lett.*, **2011**, *6*, 593.

[224] H. Li, Q. Zhang, C. C. R. Yap, B. K. Tay, T. H. T. Edwin, A. Olivier, D. Baillargeat, *Adv. Funct. Mater.*, **2012**, *22*, 1385.

[225] J. F. Shackelford, Introduction to Materials Science for Engineers, 6th Ed., *Pearson Education Inc.*, **2005**.

[226] B. G. Streetman, S. K. Banerjee, Solid State Electronic Devices, 6th Ed., *Pearson Education Inc.*, **2006**.

[227] T. Hao, H. Yu, Y. Xu, *J. Colloid Interface Sci.*, **1996**, *184*, 542.

[228] T. Hao, Y. Xu, Y. Chen, M. Xu, *Chin. Phys. Lett.*, **1995**, *12*, 573.

국문초록

지능형 소재라 불리는 자극 반응성 물질은, 페하, 온도, 빛, 기계력, 전기장 또는 자기장 등의 외부 자극에 반응하여 물질의 구조, 치수, 상호작용 등을 변화시킨다. 자극 반응성 물질은 환경 조건에 따라 반응성을 조절할 수 있다는 특성으로 인해 전 세계적으로 집중적인 관심을 받아왔다. 특히, 전기 반응성 물질은, 인가된 전기장에 따라 제어 가능한 특성을 나타내는 소재로 정의되며, 낮은 소비전력, 빠른 가역 변화, 간단한 유체 역학 등의 장점이 있어 실질적으로 응용 가능성이 가장 높은 소재이다. 현재까지 다양한 전기 반응성 물질이 제조되고 전기 반응성 유체에 적용되어왔지만, 입자의 특성에 따라 전기 반응성을 심도있게 다룬 연구는 거의 없었다. 게다가 불충분한 성능과 침전 문제 등으로 인해 전기 반응성 유체를 실질적으로 상업화하는 데는 여러가지 한계가 있다. 따라서, 높은 효율을 나타내는 획기적인 전기 반응성 소재 개발은 여전히 부족한 실정이다. 또한, 전기 반응성 유체의 역학을 좀 더 정확하게 이해하기 위하여, 입자 특성이 전기 반응 특성에 미치는 영향에 대해 규명할 필요가 있다.

본 학위논문에서는 독창적인 나노입자를 제조하여 전기 반응성 유체에 응용함으로써 입자 형태, 유전 특성, 전기 전도도 등의 중요 변수에 따른 전기 반응 특성을 체계적으로 고찰하였다. 첫 번째로, 산화 그래핀으로 코팅된 실리카 나노입자의 종횡비 조절을 통해 입자 형태가 전기 반응성에

미치는 영향에 대해 살펴보았다. 산화 그래핀으로 코팅된 실리카 입자의 종횡비가 클수록, 유동 저항, 역학적 안정성과 같은 기하학적 영향과 높은 유전율로 인해 전기유변 효과가 향상되었다. 두 번째로, 단일 셀과 이중 셀 구조의 실리카/티타니아 중공 나노입자를 제조함으로써 입자 셀 구조와 전기 반응 특성과의 관계에 대해 알아보았다. 이중 셀 구조의 실리카/티타니아 중공 나노입자는 계면 분극이 더 강하게 발생하기 때문에 뛰어난 전기 반응 특성을 나타냈다. 더 나아가 입자의 직경이 작을수록 전기유변 효율이 높아졌으며, 이는 높은 분극률에 기인한 결과이다. 뿐만 아니라, 침강 방지 특성이 현저하게 우수하였으며, 이러한 특성은 실질적인 상업화 가능성을 시사한다. 세 번째로, 이황화몰리브덴 나노시트를 전기유변유체에 도입함으로써 전기 반응 거동과 전기 전도도와의 상관성에 대해 확인하였다. 전이 금속 이유화 물질에 해당하는 이황화몰리브덴은 반도체 특성을 지니고 있어 열 처리 온도에 따라 전기 전도도 조절이 가능하다. 지금까지 전기 금속 이유화 물질을 전기 반응성 유체에 적용한 사례는 없었으며, 전기 반응성 물질의 전기 전도도 변화에 따른 전기유변 특성에 대해 깊이 있게 연구한 사례가 거의 없었다는 점에서 본 연구 결과는 큰 의의가 있다.

본 연구는 입자의 종횡비, 셀 구조, 전기 전도도 등이 조절된 나노입자를 제조함으로써, 입자 특성이 전기 반응 특성에 미치는 효과에 대해 심도 있게 고찰하였으며, 전기 반응성 지능형 유체의 성능 향상을

위한 유망한 접근법을 제시한다.

주요어: 지능형 유체, 자극 반응성, 전기 반응성, 나노입자, 전기유변유체

학번: 2011-22926